Atomic Diffusion and Pulsation in Post-Common-Envelope Binary Stars

A thesis submitted to the University of Dublin
for the degree of Doctor of Philosophy

Conor M. Byrne, BA (Mod.)

Armagh Observatory and Planetarium & Trinity College Dublin

May 2020

Trinity College Dublin
Coláiste na Tríonóide, Baile Átha Cliath
The University of Dublin

Declaration

I declare that this thesis has not been submitted as an exercise for a degree at this or any other university and it is entirely my own work.

I agree to deposit this thesis in the University's open access institutional repository or allow the Library to do so on my behalf, subject to Irish Copyright Legislation and Trinity College Library conditions of use and acknowledgement.

I consent to the examiner retaining a copy of the thesis beyond the examining period, should they so wish.

Name: Conor M. Byrne

Signature: ..... **Date:** .....

Summary

I study the evolution of peculiar low-mass, evolved stars. Two groups of interest are the core-helium-burning hot subdwarfs and the shell-hydrogen-burning low-mass pre-white dwarfs. Stars in both groups have had previous interactions with a companion in order to remove most of their outer layers to leave the stars we see today. A detailed understanding of the past evolution of these stars provides important information about the interaction between close binary companions. This in itself is important, as approximately half of all stars in the Milky Way are in a binary or multiple star system. Additionally, hot subdwarfs show a variety of unusual surface compositions, with some stars showing lead and zirconium on their surface in amounts thousands of times more plentiful than seen in the Sun. It has been proposed that this is the result of radiative levitation, whereby outgoing radiation from the star can provide an upward force on certain elements, depending on their atomic structure.

The open-source MESA stellar evolution code was used to compute models of hot subdwarf stars and low-mass white dwarfs. These models were produced by using a large mass-loss rate to strip the outer layers from a red giant model, leaving either a low-mass core-helium burning model (subdwarf) or a model with an inert helium core and a thin hydrogen-burning envelope (pre-white dwarf) depending on the mass of the red giant core. Models were produced both with and without the effects of radiative levitation to determine the impact that this has on the evolution and surface composition of these stars. These were the first self-consistent models of hot subdwarfs from Main Sequence star through to the Horizontal Branch.

It is shown that radiative levitation is important in the phase of evolution immediately following the ejection of the common envelope, something which had not previously been considered. Comparison with the abundances of the observed population of hot subdwarfs showed that while the qualitative abundance patterns agree, the efficiency of radiative levitation is too strong in the simulations. This implies that other mixing processes must be invoked in order to accurately reproduce the observed abundances. In the case of heavy metals such as lead and zirconium, the amount of atomic data presently available is insufficient to calculate radiative accelerations for these elements.

In the case of the low-mass white dwarfs, the interest here focused on the discovery by Pietrukowicz *et al.* (2017) and Kupfer *et al.* (2019) of large-amplitude pulsating variable stars which show surface temperatures similar to hot subdwarfs. These stars are currently known as Blue Large-Amplitude Pulsators (BLAPs). The proposed structure of these stars is a low-mass pre-white dwarf, formed in a similar manner to a hot subdwarf. I used the GYRE stellar oscillation code to analyse the structure of my models and determined that low-mass pre-white dwarfs can pulsate when they have a temperature and surface gravity equivalent to the observed pulsators, with the appropriate pulsation period. The inclusion of radiative levitation in the models was found to be necessary in order to drive the pulsations. This indicates that the driving mechanism is the κ-mechanism as a result of iron group opacity, the same mechanism which drives hot subdwarf pulsators. This represents the first conclusive identification of the evolutionary status of BLAPs along with the driving mechanism responsible for the pulsations. I have shown that a large instability region exists which unites the two currently observed groups of pulsator, and I predict that further such objects should be detected in ongoing and future large-scale sky surveys.

To my family

Acknowledgements

First and foremost, I would like to thank my supervisor Simon Jeffery. You have been an exceptional mentor, supporter and critic. I am truly grateful for the support, feedback and encouragement you have provided to me.

I would like to thank past members of the hot subdwarf group (Phil, Pamela, Holly and James W) for helpful scientific discussion and the cake at our group meetings. I thank my current and former officemates (Aaron Stinson, Rok Nežič and Chris Duffy) for putting up with me!

Thanks to all of the students and postdocs at the Observatory for providing both engaging scientific discussions along with entertaining non-scientific ones! Thank you to Yanina, Will, Onur, Galin, Eliceth, Erin, Lauren, Tom, Kerem, Pablo, Andreas, Boris and many visiting students for creating such an enjoyable work environment during my time in Armagh, along with a healthy dose of socialising. Thanks to James F, Lisa, David, and Miruna for some memorable board games and parties which provided a distraction from heavy workloads. Thanks also to the Education Team in the Planetarium, especially Heather and Sinead, it's been fun.

I must also give a huge thank you to the support staff at the Observatory, Aileen and Shane, who are always willing to assist in any way possible. Thanks to Emeritus Director Mark Bailey for illuminating me on the fascinating history of the Observatory and for many thought-provoking conversations. Thanks to Helen in the TCD Physics Office for admin support and the School of Physics finance team for helping me with my expenses.

I thank three amazing friends/classmates; Aoife Ryan who was in Armagh when I first discovered research can be fun, Stephen White for putting many smiles on my face and Dwayne Byrne for being there when I needed someone to talk to. I wish I was better at keeping in touch with all of you!

My journey would not have taken the course it has without the input of my school-teachers, in particular Brian Breen and Brendan Brennan.

I thank the Armagh diabetic support team for teaching me how to control my blood glucose when my pancreas decided to stop working. I thank the Irish Research Council for providing me with a scholarship to enable me to carry out this research.

Finally, a huge thank you to my family; Mum, Dad, Fionnuala, DJ, and extended family for their unending love, support and understanding.

Go raibh míle maith agaibh go léir.

List of Publications

Refereed Publications

1. **Byrne, C. M.**, Jeffery, C. S., Tout, C. A. & Hu, H.
   "Diffusion in hot subdwarf progenitors from the common envelope channel",
   Open Astronomy - Special Issue on Hot Subdwarfs and Related Objects VIII , vol. 26, pp. 214-218 (2017)

2. **Byrne, C. M.**, Jeffery, C. S., Tout, C. A. & Hu, H.
   "The effects of diffusion in hot subdwarf progenitors from the common envelope channel",
   Monthly Notices of the Royal Astronomical Society, vol. 475, pp. 4728-4738 (2018)

3. **Byrne, C. M.**, & Jeffery, C. S.
   "Post-common envelope binary stars, radiative levitation, and blue large-amplitude pulsators",
   Monthly Notices of the Royal Astronomical Society, vol. 481, pp. 3810-3820 (2018)

4. **Byrne, C. M.**, & Jeffery, C. S.
   "Pulsations in faint blue stars",
   Monthly Notices of the Royal Astronomical Society, in press.

Non-Refereed Publications

1. **Byrne, C.**, & Jeffery, C. S.
   "Post-common envelope binary stars, radiative levitation, and blue large-

amplitude pulsators",
Zenodo (proceedings of the Physics of Oscillating Stars conference)
http://doi.org/10.5281/zenodo.1570470 (2018)

"Pulsations in chemically peculiar hot subdwarfs",
Zenodo (proceedings of the Ninth Meeting of Hot Subdwarfs and Related Objects, in prep.)

Contents

List of Figures

LIST OF FIGURES

List of Tables

LIST OF TABLES

1 Introduction

The stars in the night sky have intrigued the human race for millennia. Ancient Greek, Arab and Chinese astronomers recorded and catalogued their locations and concluded that these stars were fixed to the celestial sphere, remaining in constant locations while the Sun and the other planets moved across the sky over the course of the year. Despite the conclusion that the heavens were a fixed sphere, it was known at least to the Chinese astronomers that 'new' stars could appear. One notable example of this is an extremely bright object that was recorded by Chinese astronomers in the year 1054. This 'guest star' was so bright that it could be seen in the daytime for several weeks and persisted in the night sky for approximately 2 years. It is now known that this was a supernova explosion, a highly energetic event taking place at the end of a star's life when it can no longer support its own mass, collapsing into an exotic end state such as a neutron star or black hole, leaving a disperse cloud, or nebula, of material around it. Thus, rather than this event heralding the birth of a new star, it was in fact, the death of one. In the case of the 1054 supernova, the remnant material was later identified in the constellation of Taurus, and is commonly referred to as the Crab Nebula (Figure 1.1).

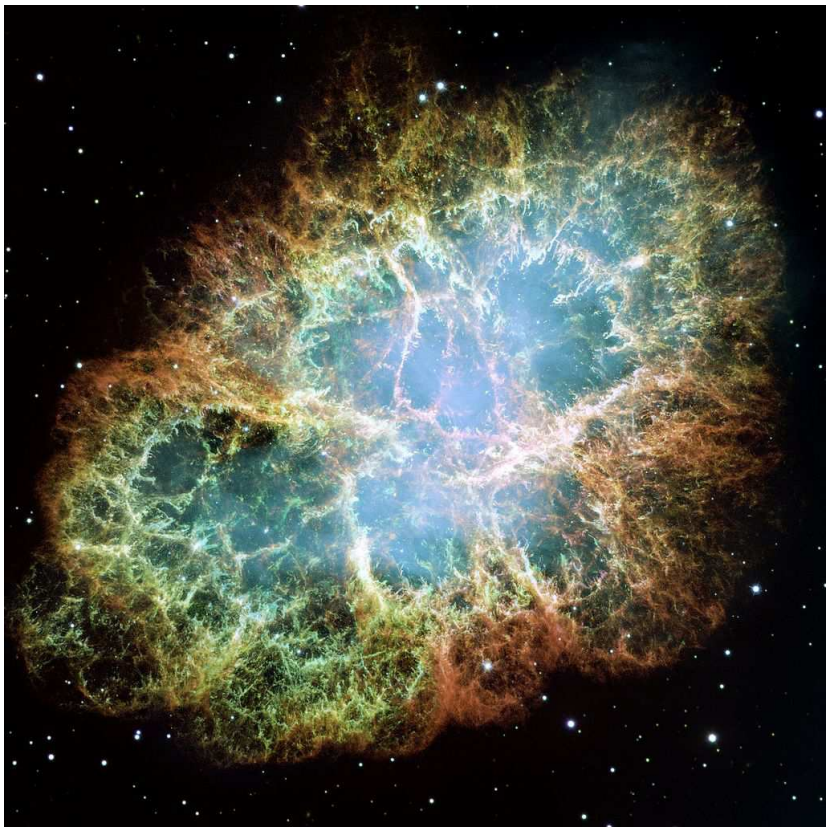

Figure 1.1: A Hubble Space Telescope image of the Crab Nebula, the remnants of a supernova explosion recorded by Chinese astronomers in the year 1054. Credit: ESA/NASA

As human knowledge and scientific understanding expanded, it became clear that the heavens were not quite as fixed and immutable as had been believed in ancient times. Edmond Halley recorded the locations of stars in 1718 and compared them to the work of Ptolemy some 1800 years previous. Halley concluded that a number of stars had moved in the intervening period, implying the stars were not as 'fixed' as had been assumed. People had also begun to ponder on the nature of the stars and what they might be. Italian philosopher Giordano Bruno (1584) hypothesised that the stars may be distant Suns and that these stars have their own planets around them. The latter of these statements was ultimately found to be correct with the discovery of an extra-solar planet orbiting around the solar-like star 51 Pegasi (Mayor & Queloz, 1995), along with the thousands of exoplanets discovered to date.

1.1 The Hertzsprung–Russell Diagram

Proving the former of Bruno's statements (that the stars are just distant counterparts of the Sun) requires one to first develop an understanding of what the Sun is. In the 17$^{\text{th}}$ century, Isaac Newton used a prism to separate light from the Sun into different colours, or a spectrum. Improvements in technology meant that by the 19$^{\text{th}}$ century, Joseph von Fraunhofer was able to take detailed measurements of the solar spectrum and noted that there were numerous dark lines in the spectrum at specific colours. Some of these lines were found by Kirchhoff and Bunsen to coincide with the emission spectrum of hydrogen gas (Kirchhoff, 1860). This led to the conclusion that the Sun was comprised of the same chemical elements as those found on the Earth. Spectroscopic measurements of other bright stars such as Sirius showed that they also had spectral lines, but in different arrangements. This provided proof that the Sun is indeed a star, although they are not all identical. By the end of the 19$^{\text{th}}$ century, astronomers were developing schemes to classify and arrange stellar spectra according to the number, strength and location of their spectral lines. One such scheme was developed at Harvard by Cannon & Pickering (1912). This classification assigned the letters O, B, A, F, G, K and M to stars based on the strength of different set of spectral lines. The Harvard spectral classification scheme remains more or less unchanged and in active use in modern astronomy as a descriptor of a star's spectrum. Another property of the stars is that they all have different brightnesses. Stars which are further away appear to be fainter, however this does not give an indication of the intrinsic brightness, or luminosity, of the star. By using the parallax motion of a nearby star relative to the background during the orbit of the Earth around the Sun, a distance can be estimated. It is then possible to get a measurement of the luminosities of those stars. The luminosity of stars is typically referred to in units of the Sun's luminosity ($L_{\odot}$). By combining the intrinsic brightness of a number of stars with their spectral classification Hertzsprung (1911) and Russell (1914) independently discovered that there was a relationship between the spectral type of the star and its luminosity. This diagram plotting spectral class against luminosity proved to be an incredibly useful astronomical tool and

is commonly referred to as the Hertzsprung–Russell (HR) Diagram. A modern version of a HR diagram is shown in Figure 1.2.

1.1.1 From Spectral class to Temperature and Colour

In the modern HR diagram the spectral classification is generally replaced with the surface temperature of the star. This is both because there is a link between the temperature of the star's atmosphere and the spectral lines which will be present and because determining the temperature is a more precise measurement than a qualitative assessment of the spectrum. For a given temperature, T, the spectral energy density B_ν of a blackbody object, such as a star, has a characteristic curve as a function of wavelength, ν, arising from Planck's law (Equation 1.1)

$$B_\nu(\nu, T) = \frac{2h\nu^3}{c^2} \frac{1}{e^{\frac{h\nu}{k_B T}} - 1} \tag{1.1}$$

where c is the speed of light, h is the Planck constant (6.626×10^{-34} J s) and k_B is the Boltzmann constant (1.381×10^{-23} J K^{-1}).

A corollary of the Planck function is that the wavelength of light with the highest energy density decreases with increasing temperature, thus hotter stars appear blue, while cooler stars appear red. The peak wavelength is described by Wien's displacement law (Equation 1.2).

$$\nu_{\max}[\text{nm}] = \frac{2.897772 \times 10^6}{\text{T/K}} \tag{1.2}$$

By using this relationship, it can be seen that peak emission in a star with a surface temperature of 4,000 K is at a wavelength of around 724 nm (red), while a star with a surface temperature of 8,000 K emits most strongly at 362 nm (violet). This is why hot stars are typically described as blue, while cool stars are red. What Hertzsprung and Russell discovered was that for the vast majority of stars, there was a trend whereby the intrinsic luminosity of the stars increased for stars with higher surface temperatures. This line on which the vast majority of stars sit is called the Main Sequence (MS).

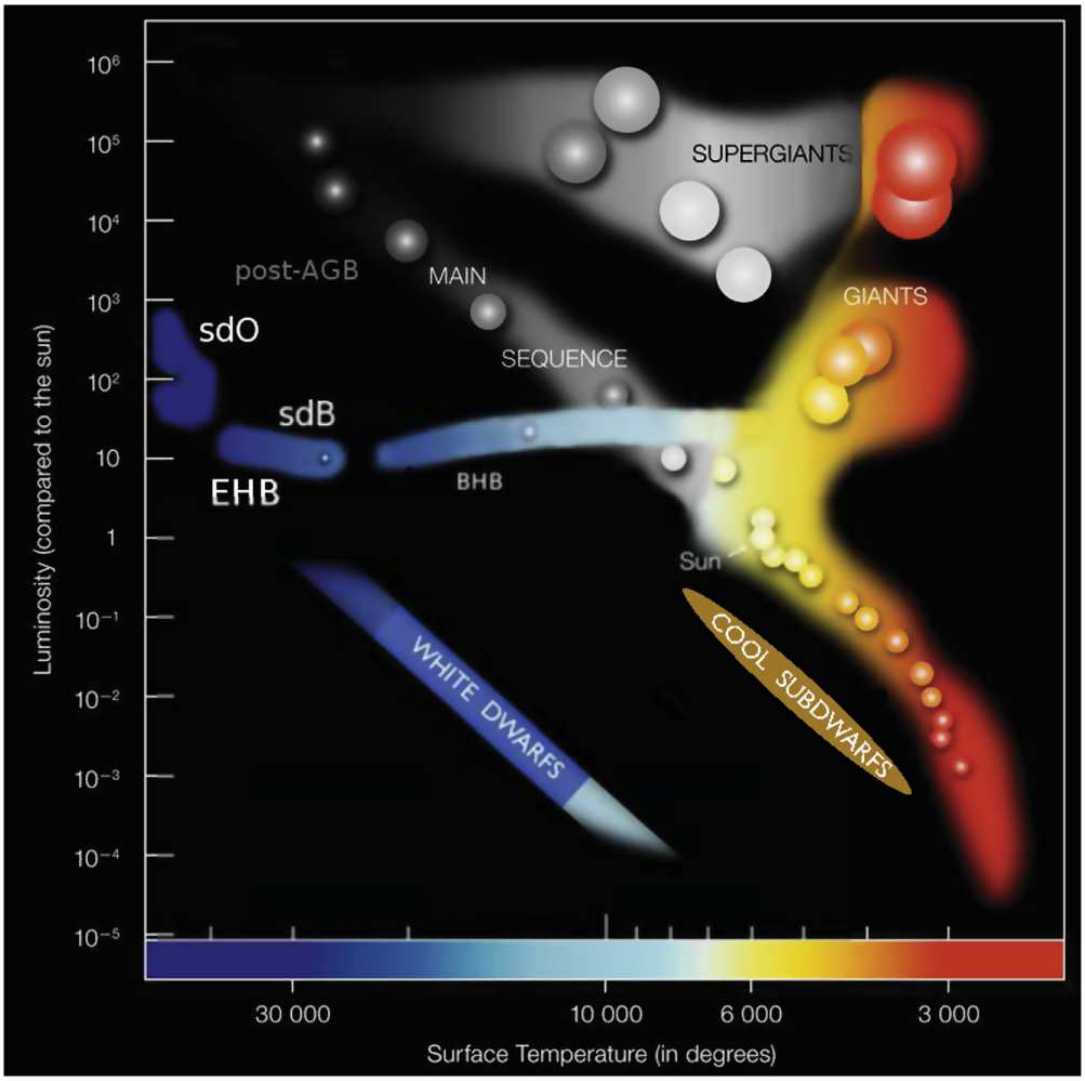

Figure 1.2: A $\log(L)$-$\log(\ T_{\rm eff})$ (or Hertzsprung-Russell) diagram illustrating the different sequences of stars, each representing a different evolutionary stage in the stellar life cycle. Republished with permission of Annual Reviews from Heber (2009). Permission conveyed through Copyright Clearance Center.

1.1.1.1 Definition of Stellar Surface and Effective Temperature

As the 'surface' of a star is poorly defined due to its diffuse outer layers, it is instructive to have a standard definition of where the stellar surface is. The most commonly used definition makes use of the Eddington approximation (Equation 1.3). The Eddington approximation considers an atmosphere where the absorbing power of the material is constant across all wavelengths and this assumption leads to the relation

$$T^4 = \frac{3}{4} T_{\mathrm{e}}^4 \left(\tau + \frac{2}{3} \right) \tag{1.3}$$

where τ represents the 'optical depth' of the material, a measure for how well radiation is able to escape through the atmosphere, and consequently is a measure of physical depth in the atmosphere. T_{e} indicates the 'effective temperature', that is the temperature of a perfect blackbody emitter which emits the same amount of radiative flux as the stellar atmosphere. From this we can see that for a value of $\tau = \frac{2}{3}$, the value of T_{e} is equivalent to T, and therefore at this depth, the temperature of the medium is identical to the effective blackbody temperature of the star. This value of τ corresponds to the depth at which the average photon experiences less than 1 scattering event before leaving the atmosphere and thus is a physically sensible choice of 'surface'. This 'effective temperature', or T_{eff}, is what is used in stellar astrophysics to describe the surface temperature of a star.

1.2 Stellar Structure

As well as discussing how to classify the stars, there was significant debate as to what the source of the Sun's energy was, and by extension the energy source of the stars. Lord Kelvin suggested that the Sun was emitting thermal energy as it slowly contracted, however the upper estimate of the lifetime of the Sun if that were the case was 200,000 years, a lifetime much shorter than that of the Earth. Ernest Rutherford expanded upon this and suggested the lifetime could be extended if extra heat was supplied to the Sun through radioactive decay of nuclei, which extended its possible lifetime to a couple of million years, still a few orders of magnitude short. It was not until the early 20^{th} century that the correct

energy source was identified, when Eddington (1920) proposed that nuclear fusion could provide sufficient energy to keep the Sun. This was confirmed by the description of the proton-proton chain, the fusion of two hydrogen nuclei (protons) to form a deuteron, by Bethe & Critchfield (1938) and the CNO cycle, where carbon catalyses the processing of hydrogen nuclei into helium nuclei described independently by von Weizsäcker (1938) and Bethe (1939). The temperatures and pressures in the core of the star are sufficiently high that atomic nuclei can overcome their Coulomb repulsion and fuse together to form heavier elements, releasing significant amounts of energy. These nuclear fusion reactions can power the Sun for billions of years, which agree much better with the estimates of the age of the Solar System determined from the age of the rocky material of the Earth and meteorites. By combining all of these ideas and observations, we can now provide a basic description of what a star is, namely a massive self-gravitating spheroid of matter (mostly hydrogen) which releases energy from its surface in the form of electromagnetic radiation and is fuelled by nuclear fusion reactions deep in its interior.

It is also possible to describe the basic structure of a star mathematically. The most fundamental way to do this is through the equation of mass continuity (Equation 1.4) which states that the mass contained within the system remains constant, the equation of hydrostatic equilibrium (Equation 1.5) which assumes the star is in an equilibrium state where the pressure of the fluid is balanced by the inward force of gravity at all depths within the star, the energy equation (Equation 1.6) which describes the generation of energy throughout the star and the equation of energy transport (Equation 1.7) which details how the energy of the star is transported between regions in the star. These equations can be described in either Eulerian form (variation with respect to radius, r) or Lagrangian form (variation with respect to mass, m).

$$\frac{dm}{dr} = 4\pi r^2 \rho \qquad \frac{dr}{dm} = \frac{1}{4\pi r^2 \rho} \tag{1.4}$$

$$\frac{dP}{dr} = -\frac{GM\rho}{r^2} \qquad \frac{dP}{dm} = -\frac{Gm}{4\pi r^4} \tag{1.5}$$

$$\frac{dl}{dr} = 4\pi r^2 \rho \epsilon \qquad \frac{dl}{dm} = \epsilon \tag{1.6}$$

$$\frac{dT}{dr} = -\frac{4\pi G \rho^2 T r}{3P}\nabla \qquad \frac{dT}{dm} = -\frac{GmT}{4\pi r^4 P}\nabla \tag{1.7}$$

The symbol ∇ represents the partial derivative, $\frac{\partial \ln T}{\partial \ln P}$ which takes the form

$$\nabla = \nabla_{rad} = \frac{3k\rho}{4acT^3}\frac{l}{4\pi r^2} \quad \text{in radiative equilibrium,} \tag{1.8}$$

$$\nabla = \nabla_{ad} = \frac{\gamma}{\gamma - 1} \text{ if fully convective} \tag{1.9}$$

where γ is the adiabatic index of the gas ($\gamma = \frac{5}{3}$ for a fully ionised ideal gas).

In order to solve these equations a set of boundary conditions are required. By definition, these are: $m(r = 0) = 0$, $l(r = 0) = 0$, $P(r = R_*) = 0$ and $T(r = R_*) = T_{\text{eff}}$, where l is the luminosity as a function of mass or radius coordinate. To complete the system of equations, expressions are also needed for the other quantities mentioned in the equations; the opacity, κ, the rate of energy generation, ϵ, density, ρ, and energy transport, ∇. These additional properties generally depend on P, T and the abundance of chemical elements, X_{i}. These equations provide a method for computing the entire structure of a star as a static object.

1.2.1 Energy Transport

The differing forms of the energy transport equation (1.7) highlight that different methods of energy transport exist within a star, depending on the conditions. The three ways of transferring energy are by conduction, convection and radiation. Energy transport by radiation is where the energy in the star is transferred by photons (and neutrinos). This is generally very efficient at transferring energy, except in cases where the density is very high (therefore the mean free path of a photon becomes very short) or when the opacity of the material gets very

high (often due to the presence of an ionisation zone). Generally, this radiative equilibrium is a stable configuration of the material in the star as long as the condition

$$\nabla < \nabla_{ad} \equiv \frac{\gamma - 1}{\gamma}$$

is met. In the circumstances mentioned above, this condition is no longer satisfied, and the material becomes unstable to convection. The concept of convection can be understood by considering a small parcel of gas in the star, and what happens if it experiences a small increase in its temperature due to random fluctuation. Assuming it maintains pressure equilibrium with its surroundings, the parcel will expand adiabatically and become buoyant and rise. If the temperature gradient of the surrounding material is less than the adiabatic temperature gradient, then the parcel of material will become less dense at a rate slower than the surrounding material, lose its buoyancy and return to its original location. On the other hand, if the temperature gradient of the surrounding material is greater than the adiabatic temperature gradient, the parcel will continue to rise. Eventually, it will reach thermal equilibrium by transferring energy to the surrounding medium, thus transporting energy outwards. Likewise, in such an environment, a piece of material which experiences a decrease in temperature will lose its buoyancy and sink. Consequently, convective regions in a star not only transport energy, but also transport material. Energy transport by conduction is unimportant in most stars and only plays a notable role in white dwarf stars, when electrons transfer heat from the inert core to the surface of the star where it escapes, causing the star to cool.

1.3 Stellar Evolution

A star's fuel reserves are of course not unlimited, and therefore the energy budget of a star will change when it can no longer fuse hydrogen. This has the implication that the observable characteristics of stars must evolve and change over their lifetime. Stars are formed when clouds of gas and dust collapse due to their own gravity. As the dust cloud contracts, central regions reach high temperatures and pressures and hydrogen can fuse to form helium. Stars spend the majority of

their lifetime ($\sim 90\%$) on the Main Sequence, powered by the fusion of hydrogen into helium.

Based on observations of eclipsing binary star systems, where mass, radius and luminosity can be accurately determined, it is known that there is an empirical relationship between the luminosity of a star and its mass.

$$L \propto M^{\beta} \tag{1.10}$$

From observations the value of β is known to be between 3.5 and 4 for most stars. For massive stars over 50 times the mass of the sun ($\mathrm{M}_{\odot}$), the value of β is much closer to 1, while for Main Sequence stars with a mass less than $0.43\,\mathrm{M}_{\odot}$ β is measured to be around 2.3. Using the value of $\beta = 3.5$, we can derive an empirical relationship between the mass of a star and its lifetime on the Main Sequence, as this is roughly proportional to its mass (amount of fuel/energy available) divided by its luminosity (rate of energy loss)

$$\tau \propto \frac{M}{L} = \frac{M}{M^{\beta}} = M^{1-\beta} \approx M^{-2.5} \tag{1.11}$$

Thus it can be seen that massive stars live for significantly less time than low-mass stars. For example, knowing that a star having the same mass as Sun ($1\,\mathrm{M}_{\odot}$) has a Main Sequence lifetime of around 10 billion (10^{10}) years, we find that a star of about $16\,\mathrm{M}_{\odot}$ has a lifetime of just 10^7 years, while a star of $0.5\,\mathrm{M}_{\odot}$ will live for around 5.6×10^{10} years, almost six times longer than the Sun.

Once this fuel is exhausted in the core, the star begins fusion in a shell around the core. As the core is no longer producing energy, it contracts while the outer layers expand, meaning the star gets brighter and cooler (redder) and becomes a red giant which can be 100-200 times the radius of the Sun ($\mathrm{R}_{\odot}$). The hydrogen burning shell burns outwards through the outer layers of the star (envelope) and the helium core grows in mass. These stars are located on the Red Giant Branch of the HR diagram (refer to Figure 1.2), and in fact by understanding stellar evolution, we shall see that a stars location on the HR diagram is generally a good way to determine a star's evolutionary status.

Low mass stars ($< 0.5\,\mathrm{M}_{\odot}$) eventually reach a point where the hydrogen burning shell can no longer sustain fusion as the outer layers are not hot enough, and

most of the material has been converted to helium. The star then cools and contracts, becoming a helium white dwarf (He-WD). As we know from the mass-lifetime relationship discussed above, single stars of this mass will not yet have reached the end of their Main Sequence lives, as it takes longer than the current age of the Universe (~ 14 billion years) for them to exhaust their hydrogen fuel.

For stars with a mass of at least $0.8\,\mathrm{M}_\odot$ and less than around $8\,\mathrm{M}_\odot$, the core reaches a temperature of $\sim 10^8\,\mathrm{K}$ at which point it becomes possible for multiple helium nuclei to fuse together to form carbon, nitrogen and oxygen, providing another source of energy. The red giant contracts and appears on the horizontal branch (HB) during this phase of core helium burning. The star's location on the HB is dependent on the envelope of hydrogen which remains around the helium-burning core. Stars with lower mass envelopes appear to the hotter (bluer) end of the HB. As with hydrogen, when the core runs out of helium, fusion moves to a shell and the star expands and ascends the asymptotic giant branch (AGB) with an inner helium-burning shell and an outer hydrogen-burning shell. The energy produced by converting helium to heavier elements is less efficient and thus the helium core burning phase of evolution is about 10 times shorter than the MS lifetime. Once the star has exhausted this fuel, these stars eject their hydrogen-rich outer layers in a planetary nebula and become carbon-oxygen white dwarfs (CO-WD).

Stars with mass $\gtrsim 8\,\mathrm{M}_\odot$ can continue fusing heavier elements in their cores, becoming supergiant stars after leaving the MS. Fusion of elements heavier than iron does not lead to a release of energy, thus once the star has formed iron in its core, it has run out of available fusion energy. At this point the star is no longer able to support its own weight and begins to collapse. The material then reaches a point where the central density is equivalent to that of nuclear material and protons and electrons combine to form neutrons, emitting a neutrino. In these extreme conditions, the opacity of neutrinos becomes non-zero and the neutrinos provide some support to the core, halting its contraction. The in-falling material of the outer layers collides with the dense material in the core, producing a highly energetic supernova explosion. The remaining core forms either a neutron star or a black hole.

All of the aforementioned evolutionary scenarios are the typical evolutionary routes for a star if we assume it is evolving in isolation, with no complications arising from external factors. Examples of such external factors include where the star gains or loses material through mass transfer with its companion, where the star is actually the product of a merger of two stars, where the star is perturbed due to an event such as a supernova in its vicinity or where the star's trajectory takes it close to a massive objects such as black hole which can significantly disrupt the star. As we will see in Sections 1.7 and 1.8, the implications of close binary evolution will be of key importance for the objects of interest in this thesis.

The equations discussed in Section 1.2 determine the structure of the star. In order to establish what happens over time, time-dependent processes also need to be considered. One example is thermodynamic change to the temperature and radius as the star evolves. Work done to expand or contract the star contributes to a change in the energy output from the stellar surface.

These considerations leads to modifications to the energy equation (Equation 1.6) to account for the energy absorbed or released by a region of the star due to this change. This expression can be attained through thermodynamic considerations;

$$dE = -dS = -(dU + PdV) \tag{1.12}$$

meaning Equation 1.6 should be rewritten as

$$\frac{dl}{dm} = \epsilon - T\frac{dS}{dt} = \epsilon - \frac{dQ}{dt} \tag{1.13}$$

thus yielding a time dependence in the energy equation. Another important example of time dependence is the change in composition of a star as a function of time. It is clear that as the star fuses hydrogen into helium in the star, the abundance of hydrogen in that region will decrease. One example of how this is achieved is through the proton-proton chain, which ultimately uses 4 hydrogen nuclei to produce a single nucleus of helium, with some intermediate steps. If the overall rate of the fusion reaction is described by r_{pp}, the rate of depletion of hydrogen can be written as

$$\frac{dX}{dt} = -4m_u r_{pp} \tag{1.14}$$

where X is used to represent the fraction of mass constituted by hydrogen, and m_u is the atomic mass unit, representative of the mass of a hydrogen nucleus. The negative sign indicates that the reaction leads to a depletion of hydrogen and the factor of $4m_u$ highlights that the reaction consumes 4 hydrogen nuclei. The conversion of hydrogen to helium means the fraction of mass composed of helium must increase by a corresponding amount

$$\frac{dY}{dt} \simeq -\frac{dX}{dt} \tag{1.15}$$

where Y is used to refer to helium. This amount will not be precisely identical as other nuclear reactions may also be taking place. The metallicity of a star (amount of material other than hydrogen and helium) is typically represented by the letter Z. Elemental abundances can also be modified by mixing processes such as convection, discussed in Section 1.2.1 above, and atomic diffusion, which will be discussed in Section 1.5.

1.4 Chemically Peculiar Stars

The amount of a given chemical element on the surface of a star (its abundance) can be determined by looking at the spectrum of the electromagnetic radiation emitted by the star. The strength of lines in the spectrum associated with a particular element can be used to calculate the quantity of the element present in the atmosphere. If an element is more abundant in a star, it would be expected to absorb more radiation and produce a deeper absorption line in the spectrum than a star which has less of the element in its atmosphere. As the star most familiar to us, the Sun is often taken as the 'standard' to which we compare all other stars. This is a reasonable approach, as the relative abundances of elements in the Galaxy are approximately similar. However, there are many types of star where elements have abundances significantly different from that of the Sun. Figure 1.3 shows all of the regions of the HR diagram in which chemically peculiar stars have been observed. As can be seen from this figure, there are chemically peculiar stars in practically every region of the HR diagram.

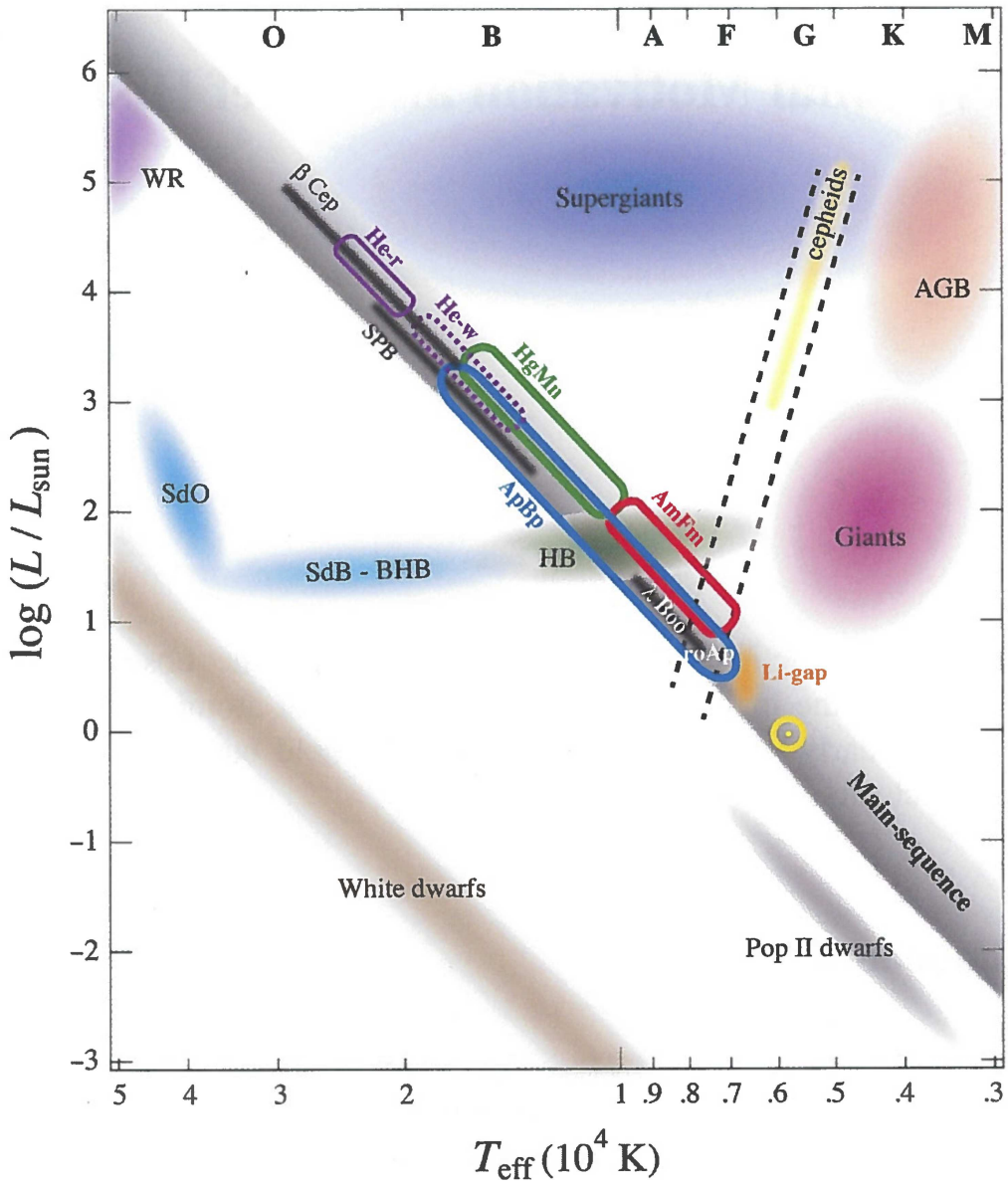

Figure 1.3: A HR diagram showing the types of chemically peculiar stars currently known. Different coloured regions/boxes indicate the location of different groups of peculiar stars. Figure reprinted by permission from Springer Nature Customer Service Centre GmbH: Springer, *Atomic Diffusion in Stars* by Michaud, G., Alecian, G. and Richer, J., © (2015). This source also provides further details on the different groups of stars identified in the diagram.

Giant and supergiant stars show enhanced helium and nitrogen abundances, AmFm and HgMn stars are main sequence stars which show unusual metallic elements on their surface, horizontal branch stars appear to have helium abundances which are lower than normal and some white dwarfs show spectra which indicate a surface composed almost entirely of hydrogen. There are a number of mechanisms which can produce abundance anomalies. Surface abundance anomalies in giant and supergiant stars are due to macroscopic particle transport mechanisms such as convection, where deep mixing of material can 'dredge up' partially processed material from shell-burning regions below. Anomalies in Horizontal Branch, MS and white dwarf stars are generally caused by transport of material through microscopic processes such as atomic diffusion (Michaud *et al.*, 2015).

1.5 Atomic Diffusion

Diffusion processes were speculated to take place in the atmospheres of stars as early as the 1920s, when it was suggested that the atmosphere of the star is supported by radiation pressure (Eddington, 1930).

The derivation of a diffusion velocity for a species i in a hydrogen-dominated environment begins with the assumption that at equilibrium, the partial pressure of i is balanced with the forces acting on it, such that

$$\frac{\partial p_{i,eq}}{\partial r} = n_i F_i \quad . \tag{1.16}$$

These forces are gravity, acting inwards, radiation pressure, acting outwards, and as we are dealing with ionised material, there is also an electric force. Hence,

$$F_i = -m_i g + m_i g_{i,rad} + Z_i e E \ . \tag{1.17}$$

Taking the derivative of $\ln(p_i)$ with respect to position, and using the definitions of gas pressure ($p = nkT$) and atomic mass ($m_i \equiv A \times m_p$),

$$\frac{\partial \ln(p_i)}{\partial r} = \frac{(-A_i m_p g + A_i m_p g_{rad,i} + Z_i e E)}{kT} \ . \tag{1.18}$$

The partial pressure of a species, p_i can be related to its concentration, c_i, which

for the hydrogen-dominated case is

$$c_i = \frac{p_i}{p_i + p_p}, \quad . \tag{1.19}$$

One may assume that the diffusion velocity, v_D, of a species will be linearly proportional to the difference between its present concentration gradient and its equilibrium gradient;

$$v_D = D_{ip} \left[\frac{\partial \ln(c_{i,eq})}{\partial r} - \frac{\partial \ln(c_i)}{\partial r} \right] . \tag{1.20}$$

Making use of Equation 1.19 and assuming $p_p \gg p_i$,

$$v_D = D_{ip} \left[\frac{\partial \ln(p_{i,eq})}{\partial r} - \frac{\partial \ln(p_{p,eq})}{\partial r} - \frac{\partial \ln(c_i)}{\partial r} \right] . \tag{1.21}$$

Substituting in Equation 1.18 and simplifying:

$$v_D = D_{ip} \left[\frac{A_i m_p}{kT} (g_{rad,i} - g) + \frac{(Z_i + 1)eE}{kT} - \frac{\partial \ln(c_i)}{\partial r} \right] . \tag{1.22}$$

By considering an electron and proton mixture with negligible g_{rad}, it can be shown that

$$eE = \frac{(m_p + m_e)g}{2} \approx \frac{m_p g}{2} . \tag{1.23}$$

A thermal component can also be added to account for thermal diffusion, giving the final expression for the diffusion velocity (Aller & Chapman, 1960),

$$v_D = D_{ip} \left[-\frac{\partial \ln(c_i)}{\partial r} + \frac{A_i m_p}{kT} (g_{rad,i} - g) + \frac{(Z_i + 1)}{2kT} m_p g + \kappa_T \frac{\partial \ln(T)}{\partial r} \right] . \tag{1.24}$$

Values of v_D are typically in the range of 10^{-6} to $10^{-2}\,\mathrm{cm\,s^{-1}}$. Equation 1.24 shows that a number of properties can affect the motion of material. The first term in Equation 1.24 indicates that the concentration of an element is important. Diffusion seeks to smooth out concentration differences and this is known as *concentration diffusion*. The final term indicates the role of temperature gradients and the star will try to smooth out temperature gradients (*thermal diffusion*). In the case of the stars being studied in this work, the thermal diffusion coefficient is negligible and the atmosphere is typically dominated by either hydrogen or helium, thus neither thermal diffusion nor concentration diffusion are significant in this work. The second and third term represent the inwards force of gravity (*gravitational settling*) and the outward force arising from the opacity of the

material as it absorbs the outgoing radiation, which imparts momentum on the ions (*radiative acceleration*).

A large amount of data is needed in order to compute the diffusion velocities, the g_{rad} term in particular. This requires calculation of the absorption cross-sections and energy levels of neutral and ionised atoms across a large range of energies to determine the opacity of the material across all wavelengths. As each atomic species has a different structure and set of energy levels, they experience different radiative forces from the radiation they absorb providing an outward acceleration. This differs from the inwards force due to gravity which depends more simply on the mass of the atom. If the outwards force from radiation is larger than the gravitational force, that element will move outwards. This process is called *radiative levitation* and it was first proposed as a mechanism for producing the chemical peculiarities seen in chemically peculiar A-type MS stars by Michaud (1970). Radiative levitation can also take place deeper in the envelope of a star and impact on its behaviour in a number of ways, including contributing to the driving of pulsations.

1.6 Stellar Pulsations

Classifying stars by their brightness and temperature is a useful way to identify their evolutionary state. However, there are many stars which are known to vary in brightness over short periods of time, relative to their evolutionary timescale. There are a number of reasons why these stars may vary and these are generally separated into extrinsic and intrinsic variables. Extrinsic variables stars are objects where the brightness variations are due to the motion of the star and its stellar or planetary companions, rather than any changes in the actual energy output of the star. Examples of such systems include eclipsing binary systems, where the measured brightness of a system can change as one object passes in front of the other along the line of sight of the observer. Intrinsic variables are stars which vary due to processes internal to themselves. These can include eruptions (such as solar flares), explosions (such as supernovae) and pulsations, which are of most relevance to this thesis. For an appropriate set of conditions, a star may periodically change in shape, leading to heating and cooling on the stellar

surface as the star contracts and expands respectively, thus causing brightness variations in the star. This is what is referred to as pulsations. A HR diagram showing all the different classes of pulsators is shown in Figure 1.4.

1.6.1 Driving Mechanisms

Pulsations have a number of different driving mechanisms and restoring forces. The main driving mechanisms for pulsations are convective blocking mechanism the opacity (or κ) mechanism and the ϵ mechanism (Aerts *et al.*, 2010).

1.6.1.1 Convective Blocking

The convective blocking mechanism is where energy builds up in the interior of a star at the bottom of a convective zone. This traps the outward-travelling radiation and energy builds up at the base of the convective zone. The star heats and expands, at which point the trapped energy can escape. Once the energy is released, the star contracts and cools, causing the energy to be trapped once more. Convection is important for pulsations in cool, luminous red giant stars such as Mira variable stars. Pulsations can also be stochastically excited in a star by convective motion at the surface. This is a mechanism for exciting variability in the Sun and other solar-like oscillators.

1.6.1.2 ϵ-Mechanism

The ϵ-mechanism, is so-called as it is the rate of nuclear energy generation (typically referred to as ϵ) which causes the variations. As the star burns its fuel it heats up and more energy is generated. This causes the star to expand, which in turn leads to a drop in temperature in fusion region and the nuclear reaction rate decreases, causing contraction. This cycle repeats, leading to pulsations. This mechanism has the potential to be important in stars with very thin regions of energy production, where small perturbations could have significant effect. There are no currently confirmed cases of ϵ-mechanism pulsations being observed in stars, although it has frequently been proposed as an explanation for new classes of pulsating stars (e.g. Miller Bertolami *et al.*, 2011).

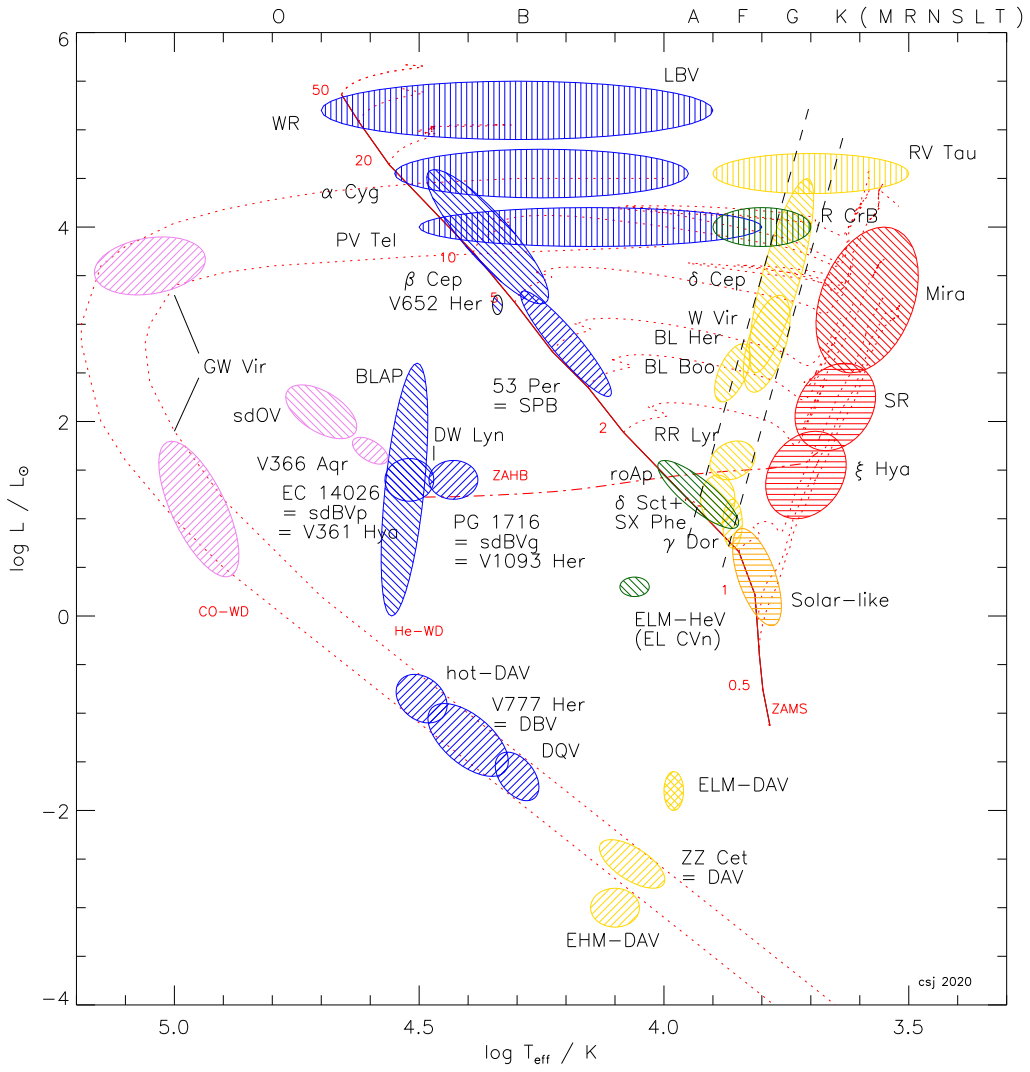

Figure 1.4: *Left:* A HR diagram illustrating all currently known regions of instability and the types of stars to be found in them, as of 2013. The upper x-axis denotes the corresponding spectral types of the stars at a given temperature. Backslash markings (\) indicates p-mode pulsators, while slash markings (/) indicate g-mode pulsators. Solar-like pulsators are indicated by horizontal lines (–) and luminous pulsators with irregular pulsations are indicated by vertical lines (|). Explanations of the acronyms of the categories of pulsator shown in this diagram as well as detailed information on their properties can be found in Aerts *et al.* (2010). Figure credit: C. S. Jeffery, private communication.

1.6.1.3 κ-Mechanism

The κ mechanism is where a region of highly opaque material serves as the block against the outflow of energy from the star. In the context of astrophysics, opacity refers to the ability of the material to absorb radiation as it moves outwards through the star. There are a number of different forms of opacity; bound-bound opacity (absorption of a photon of a specific energy, moving an electron to a higher energy level), bound-free opacity (absorption of a high energy photon, liberating an electron), free-free opacity (absorption of a photon by a free electron) and electron scattering (altering the trajectory of a photon, delaying its escape from the star). Each of these forms of opacity inhibit the escape of radiative energy from the star.

In general, opacity in the stellar interior decreases with increasing temperatures. At certain temperatures, some partially ionised elements show an increase in opacity with temperature. These 'opacity bumps' can be seen at 1.5×10^4 K, 4×10^4 K and 2×10^5 K and are due to the partial ionisation of hydrogen (H I), hydrogen and helium (H II and He I) and iron group elements (Fe, Ni and others) respectively.

For material at temperatures close to these opacity bumps, as they heat up, the opacity increases, leading to a trapping of heat energy. This results in more heating until the opacity decreases and the trapped energy can escape and the region of the star cools and expands again. The repetition of this cycle leads to pulsations as the surface area of the star (and thus its temperature and brightness) fluctuates.

1.6.2 Period-Mean Density Relationship

The time taken for an acoustic (sound) wave to travel through a star gives a good first approximation to the pulsation period (Π) of a star:

$$\Pi = \frac{2R_*}{c_s} \tag{1.25}$$

The sound speed, c_s, in the star can be approximated by:

$$c_s = \sqrt{\frac{\gamma P}{\rho}} \tag{1.26}$$

where γ is the adiabatic index, obtained from the ratio of heat capacities at constant pressure and volume respectively. For a monoatomic gas with 3 degrees of freedom, $\gamma = \frac{5}{3}$, and this is generally a good approximation to make for stellar material.

To derive an expression for the pressure, P as a function of radius, we solve the equation of hydrostatic equilibrium (1.5) where the mass, M, is replaced by $\frac{4}{3}\pi r^3 \rho$.

$$\frac{dP}{dr} = -\frac{4}{3}\pi G \rho^2 r \tag{1.27}$$

To simplify the system further so that only one quantity is varying over radius, we will assume a constant density in the star, represented by $\overline{\rho}$, the mean density. Integrating this over r gives:

$$P(r) = -\frac{2}{3}\pi G \overline{\rho}^2 r^2 + \text{Constant}. \tag{1.28}$$

Applying the boundary condition that pressure is zero at the surface of the star, $P(r = R) = 0$, one finds that the constant of integration is $\frac{2}{3}\pi G \overline{\rho}^2 R^2$.

$$P(r) = \frac{2}{3}\pi G \overline{\rho}^2 (R^2 - r^2) \tag{1.29}$$

Inserting Equation 1.29 into the expression for sound speed (Equation 1.26) gives an expression for the sound speed as a function of radius:

$$c_s(r) = \sqrt{\frac{2\gamma\pi G\overline{\rho}(R^2 - r^2)}{3}} \tag{1.30}$$

Placing Equation 1.30 into Equation 1.25 and integrating the sound speed from the centre to the stellar radius allows us to compute the pulsation period:

$$\Pi = 2\int_0^R \left(\frac{2\gamma\pi G\overline{\rho}(R^2 - r^2)}{3}\right)^{-\frac{1}{2}} dr \tag{1.31}$$

By moving the constant terms outside the integral we are left with

$$\Pi = \sqrt{\frac{3}{2\gamma\pi G\overline{\rho}}} \int_0^R (R^2 - r^2)^{-\frac{1}{2}} dr, \tag{1.32}$$

which is a standard integral with result $\pi/2$. Thus:

$$\Pi = \sqrt{\frac{3\pi}{2\gamma G\overline{\rho}}}. \tag{1.33}$$

This gives a relationship between period and mean density of $\Pi \propto \overline{\rho}^{-\frac{1}{2}}$, or equivalently

$$\Pi \left(\frac{\rho}{\rho_\odot}\right)^{\frac{1}{2}} \approx Q \tag{1.34}$$

where Q is termed the "pulsation constant". Q is not strictly a constant as it can vary through fluctuations in γ and deviations in the structure of the star. As an example, if one uses the mass and radius of the red giant variable Mira ($1.18\,\mathrm{M}_\odot$, $\sim 350\,\mathrm{R}_\odot$) one obtains a value of 1.05 years for the pulsation period, which agrees roughly with the observed period of 0.91 years.

1.6.3 Theory of Stellar Oscillations

Observations of pulsating stars are helpful for developing our understanding of the internal structure of stars. One method for doing so is to determine the normal modes of oscillation of a star and calculate whether these modes can pulsate.

1.6.3.1 Normal Modes of Oscillation

Stars are spherical in shape and thus perturbations to their shape will take the mathematical form of spherical harmonics to satisfy periodic boundary conditions on the surface. The simplest form of a spherical harmonic is a radial mode. This is simply where the star expands and contracts, maintaining spherical symmetry. It is also possible for stars to pulsate in non-radial modes. The shapes of these spherical harmonics can be found from the expression:

$$Y_\ell^m(\theta, \phi) = N_\ell^m P_\ell^{|m|}(\cos\theta) e^{im\phi} \tag{1.35}$$

Where ϕ and θ are the polar longitude and latitude respectively, N_ℓ^m is the normalisation constant for a particular mode, and $P_\ell^{|m|}$ is the Legendre polynomial for that mode.

The letters ℓ and m refer to the number of node lines (lines between expanding and contracting parts of the surface at which no motion is observed) on the stellar surface. ℓ is known as the *spherical degree* of the mode, and represents the total number of node lines present on the surface. m is the *azimuthal order* and is the number of node lines which intersect the stellar equator. For a given value of ℓ, the azimuthal order can vary within the range $[-l, l]$, with the sign on the number indicating the direction of travel of the pulsations relative to the rotation of the star itself. The $\ell = 0$ modes are referred to as radial modes. Modes of azimuthal order 0 are commonly referred to as axisymmetric modes. Modes with $|m| = \ell$ are named sectoral modes, while all other modes can be considered as tesseral modes.

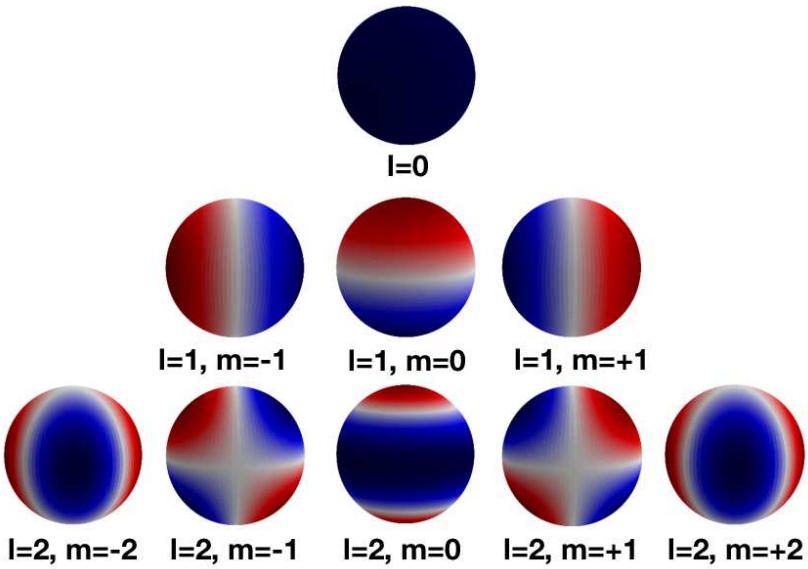

Figure 1.5: A schematic showing the spherical harmonics up to a spherical degree of $\ell = 2$. The pale regions indicate the positions of node lines on the surface. Image: Own work.

There is also a third quantity, labelled by k, called the *radial order* which is needed to fully describe a particular mode. This refers to the number of radial nodes which can be found within the star. A value of 0 for k gives the fundamental

mode, while $k = 1$ is the first overtone mode, analogous in 2 dimensions to the fundamental mode and first overtone mode vibrations in a plucked string fixed at both ends. Figure 1.5 gives a visual representation of the first few spherical harmonics. The combination of k, ℓ and m can be used to uniquely identify an individual pulsation mode, and thus can be considered as 'pulsational quantum numbers'.

1.6.3.2 Linearised Equations of Stellar Pulsation

To determine the normal modes of oscillation of a star, one should derive the equation of motion for an oscillating star. This can be derived by considering a small perturbation to the stellar structure equations (Section 1.2)

The equation of motion is derived using an approach known as linearisation, and a number of assumptions and approximations are made in its derivation. An illustration of how this is achieved can be shown in the linearisation of the mass continuity equation (Equation 1.4). A small perturbation is added to the radius and the density ($r = r_0 + \delta r$, $\rho = \rho_0 + \delta\rho$), where $\delta m/m_0,\ \delta\rho/\rho_0 << 1$where the zero in the subscript indicates the equilibrium position of the star.

$$\frac{\partial\left(r_0 + \delta r\right)}{\partial m} = \frac{1}{4\pi\left(r_0 + \delta r\right)^2\left(\rho_o + \delta\rho\right)} \tag{1.36}$$

By expanding the terms in the equation and ignoring terms which are a product of two perturbation terms (δr^2 or $\delta r\delta\rho$), one obtains the expression

$$\partial r = 4\pi r_0^2\rho_0\delta m\left(1 + 2\frac{\delta r}{r_0} + \frac{\delta\rho}{\rho_0} + \frac{\partial\delta r}{\partial r_0}\right) \tag{1.37}$$

where one can recognise the left hand side and the first term on the right hand side as the original formulation of the mass continuity equation. Simplifying and defining $\zeta = \frac{\delta r}{r_0}$:

$$\frac{\delta\rho}{\rho_0} = -3\zeta - r_0\frac{\partial\zeta}{\partial r_0} \tag{1.38}$$

which is the linearised form of the perturbed mass continuity equation in Eulerian coordinates. A similar approach can be taken with the other equations. Naturally, if the star is in motion, the equation of hydrostatic equilibrium (Equation 1.5) is

no longer valid and an acceleration term is introduced, arising from the imbalance between pressure and gravity produced by the perturbation (Equation 1.39).

$$\frac{d^2r}{dt^2} = \ddot{r} = -4\pi r^2 \frac{dP}{dm} - \frac{Gm}{r^2} \tag{1.39}$$

Using the same approach as for the mass continuity equation, the linearised form of Equation 1.39 can be derived

$$\frac{d^2}{dt^2}(\delta r) = 4\zeta \frac{Gm}{r_0^2} - 4\pi r_0^2 \frac{d\delta P}{dm} \tag{1.40}$$

1.6.3.3 Approximations

Note that in this section, we only consider radial pulsations. That is to say, we assume spherical symmetry and that the perturbation is in the radial axis. Derivation of the pulsation equations for non-radial pulsations (for pulsation quantum numbers where $l > 0$) requires separate terms for perturbations in the radial and transverse directions. For detailed derivations of the complete set of pulsation equations, one can consult a textbook on stellar oscillations (e.g. Aerts *et al.*, 2010; Unno *et al.*, 1989).

Another simplification that can be made in dealing with these equations is to assume that the perturbation to the gravitational potential as a result of the stellar motion can be neglected. This is referred to as the Cowling approximation after Cowling (1941). This simplifies a number of the equations from fourth order differential equations to second order equations, thus making calculations simpler and more efficient.

1.6.3.4 Adiabatic Oscillations

A key assumption of the adiabatic approach is that no heat is transferred by the perturbation. That is to say, from Equation 1.13, $\frac{dQ}{dt} = 0$. This is the most important distinction between the adiabatic and non-adiabatic approach, and simplifies the energy equation as there is now a simple expression to relate pressure and density, $\frac{\delta P}{P_0} = \Gamma_1 \frac{\delta \rho}{\rho_0}$. Applying this to the linearised equation of

motion, one can obtain the linear adiabatic wave equation (Equation 1.41) which depends only linearly on the perturbation, ζ.

$$\frac{d^2\zeta}{dt^2} = -(3\Gamma_1 - 4)\frac{Gm}{r_0^3}\zeta \tag{1.41}$$

By guessing that the solutions to the wave equation are of the form

$$\zeta(m,t) = \xi(m)e^{-i\omega t}, \tag{1.42}$$

where ω is the angular frequency of the oscillation, one arrives at the result:

$$\frac{d^2\zeta}{dt^2} = -\omega^2\xi \implies \omega^2 = -(3\Gamma_1 - 4)\frac{Gm}{r_0^3} \tag{1.43}$$

This solution highlights that for certain values of Γ_1, ω is imaginary:

$$\text{if } \Gamma_1 < \frac{4}{3} \implies \omega^2 < 0 \implies \omega \text{ imaginary, dynamically unstable} \tag{1.44}$$

$$\text{if } \Gamma_1 > \frac{4}{3} \implies \omega^2 > 0 \implies \omega \text{ real, oscillatory motion possible} \tag{1.45}$$

Very massive stars ($M > 50M_\odot$) have values of Γ_1 approaching and exceeding $\frac{4}{3}$ and are thus dynamically unstable. In lower mass stars, it is possible for periodic motion to occur, as Γ_1 is generally close to $\frac{5}{3}$. The linear adiabatic wave equation can be written in the form:

$$\mathscr{L}(\xi(m)) + \omega^2\xi(m) = 0 \tag{1.46}$$

which is the form of a Sturm-Liouville type equation. This type of equation has well-known mathematical solutions with eigenvalues ξ_i and eigenfrequencies ω_i. One notable property of these solutions is that when the eigenfunctions are ordered by their eigenfrequencies, an increase in ω gives an increase in the number of nodes. Another property is that if ω increases, $\frac{d\xi}{dm}$ and $\frac{d^2\xi}{dm^2}$ also increase. So for large ω and thus higher mode orders, the gradients of pressure and temperature will be larger. Large gradients in P and T lead to more energy dissipation due to friction forces in the material. This means dissipation of energy is quite prevalent in high mode orders (high frequencies). This helps to explain why most stars pulsate only in their fundamental mode and/or in modes of low radial order.

1.6.3.5 Non-Adiabatic Oscillations

These results described above are a result of the assumption that the perturbations are 'ideal' and adiabatic. While such an ideal case is seldom found in nature, the adiabatic model is sufficient to provide information about the periods of oscillation in which a star could pulsate, generally to a high degree of accuracy. However, it cannot provide any information about whether or not these modes are excited and will pulsate. To get information about the actual excitation of these modes in the star, a non-adiabatic model needs to be considered. As discussed in the adiabatic case, the temperature and pressure gradients caused by the perturbations lead to damping. Thus even the low frequency oscillations would eventually be completely damped. The non-adiabatic analysis allows determination of regions which provide (consume) energy and therefore drive (damp) the perturbations.

To find the non-adiabatic results, the solutions are once again guessed to take the form $e^{i\omega t}$. However this time, ω is defined to be complex, $\omega = \omega_r + i\omega_i$. By substituting this into the proposed solution:

$$e^{-i\omega t} = e^{-i(\omega_r + i\omega_i)t} = e^{-i\omega_r t} e^{\omega_i t} \tag{1.47}$$

This means the solutions now comprise an oscillatory term ($e^{-i\omega_r t}$) and an exponential term ($e^{\omega_i t}$). The exponential term allows the stability of the mode to be determined by looking at the value of ω_i.

$$\text{if } \omega_i < 0 \implies e^{\omega_i t} \to 0 \text{ as } t \to \infty, \text{ stable mode} \implies \text{no pulsations} \tag{1.48}$$

$$\text{if } \omega_i > 0 \implies e^{\omega_i t} \to \infty \text{ as } t \to \infty, \text{ unstable mode} \implies \text{pulsations} \tag{1.49}$$

Therefore, for an unstable mode, if one begins with a small perturbation, the restoring force will return the system to equilibrium. This will generate a perturbation in the opposite direction, with a magnitude greater than the initial one, thus causing the amplitude of the perturbation to grow, causing a noticeable pulsation. If the mode is stable, the restoring force will yield an inverse perturbation which is smaller than the initial one, and the amplitude will decay and become non-existent. Therefore, once one has carried out a non-adiabatic analysis of a

stellar model, the stability of its modes of pulsation can be determined by examining the sign of the imaginary part of the eigenfrequencies. This is the method used in Chapters 4 and 5 to determine the stability of the analysed pulsation modes.

By considering the equation of energy conservation, derived as a linearised version of Equation 1.13

$$\frac{d}{dt}(\delta Q) = \delta\epsilon - \frac{d}{dm}(\delta L) \tag{1.50}$$

it can be seen that if the quantity $\frac{d}{dt}\delta Q$ is positive, heat is gained by the system (and vice versa) during one cycle. By computing this quantity over each mass element in the star, one can compute the total work done in one pulsation period.

$$W = \oint_{t=0}^{t=\Pi} \int_0^{M_*} \frac{d}{dt}(\delta Q)\, dm \tag{1.51}$$

This is defined as the *work integral*, W, of the pulsation and it is the work done by the pressure and gravity forces on all of the mass of the star.

If W is positive, energy is gained over the period of oscillation. This energy gain is the extra energy necessary to drive the pulsation and allow it to grow in amplitude. If W is negative, the star loses energy in the course of the oscillation and will be damped. Analysis of the work integral over small mass elements will also allow damping and driving regions within the star to be identified. By comparing it to other properties of the star, such as elemental abundances and opacity, it is possible to make a diagnosis of the driving mechanism responsible for the pulsations.

1.6.4 Restoring Forces and Modes of Propagation

An alternate approximate formulation of Equation 1.40 is

$$\frac{d^2\xi}{dr^2} = \frac{\omega^2}{c_s^2}\left(1 - \frac{N^2}{\omega^2}\right)\left(\frac{S_\ell^2}{\omega^2} - 1\right)\xi \tag{1.52}$$

where N and S_ℓ are the Brunt Väisälä and Lamb frequency (for mode order ℓ) respectively. These are the two characteristic frequencies of the stellar material. N represents the buoyancy frequency at which a blob of material will oscillate if

perturbed. This is unstable in convective regions and N^2 will be negative in such situations. S_ℓ is related to the acoustic frequency of the medium, being directly proportional to the sound speed. Oscillatory solutions ($\frac{d^2\xi}{dr^2} < 0$) are found when ω^2 is either greater than both N^2 and S_ℓ^2 or less than both N^2 and S_ℓ^2.

In these regimes, one of the characteristic frequencies will typically dominate over the other, thus providing two different forms of pulsations, characterised by their restoring forces, namely pressure and gravity. Oscillations are referred to as p-modes or g-modes depending on their respective restoring force. Pressure modes involve motion of material in a radial direction, and affect material closest to the surface. Gravity modes involve motion in a transverse direction, where the buoyancy provided by gravity acts as the restoring force. These modes can probe into the deep interior of the star.

This can be illustrated in what is referred to as a 'propagation diagram'. An example of this is shown in Figure 1.6 which shows two example models, which are presented in Chapter 4. In this diagram, the Brunt Väisälä and Lamb frequency (for $\ell = 1$) are plotted as a function of fractional stellar radius. The regions below both curves and the region above both curves are shaded, indicating the regions in a star where pulsations can propagate. This provides an illustration that g-modes are typically of lower frequency and propagate more often towards the centre of the star, while p-modes are of high frequency and generally propagate in the outer regions of the star. The convective regions near the surface of these stars are also noticeable as N vanishes at those locations as the material has no stable buoyancy frequency. In both cases it can be seen that for frequencies between 10^2 and 10^4 μHz, it is possible for a pulsation mode to propagate in both the g-mode zone and the p-mode zone. These modes are referred to as mixed modes. It should also be noted that radial modes ($\ell = 0$) are a special case, and do not couple to buoyancy forces (motion is only in the radial direction), and thus a propagation diagram provides limited insight in those cases.

1.7 Hot Subdwarf Stars

Hot subdwarf stars are a type of star with an unusual evolutionary history. Their basic properties are summarised in Table 1.1. First observed in the 1950s, these

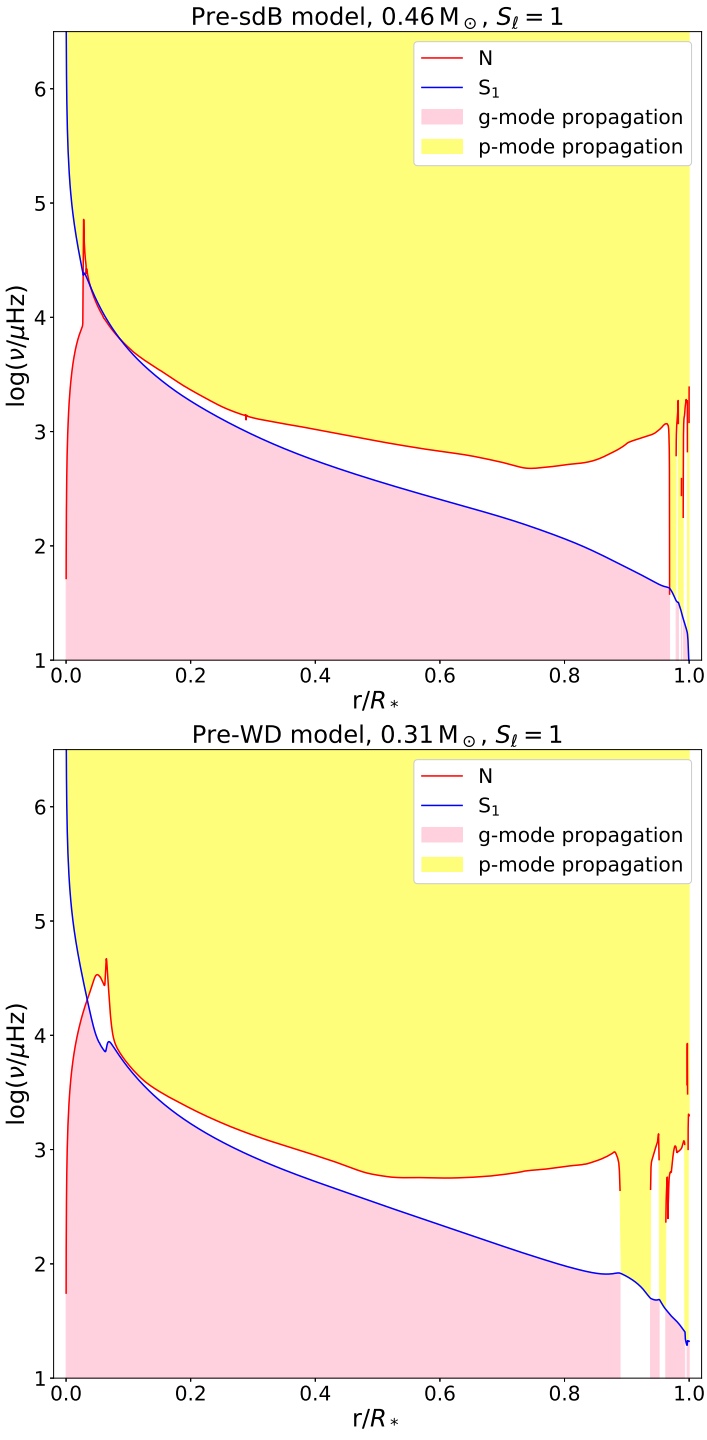

Figure 1.6: Mode propagation diagram for $\ell = 1$ for two representative models presented in Chapter 4. The p-mode and g-mode propagation regions are highlighted in light yellow and light magenta respectively.

Table 1.1: Main characteristics of hot subdwarf stars

Property	Typical Value
Mass	$0.47\ M_\odot$
Envelope Mass	$\lesssim 0.02\ M_\odot$
Radius	$0.15 - 0.25\ R_\odot$
Surface gravity (log g)[cm s^{-2}]	$5.0 - 6.5$
Surface Temperature [K] ($T_{\rm eff}$)	$20\,000 - 40\,000$ K (sdB)
	$40\,000 - 80\,000$ K (sdO)

'faint blue stars' were found to be deficient in hydrogen (Greenstein & Sargent, 1974). Analysis of their temperature and surface gravity found that they lie beyond the hotter (bluer) edge of the horizontal branch (sdB and sdO in Figure 1.2), in the Extreme Horizontal Branch (EHB). This led to the conclusion that they are helium core burning stars, and are not very massive. They are much hotter than other HB stars as they only have very low mass hydrogen envelope ($\lesssim 0.02\,M_\odot$). The fact that they are core helium burning stars implies that they have passed the end of their Main Sequence phase and grown a helium core of about $0.47\ M_\odot$. Because of their blue colour and evolved state, they are the primary source of ultraviolet radiation in old stellar populations (Brown *et al.*, 1997). A detailed review of current understanding of hot subdwarf stars has been written by Heber (2016).

1.7.1 Formation Channels

From observed parameters and their location on the HR diagram, hot subdwarfs have been identified as hot, compact and low mass stars. One of the biggest mysteries surrounding these stars is their formation. The biggest question is how a star that was massive enough to form a core of almost half a solar mass and ignite helium can become a low mass object with almost no hydrogen remaining. This puzzling behaviour has led to the formulation of several possible mechanisms by which these objects may have originated. Applying single star evolution processes outlined above cannot produce a hot subdwarf star. There are three proposed evolutionary channels for hot subdwarf formation and all of them involve the interaction of a star with a binary companion (Han *et al.*, 2002, 2003). These

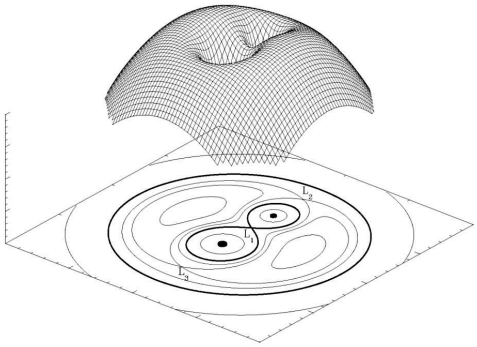

Figure 1.7: Schematic representation of Roche lobes in a binary star system. Credit: Wikimedia Commons / Marc van der Sluys / CC BY-SA 3.0[1]

channels are generally referred to as common envelope ejection (CEE or CE ejection), Roche Lobe overflow (RLOF) and double white dwarf mergers.

1.7.1.1 Roche Lobe Overflow (RLOF)

The Roche lobe of a star in a binary system is the region in space in which matter is gravitationally bound to it. Figure 1.7 shows the Roche lobes of a binary system. If a star expands beyond the extent of its Roche lobe, mass will begin to transfer onto the companion star.

If two MS stars, or one MS star and a white dwarf are in close binary orbit, then mass will be transferred from the MS star (primary star) to its low mass companion (secondary star) when it expands and becomes a red giant, overflowing its Roche Lobe. Depending on the orbital parameters and how the stars respond to this mass transfer, this can be a stable process. If these changes lead to a widening of the orbit, mass transfer will eventually stop as the star will reach a point where it is no longer filling its Roche Lobe. This method of transferring mass is called the RLOF method, and can produce hot subdwarfs in comparably wide binary orbits, as most of the star's hydrogen envelope will have been transferred to its companion. Han *et al.* (2002) suggest that orbital periods of up to 1000 days would be expected for subdwarfs from the RLOF channel. A schematic illustration of this is provided in Figure 1.8.

[1] `http://creativecommons.org/licenses/by-sa/3.0/`

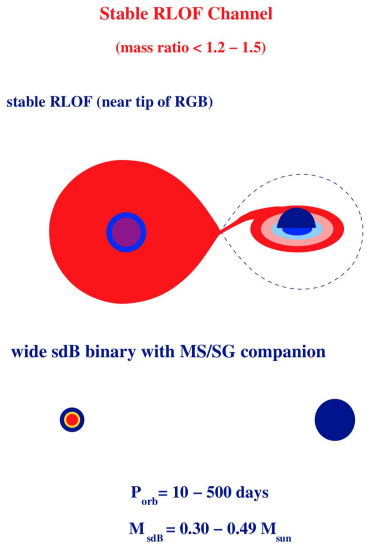

Figure 1.8: Schematic illustrating the formation of a hot subdwarf via the RLOF evolution channel. Credit: Podsiadlowski *et al.* (2008).

1.7.1.2 Common Envelope Ejection

The ejection of a common envelope is a mechanism proposed by Paczyński (1976) as a possible way a large amount of mass could be ejected from a binary system. Like in the RLOF case, this feature of binary evolution occurs in systems where the stars are in a relatively close orbit. As described by Han *et al.* (2002), CE ejection typically takes place when the radius of the star undergoing a loss of mass is increasing faster than the radius of its Roche lobe. This is the opposite of the RLOF case, where the radius of the star expands at a slower or similar rate to the Roche lobe, thus regulating the transfer.

In the CE case, this unstable situation leads to rapid mass transfer and as a consequence the transferred matter forms a shared envelope (or common envelope) around the red giant core and the low-mass companion. Friction develops between the two cores and the envelope, causing the radius of their orbit to decrease and producing thermal energy. If the energy released is sufficient, the envelope will be ejected leaving the nearly-naked degenerate core of the giant and its companion in a very close binary system. If the helium core is sufficiently large

to ignite helium, the star will become a hot subdwarf. If the core is less massive, the star will evolve to become a low-mass white dwarf. sdBs with orbital periods of $\lesssim 10$ days are achievable by CE ejection according to Han *et al.* (2002). It is also possible that massive planets could cause a CE event. According to Charpinet *et al.* (2011), the Kepler-70 system consists of 2 planets in very close orbits around an sdB star. These are possibly the cores of gas giant planets which remained after the planets were engulfed in the star when it became a red giant, and this may have triggered the CE ejection. The common envelope phase of evolution remains poorly understood, with 3-dimensional hydrodynamic models often disagreeing on the amount of material that can actually be removed in such an interaction. A recent review of the physics of CE ejection has been written by Ivanova *et al.* (2013). A schematic diagram of the formation of a short-period sdB+MS binary and a short-period sdB+WD binary via CE ejection is shown in Figure 1.9. This figure illustrates two routes to forming an sdB star through CE evolution. In this figure, moving downwards indicates moving forwards in time. In the scenario shown in the left column, there initially is a close binary system composed of two MS stars of reasonably similar masses, The more massive star evolves faster and begins transferring mass to its companion, becoming a He-WD with its MS companion in a relatively wide binary orbit. Subsequently, the MS star evolves to become a red giant, and this large expansion leads to the formation of a CE, removing most of the outer layers, resulting in a He-WD and hot subdwarf binary system. In the scenario shown on the right of the figure, there is a larger difference in mass between the two stars, so no mass trnasfer takes place prior to the more massive star reaching the RGB. On the RGB, the star expands and engulfs it's low mass companion, and the envelope is ejected. In this situation the outcome is a hot subdwarf star in a close binary orbit with a low-mass Main Sequence companion. The formation of sdBs and low-mass white dwarfs via CE ejection is the evolutionary channel of most interest in this thesis.

1.7.1.3 White Dwarf Merger

A binary system consisting of two white dwarfs can be formed following either one stable RLOF phase and a CE phase, or following two CE phases (Han *et al.* (2003) & references therein). If the orbital period of the system after this evolution is

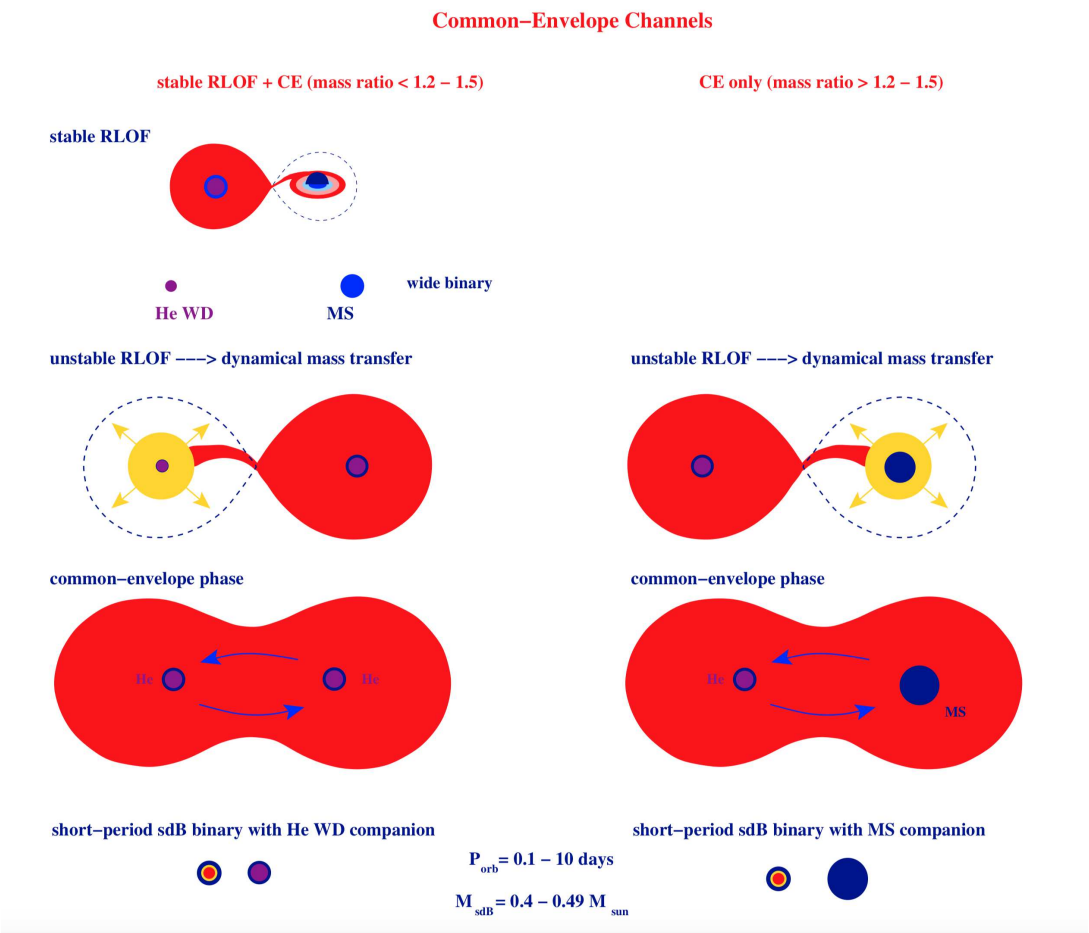

Figure 1.9: Schematic of two of the possible evolution channels for hot subdwarf stars. *Left:* Unstable mass transfer leading to common envelope ejection and a short period binary sdB+WD system. *Right:* Unstable mass transfer leading to common envelope ejection and a short period binary sdB+MS system. Credit: Podsiadlowski *et al.* (2008).

short enough, the orbital radius of the system will decay through gravitational radiation, eventually leading to the two objects merging. If the resultant object develops a sufficiently high internal temperature, helium ignition may take place and this leaves an sdB star in a single system. It has been suggested (e.g. Zhang & Jeffery, 2012) that white dwarf mergers are the main formation mechanism for helium-rich subdwarfs as stars produced this way are likely to be rich in helium. At least 50% of hot subdwarfs are believed to be in binary systems (Maxted *et al.*, 2001) and most have hydrogen-rich surfaces. The hydrogen-rich stars in binaries likely come from the other aforementioned evolutionary channels.

1.7.1.4 Enhanced Mass-Loss

It has also been suggested that a hot subdwarf can form as a single star through enhanced stellar winds, perhaps as a result of rapid rotation or high metallicity. Both the enhanced mass-loss and the WD merger channels are illustrated in Figure 1.10.

1.7.2 Chemically Peculiar Subdwarfs

Hot subdwarf stars all show peculiar surface compositions. Observational data shows that the amount of helium present on their surface can vary from ~ 0 to ~ 99 per cent. Interestingly, this appears to follow a trend, with helium abundance typically increasing at higher effective temperatures. This is highlighted in Figure 1.11, which plots hot subdwarf stars according to their surface helium number fraction, $\log [N(\mathrm{He})/\mathrm{N(H)}]$ and effective temperatures. The horizontal dashed line indicates the solar abundance of helium.

From this it can be seen that in general, most hot subdwarfs of spectral class B are helium poor, while some are helium rich. An even smaller number reside in an 'intermediate helium-rich' regime, with a helium fraction between 10% and 90%. Detailed spectroscopic studies of a large sample of hot subdwarf stars by Geier (2013) examined the abundances of many elements. Light elements such as carbon, nitrogen and oxygen were found to be typically under-abundant relative to the Sun, although a large scatter is found in carbon abundances. Intermediate mass elements such as aluminium and silicon are also under-abundant. Heavier

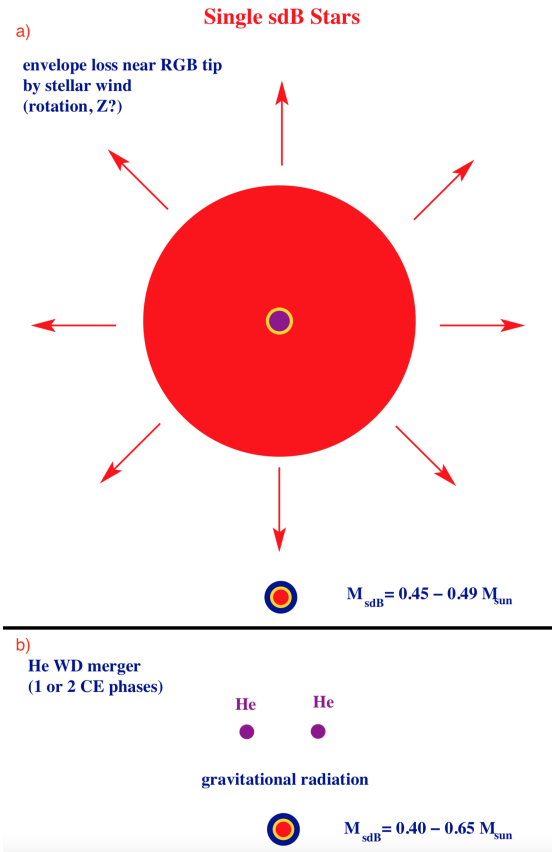

Figure 1.10: Schematic of the possible evolution channels for forming single hot subdwarf stars. *a):* Envelope removal through enhanced mass-loss, as a result of rotation or some other mechanism. *b):* A merger of two helium white dwarfs. Credit: Podsiadlowski *et al.* (2008).

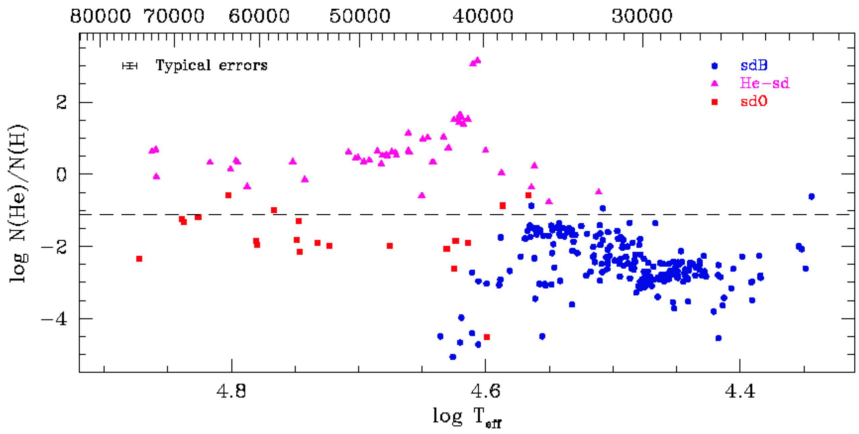

Figure 1.11: Distribution of atmospheric helium abundances in hot subdwarf stars as a function of effective temperature. Figure reproduced from Charpinet *et al.* (2009)[1], with the permission of AIP publishing.

elements such as scandium, titanium and chromium are found to be enriched, trending to stronger enrichments at higher effective temperatures. These trends in the heavier elements are understood to qualitatively agree with atomic diffusion studies in hot subdwarfs. Figure 1.11 shows the elemental abundances of some 'typical' hot subdwarfs to illustrate the general abundance patterns seen in these stars, relative to the solar values. While all hot subdwarfs show chemical peculiarities, a number of hot subdwarfs are exceptionally peculiar. Two interesting cases are LS IV-14°116 (Naslim *et al.*, 2011) and CPD-20°1123 (Naslim *et al.*, 2012). Along with having an intermediate helium abundance, CPD-20°1123 is also observed to be in a 2.3 day orbit with a companion star. Due to the short orbital period, it is quite likely that the star is a post-common envelope subdwarf. By studying the post-common envelope phase of evolution of a hot subdwarf progenitor, it may be possible to develop a better understanding of the evolutionary status of stars such as CPD-20°1123 by testing the suggestion that intermediate helium-rich subdwarfs may be pre-horizontal branch objects, which will only become depleted in helium when they reach the horizontal branch and gravitational settling causes the helium to sink from the atmosphere. LS IV-14°116 is another intermediate helium-rich subdwarf, which shows abundances of zirconium, stron-

[2]http://doi.org/10.1063/1.3246567

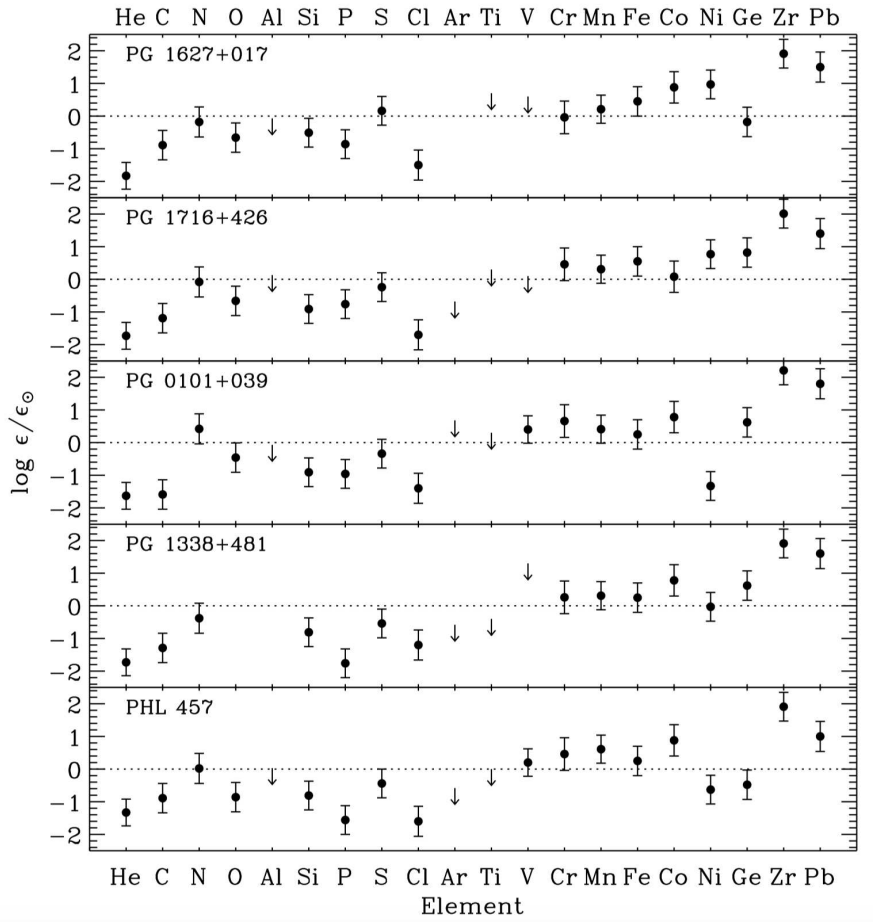

Figure 1.12: Abundances of some typical hot subdwarf stars on a logarithmic scale, where a value of 0 corresponds to the solar abundance. Credit: Blanchette *et al.* (2008), `http://doi.org/10.1086/533580`, © AAS. Reproduced with permission.

tium and yttrium which are 10,000 times that of the Sun. No companion has been found for the star, and the origins of these exotic elements is unclear. With the discovery of other similar objects, such as UVO 0825 (Jeffery *et al.*, 2017), Feige 46 (Latour *et al.*, 2019) and others (e.g. Dorsch *et al.*, 2019), the total number of these 'heavy-metal' subdwarfs is now greater than 10. The origin of this sub-population of hot subdwarfs and the reason behind their extraordinary surface chemistry remains unclear.

1.7.3 Pulsations in Hot Subdwarfs

sdB stars were first predicted to pulsate by Charpinet *et al.* (1996). It was proposed that these pulsations would be driven by the κ mechanism, specifically due to a Z-bump opacity caused by the ionisation of iron at the high temperatures associated with B class stars. The first pulsating sdB stars were discovered within a few months of their prediction (Kilkenny *et al.*, 1997). The variable stars that were discovered exhibited short period variability ($\Pi \sim 2 - 9$ minutes according to Kilkenny (2007), i.e. p-mode pulsators) and were seen in sdBs with $28,000 \leq T_{\rm eff} \leq 35,000$ K. These periods are comparable to those obtained by using the period-mean density relation (Equation 1.33) with the typical masses and radii of hot subdwarfs outlined in Table 1.1. The relation gives values of Π between 460 and 1,000 seconds (7 to 16 minutes), which is similar to the observations.

The heavy metal opacity bump was confirmed as the driving mechanism for these pulsations by Charpinet *et al.* (1997). This work also suggested that the metallicity in the envelope would need to be enhanced in order to cause significant driving of the pulsations. These enhanced metal abundances can arise as a consequence of atomic diffusion, and in particular radiative levitation. A similar process was also proposed by Fontaine *et al.* (2003) as a driving mechanism for the g-mode sdB pulsators, discovered by Green *et al.* (2003). These stars had much longer period variations ($\Pi \sim 60 - 120$ minutes) and were found in cooler sdBs, $T_{\rm eff} \lesssim 27,000$ K. A very small number of sdB stars have been observed to be hybrid pulsators (stars which exhibit both p- and g-mode pulsations), such as Balloon 090100001 (Oreiro *et al.*, 2004). These are located in the intermediate region between the short-period and long-period pulsators.

It was later shown by Jeffery & Saio (2006b) that with the inclusion of more accurate opacity information for heavy metals (using Opacity Project opacities instead of older OPAL opacity tables), the presence of an overabundance of nickel in the driving region was a significant factor as well as iron and provided a better agreement between the temperature range in which pulsations are theoretically expected and that of the observed pulsators. Research has been carried out to look at the effects of diffusion and radiative levitation, and has found that these processes significantly alter the surface chemistry of these stars. A study of radiative levitation of horizontal branch stars found that hot subdwarfs should have surfaces which are depleted in light elements (Cl and below), while heavier elements should show super-solar abundances (Michaud *et al.*, 2011). Other theoretical studies applied radiative levitation and attempted to match observed hot subdwarf helium abundances to the result and found that turbulent mixing of the outer layers, or some mass loss, is needed in order to satisfy this restriction, however these come with the drawbacks of no longer matching pulsation instability strips and a lack of a physical mechanism for this mixing respectively (Hu *et al.*, 2011). This indicates that the interplay between diffusion physics and the pulsation properties of the resulting models is a key constraint with which to test the physics operating in the interior of these stars.

It is suggested that only about 10% of stars in the p-mode instability strip pulsate and around half of stars in the g-mode instability strip are variable. As the timescale for diffusion ($\sim 10^6$ years) is much shorter than the HB lifetime of the star ($\sim 10^8$ years), this raises the question of why not all sdB stars are observed to pulsate, and why there is a difference between the fractions of short-period and long-period pulsators in their respective instability strips. UV spectroscopy by O'Toole & Heber (2006) on pulsating and non-pulsating sdB stars and found no significant differences could be seen between the sdBs that pulsate and those that do not, so it is unclear how one could differentiate between variable and constant stars. One suggestion put forward by Jeffery & Saio (2007) is that the motion of material associated with the pulsations disrupts the material and moves the iron and nickel away from the driving region, causing the pulsations to cease. Since p-mode pulsations are vertical and g-mode pulsations are transverse, this is a

feasible explanation for why a larger portion of sdBs in the g-mode instability strip are observed to pulsate.

1.8 Low-Mass White Dwarfs

The mass distribution of white dwarfs shows a strong peak at around $0.6\,M_\odot$, with most white dwarfs having a mass between $0.5\,M_\odot$ and $0.7\,M_\odot$ (Kepler *et al.*, 2007). White dwarfs with a mass less than $\sim 0.5\,M_\odot$ are often referred to as low-mass white dwarfs. To form a white dwarf of such low mass through standard single-star evolution would take longer than the current age of the Universe, therefore they must form through binary interactions, as is the case with hot subdwarfs. The formation of low-mass white dwarfs through RLOF was explained by evolutionary calculations by Althaus *et al.* (2013), while the formation of low-mass white dwarfs which appear to be presently single stars, has been discussed by Kilic *et al.* (2007) and Justham *et al.* (2009). Some of these stars have been observed to pulsate (Hermes *et al.*, 2013), although the driving mechanism in this instance is the partial ionisation zone of hydrogen near the surface of the star. Additionally, some stars which have been identified as low-mass proto-WDs have also been observed to pulsate. Evolutionary modelling of extremely low mass pre-WDs has been carried out by Istrate *et al.* (2014) in the context of the timescales involved and the impact this has on the age determination of white dwarfs and also by Istrate *et al.* (2017), who focused on WASP 0247-25B, a pulsating pre-WD of around $0.18\,M_\odot$. As an eclipsing double-lined spectroscopic binary, WASP 0247-25B is representative of the EL CVn type double-lined eclipsing binaries which contain a pre-WD with an A- or F-type main-sequence companion (Maxted *et al.*, 2014). Another group of pre-WDs includes single-lined systems containing a pre-WD with an unseen CO-WD companion (Gianninas *et al.*, 2016). Both groups may have some connection to BLAPs and both contain pulsating variables; Jeffery & Saio (2013) argue that reduced hydrogen abundance in the envelope led to helium being the principle opacity driver. The evolution of EL CVn systems has also been examined by Chen *et al.* (2017).

1.8.1 Blue Large-Amplitude Pulsators (BLAPs)

The discovery of a new class of pulsating star was announced by Pietrukowicz *et al.* (2017) based on observations carried out by the OGLE (Optical Gravitational Lensing Experiment) survey of the stars in the Galactic bulge. These stars showed extraordinary brightness variations of 0.2-0.4 magnitudes on timescales of 20-40 minutes, and were dubbed Blue Large-Amplitude Pulsators (BLAPs) by the discoverers due to their blue colour. Follow-up observations of some of these stars found that they are hot, compact objects, similar to hot subdwarf stars, but with lower surface gravities. Spectroscopic measurements from a couple of these stars indicate that their surfaces are rich in helium. The fact that these hydrogen deficient objects pulsate is perhaps unsurprising given that opacity-driven radial pulsations are excited in many regions of the luminosity– $T_{\rm eff}$ plane when the damping influence of hydrogen is diminished (Jeffery & Saio, 2016). Pietrukowicz *et al.* (2017) suggested two theories of the structure of the star; a $\sim 1\,\mathrm{M}_{\odot}$ core helium-burning object, or a low-mass ($\sim 0.3\,\mathrm{M}_{\odot}$) shell hydrogen-burning object. The latter of these theories indicates an object which is in the pre-WD phase of evolution, indicating that it could be another group of pulsating, low-mass pre-WDs. A group of 4 similar large-amplitude pulsators were discovered by the Zwicky Transient Facility (ZTF) by Kupfer *et al.* (2019). This second group of objects, described as 'high-gravity BLAPs', have surface gravities of $5.3 \leq \log g/\mathrm{cm\,s^{-2}} \leq 5.7$, which is very similar to hot subdwarfs. However, the pulsation amplitudes of these high-gravity BLAPs are much higher than those usually seen in hot subdwarf pulsators and more similar to that of the original Pietrukowicz *et al.* (2017) BLAPs, and therefore there is uncertainty regarding their precise evolutionary origins.

A complete list of the properties of all currently known BLAPs is provided in Table 1.2, including the pulsation period, the effective temperature and surface gravity (where these have been measured). To contextualise these objects, they have been placed on a plot of surface gravity against effective temperature in Figure 1.13, alongside a sample of pulsating hot subdwarf stars for comparison. A number of suggestions have been made to explain what BLAPs are and have been examined. One proposal which has been examined is that BLAPs are low

Table 1.2: Observed properties of all known BLAPs.

Name	$T_{\rm eff}$/K	$\log g/{\rm cm\,s^{-2}}$	P (s)	Ref.
OGLE-BLAP-001	30 800	4.61	1695.6	1
OGLE-BLAP-002	–	–	1397.4	1
OGLE-BLAP-003	–	–	1707.6	1
OGLE-BLAP-004	–	–	1341.6	1
OGLE-BLAP-005	–	–	1635.0	1
OGLE-BLAP-006	–	–	2281.2	1
OGLE-BLAP-007	–	–	2110.8	1
OGLE-BLAP-009	–	–	2068.8	1
OGLE-BLAP-009	31 800	4.40	1916.4	1
OGLE-BLAP-010	–	–	1927.8	1
OGLE-BLAP-011	26 200	4.20	2092.2	1
OGLE-BLAP-012	–	–	2359.8	1
OGLE-BLAP-013	–	–	1695.6	1
OGLE-BLAP-014	30 900	4.42	2017.2	1
HG-BLAP-1	34 000	5.70	200.20	2
HG-BLAP-2	31 400	5.41	363.16	2
HG-BLAP-3	31 600	5.33	438.83	2
HG-BLAP-4	31 700	5.31	475.48	2

Souces: 1: Pietrukowicz *et al.* (2017), 2: Kupfer *et al.* (2019)

mass, helium-core pre-white dwarfs ($M \approx 0.3\,M_\odot$) which will evolve to have the same temperature and luminosities as the observed objects (Córsico *et al.*, 2018; Romero *et al.*, 2018) as they approach the white dwarf cooling track. Another suggestion which has been studied is that they are helium-core burning post-giants evolving toward the extended horizontal branch (Wu & Li, 2018). Detailed modelling of these stars including processes such as radiative levitation, which was not considered in the aforementioned studies, will be presented in Chapters 4 and 5.

1.9 Summary

The interdependence of evolutionary history, diffusion and pulsations in hot subdwarfs and other hot, low-mass stars presents an important topic to investigate.

One question is what effects the evolution channel of the progenitor of the hot

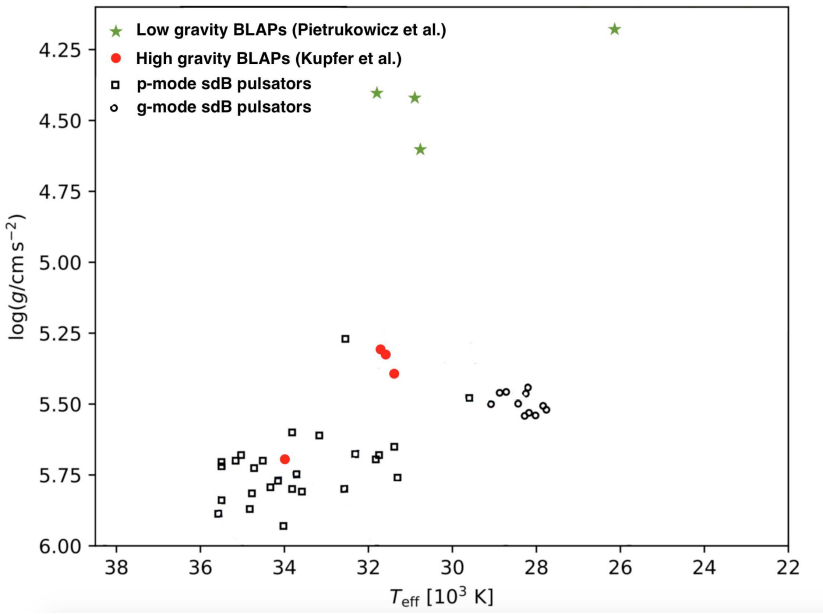

Figure 1.13: A surface gravity–effective temperature diagram showing the relative location of pulsating sdB stars and the two groups of BLAPs. Figure incorporates data from Kupfer *et al.* (2019).

subdwarfs have on the eventual properties of the subdwarf. The issue of atomic diffusion in hot subdwarfs has been studied previously. However, these studies never looked at the effects of diffusion in the transitional phase between the red giant branch and the horizontal branch. This is in part due to the limitations of code. Examining diffusion in this transitional phase would be a way to investigate the origins of intermediate helium-rich subdwarfs and other chemically peculiar subdwarfs.

Secondly, the discovery of a new category of pulsating star provides an exciting challenge for theoretical astrophysics. The similarities between hot subdwarfs and BLAPs mean that similar theoretical modelling techniques to those used on hot subdwarfs can be applied here to determine the evolutionary status of the BLAPs and the driving mechanism for their pulsations. Doing so will allow the origins of these rare and unusual objects to be probed and will provide suggestions for what sorts of objects could be expected to be found in large scale sky surveys.

1.10 Outline of Thesis

Chapter 2 outlines the structure and key capabilities of the computer programs used in this work. Chapter 3 applies these computational tools to the formation of hot subdwarf stars and investigates the role played by atomic diffusion in their formation. Chapter 4 applies similar methods to proto-white dwarf stars to investigate a newly discovered class of pulsating star, while Chapter 5 investigates this in greater detail in the context of the discovery of a wider group of objects and makes estimates of where more objects might be found in the future. The overall conclusions and a suggestion of areas for future work are outlined in Chapter 6.

2 Methodology

We want to compute how certain types of stars change over time and how they behave at different points during their lifetime. To accomplish this, we need to make use of a stellar evolution program and and a stellar oscillation program. This chapter outlines the computer programs used and the methods employed to produce models of the stars of interest.

2.1 Simulating Stellar Evolution

In order to calculate how a star will change over time, one must make use of a computer program which will simultaneously solve the equations of stellar structure and evolution, build up a numerical model of a star, calculate how each layer of the star will change and how the entire star will evolve. Many stellar evolution codes have been developed since the arrival of digital computing. Early examples include Henyey *et al.* (1959) and Kippenhahn *et al.* (1967). Advances in computer technology have led to the development of more advanced and sophisticated stellar evolution programs. An example of a state-of-the-art stellar evolution program is MESA[1] (**M**odules for **E**xperiments in **S**tellar **A**strophysics, Paxton *et al.*,

[1]Latest version and older releases available at `http://mesa.sourceforge.net`

2011, 2013, 2015, 2018, 2019), an open-source program which is constructed in a modular format, with numerous modules specialised to deal with microphysics (e.g. nuclear reactions, opacities), macrophysics (e.g. diffusion, convection) and numerical solvers (e.g. root finders, differential equation solvers). Each module is designed so that it can be used as a stand-alone tool for computational astrophysics. However, using them all together in the MESA STAR module provides a robust and detailed code which can carry out simulations of stellar evolution in 1 spatial dimension. MESA is written in the FORTRAN language, and makes use of the open-access OpenMP language (Open Multiple-Processing, Dagum & Menon, 1998) in order to utilise multiple processors on a computer in parallel in order to speed up computation. All subsequent mentions of MESA in this work refer to MESA STAR, unless otherwise stated.

MESA begins by reading instructions from the input files. Input files can contain a lot of different information, which can be separated into three main sections.

- Procedural instructions relating to the operation of the simulations, such as the location of an initial input model, what information to include in the output data and how often to record it, and how to make large scale adjustments to an input model before running the simulation. These instructions are generally placed in the `&star_job` portion of the input file.

- Choices related to the physics being used in the simulation. Examples of these sorts of options include initial stellar parameters, termination conditions, the mixing processes being used and their efficiency, how to treat stellar rotation, how mass loss is computed and controls relating to the nuclear reaction rates. These instructions are placed in the `&controls` portion of the input file.

- Various options relating to live-plotting of the simulation while it is running. This is achieved through the PGSTAR module of MESA and is controlled by the `&pgstar` portion of the input file. Image files of this output can be saved at regular intervals if the user requests it.

Additionally MESA also contains controls for binary-star evolution if one wants to compute a simulation of a binary system, either with detailed simulation of both stars, or simulation of one star orbiting a point mass. Options related to binary evolution such as mass transfer efficiency and angular momentum transfer can be specified there.

A one-dimensional model is then constructed in a series of layers from the surface to the core, with each layer (or cell) in the star having its own properties (temperature, pressure, etc.). If there is a region in the star where properties such as composition, temperature or pressure are changing rapidly, MESA will 're-mesh' the model and add extra cells to better resolve the steep gradients. Once the mesh is completed, the model will be adjusted to account for mass changes, composition is recalculated based on diffusion, convection and nuclear reactions and a new stellar structure is calculated. If the code is unable to converge to a stable stellar structure, it will repeat the calculation with a smaller time interval until a solution is found. This is one evolutionary 'step'. This process is iterated as many times as necessary until one of the user-defined stopping conditions is met and the final model is saved as an output. The user can also specify the frequency at which intermediate 'profiles' of the evolution are taken, and a history file summarising the key global properties of the star at regular intervals is also produced.

2.1.1 Physics Choices in MESA

The capabilities and functionality of MESA have improved and expanded over time. The release number of MESA and the important physics choices for the simulations carried out in this work will be outlined in each respective chapter. Here I outline the general features and options which are important for the simulations carried out in this thesis. The physical parameters chosen for this work are listed in Table 2.1. The options available and the motivation behind these choices are outlined in the following subsections (from 2.1.1.1 to 2.1.1.6)

Table 2.1: Physical parameters used in the simulations presented in this thesis.

Parameter	Value
Opacity Tables	Type 1 tables: Opacity Project (Opacity Project Team, 1995, 1997) Type 2 tables: Not used as evolution beyond core helium ignition not studies
Composition	Grevesse & Sauval (1998) composition mixture with $Z = 0.02$
Convection	Schwarzschild criterion is used to determine convective boundaries Semiconvection, convective overshooting and thermohaline mixing have been ignored
Mass Loss	No mass loss, i.e. $\dot{M} = 0$ before and after CEE $\dot{M} = 10^{-3}\,M_\odot\,yr^{-1}$ during CEE with the `relax_mass` flag in MESA
Atomic Diffusion	None ('basic' models) Gravitational settling, Thermal and Concentration Diffusion ('standard' models) 'Standard' models with radiative levitation ('complete' models)
Nuclear Astrophysics	Isotopes included: ^{1}H, ^{4}He, ^{12}C, ^{14}N, ^{16}O, ^{20}Ne, ^{24}Mg, ^{40}Ar, ^{52}Cr, ^{56}Fe and ^{58}Ni Fusion reactions for ^{1}H (pp-chain and CNO cycle) and ^{4}He (triple-α process)

2.1.1.1 Opacity

To make evolutionary calculations efficient, the opacity of each cell is not directly calculated in each iteration. Instead, tabulated opacity data is used, with different tables for differing compositions, and a tabulated value of opacity depending on the temperature and density of the cell. For normal ranges, opacity data from the OPAL project (Iglesias & Rogers, 1996) or the Opacity Project (OP, Opacity Project Team, 1995, 1997) can be used. The work in this thesis makes use of the OP opacity data as this provides the additional data needed in order to carry out radiative levitation calculations, outlined below. This choice of opacity data was made in order to use the same data source for the tabulated opacity data (for models without radiative levitation and high temperature regions where levitation is not computed) and the monochromatic data for levitation calculations, providing a direct illustration of the effects of radiative levitation.

2.1.1.2 Composition

MESA provides a number of different values for the standard solar composition, including those of Grevesse & Noels (1993), Grevesse & Sauval (1998) and Asplund *et al.* (2005). Each of these represent a different determination of the abundance of the chemical elements, based on observation and modelling of the solar photosphere. In this thesis, the composition of Grevesse & Sauval (1998) is used, as it is well reconciled with the results of helioseismology (asteroseismology of the Sun). Ultimately, when atomic diffusion is taken into account, the composition profile of the model is significantly modified and bears no resemblance to the initial composition. For this reason, the choice of composition will not have a significant effect on the results. The choice of metallicity for the initial mixture may lead to different results as a lower metallicity will provide a smaller reservoir of material for radiative levitation to operate on, and this could reduce the potential for κ-mechanism driven pulsations.

2.1.1.3 Convective Mixing

Convection is treated in MESA using the standard mixing length theory described in Chapter 14 of Cox & Giuli (1968) and is treated as a diffusive process. Addi-

tionally, MESA can calculate mixing due to composition gradients (semiconvection and thermohaline mixing) and has numerous methods of dealing with the mixing of material beyond the boundary of convective regions (convective overshooting). However, none of these additions to the standard treatment of convection have been considered in this work. Neglecting these additional mixing processes will affect the outcome of these simulations in a limited way. Including these additional mixing processes may provide a mechanism to reduce the effectiveness of atomic diffusion, as will be discussed in Chapter 3. The extra mixing may also increase the fraction of models which become helium rich subdwarfs, which will be discussed in Section 3.4.3. The main effect of ignoring these other mixing processes would be to shorten the core-burning phases of evolution, as less material will be mixed into the core, providing additional fuel. As the objects studied in this work either never achieve a helium-core burning phase, or if they do, the evolution is not followed to the end of this phase, this should have minimal impact on the evolution of the models.

2.1.1.4 Mass Loss

A number of different mass-loss schemes can be used in MESA. For winds in low-mass stars, the most commonly used schemes are those of Reimers (1975) (for RGB stars) and Blöcker (1995) (for AGB stars). The CE ejection in these models means that any mass loss on the RGB due to stellar wind has negligible effect on the outcome as all of the mass will be removed anyway. In the post-CE phase of evolution, the stars are generally not very luminous and therefore do not have strong stellar winds. Consequently, no mass loss by stellar wind was included in these simulations. The ejection of the common envelope is modelled using the artificial `relax_mass` algorithm in MESA, which uses an extremely high mass loss rate of $10^{-3}\,\mathrm{M}_{\odot}\,\mathrm{yr}^{-1}$ to remove the outer layers of the star. Mass loss rates in hot subdwarfs are typically understood to be very low. Unglaub & Bues (2001) estimated the mass loss rates for hot subdwarfs from weak radiation-driven winds to be between $10^{-13} - 10^{-14}\,\mathrm{M}_{\odot}\,\mathrm{yr}^{-1}$. More detailed modelling showed that the actual rates could be even lower, but if that is the case, the wind may be fractionated, with metallic elements being preferentially lost from the surface (Unglaub, 2008). As the comparatively short pre-subdwarf phase of

evolution ($< 10^7$ yr) is one of the primary interests in the work, these mass loss rates are unlikely to cause too lead to materially different results compared to the zero mass-loss approach taken in this thesis. Given their comparable effective temperatures and surface gravities, the low-mass pre-white dwarf models are likely to have similar mass-loss rates, although this has not been analysed in detail. However, it can be acknowledged that fractionated metallic winds provide another mechanism with which to moderate the effects of atomic diffusion, by limiting the accumulation of iron-group elements in the stellar envelope.

2.1.1.5 Atomic Diffusion

Radiative levitation was added to MESA in Paxton *et al.* (2015). Radiative levitation is implemented using the methods outlined by Hu *et al.* (2011), who made similar modifications to the STARS stellar evolution code (Eggleton, 1971; Pols *et al.*, 1995; Stancliffe & Eldridge, 2009). These modifications make use of the monochromatic opacity data available in the OP data set. This enables calculation of radiative accelerations of each element in each cell, and thus allows simulation of the effects of radiative levitation during the course of evolution, which has been demonstrated to play an important role in hot subdwarf stars.

2.1.1.6 Nuclear Astrophysics

MESA contains a comprehensive network of over 350 nuclear reactions, along with data on thermonuclear and weak nuclear reactions. The choices of reactions and isotopes to be included in a simulation can easily be modified, with 'basic' networks being provided by the developers as a platform from which users can add or remove particular reactions or isotopes. As the stars of interest in this work are low-mass hydrogen-burning and/or helium-burning stars, only the relevant nuclear reactions were included. These are all of the stages of the proton-proton chain and the CNO cycle for hydrogen burning (as outlined in Section 1.2) and the triple-α process for helium burning. The isotopes included in this work are ^{1}H, ^{4}He, ^{12}C, ^{14}N, ^{16}O, ^{20}Ne, ^{24}Mg, ^{40}Ar, ^{52}Cr, ^{56}Fe and ^{58}Ni. This selection of elements encompasses those which are relevant for nuclear reactions and the overall stellar structure (H, He, C, N and O), those which are important for

diffusion and pulsation driving (Fe and Ni) as well as a number of elements of intermediate mass which can be used as further tracers of the effects of diffusion (Ne, Mg, Ar and Cr).

2.1.2 Producing Stellar Evolution Models with MESA

Carrying out a stellar evolution calculation with MESA comprises a number of steps, the process is shown in schematic form in Figure 2.1. The first step is to provide it with the input data and instructions. As outlined above, this includes instructions on the physical and computational parameters to be used in the simulation. MESA then computes an evolutionary 'step' and updates the structure of the star (Section 2.1.2.1). Once MESA has successfully taken a time step , the data from this step is written and the code checks whether any of the termination conditions have been met. If the conditions are not met, MESA will iteratively take more time steps until a termination condition is reached.

2.1.2.1 Numerical Method for a Stellar Evolution Time Step

The numerical approach to computing stellar evolution taken in MESA is based on that of Henyey *et al.* (1959). This is an efficient method for iteratively determining the structure of a stellar model. One first divides the star up into a 'grid' or 'mesh' of discrete points at mass co-ordinates throughout the star, forming a set of 'cells'. These do not have to be evenly spaced, and are usually preferentially arranged to resolve changes in the stellar structure such as the transition between the core and different burning shells, for example. Numerically, an evolution 'step' comprises 4 stages. Firstly, the model is prepared for a time-step by arranging the grid of points according to the current stellar structure. This ability to dynamically 'remesh' the mass cells in the model is one of the strengths of MESA.

Secondly, the changes to the properties of each cell in the model are accounted for. These include mass loss or gain, material transport due to diffusion and convection and composition changes due to nuclear reactions. The calculated changes are used as a trial solution to a linearised version of the stellar structure equations, where the derivatives have been replaced by finite differences to account for the discrete nature of the model. As this is unlikely to be a perfect solution

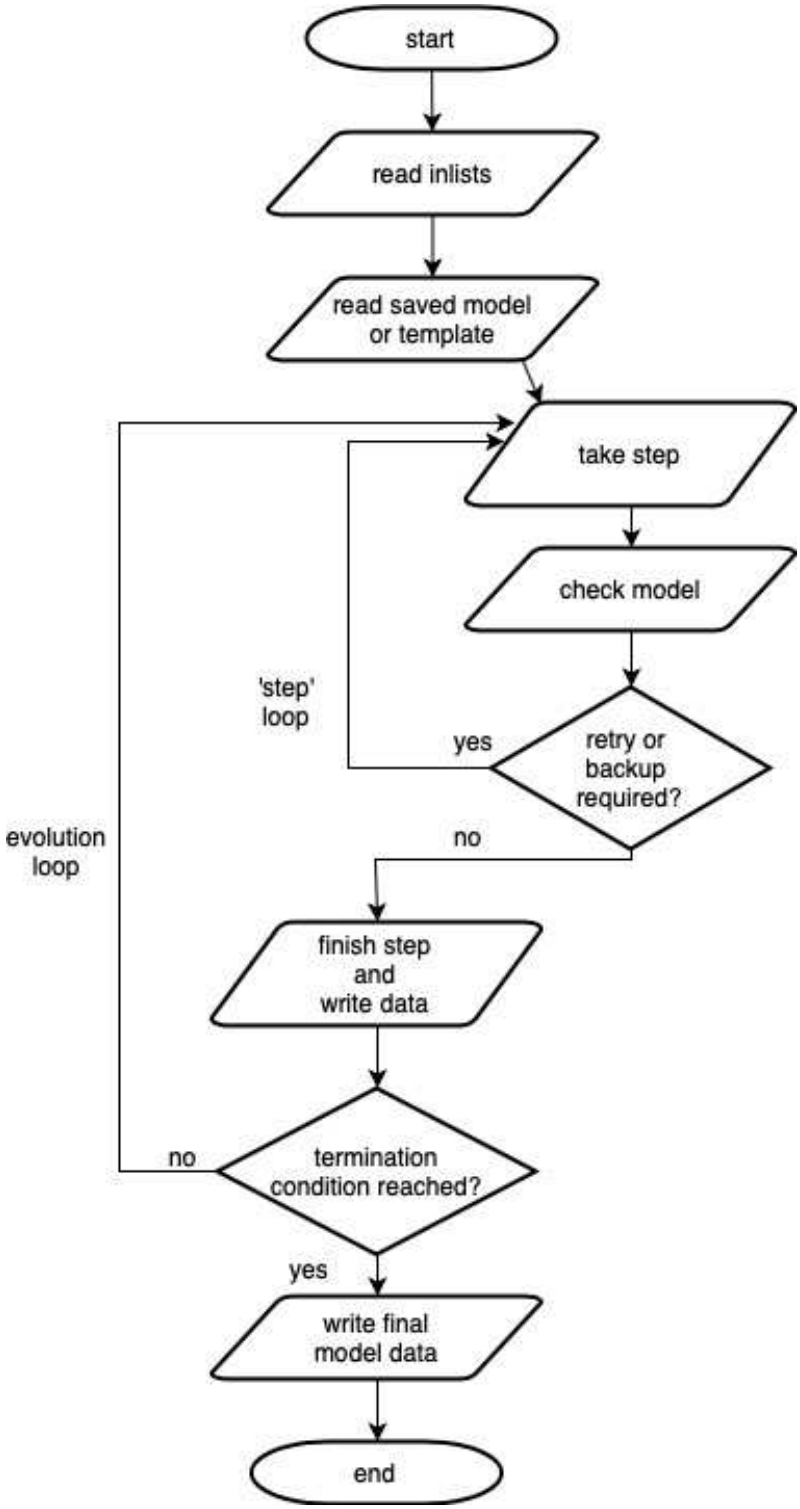

Figure 2.1: Flowchart showing a simplified representation of how MESA carries out a stellar evolution calculation.

to the stellar structure equations, residuals will remain between the values of the 'basic variables' (P, T, ρ, etc.) of the trial solution and a solution which satisfies the stellar structure equations. From these residuals, a correction to the variables in each cell is computed using the Newton-Raphson method and the process is iterated until the magnitude of both the residuals and the corrections is very small or in an idealised situation, where the residuals are 0, (Equation 2.1).

$$0 = \vec{F}(\vec{y}) = \vec{F}(\vec{y_i} + \delta\vec{y_i}) = \vec{F}(\vec{y_i}) + \left[\frac{d\vec{F}}{d\vec{y}}\right]_i \delta\vec{y_i} + O(\delta\vec{y_i}^2) \tag{2.1}$$

Here $\vec{F}$ is the residuals, y is the trial solution, i represents the iteration number, δy is the correction to the trial solution and $\left[\frac{d\vec{F}}{d\vec{y}}\right]_i$ is the Jacobian matrix, containing the partial derivatives with respect to the basic variables. Simplifying the above equation, and writing the Jacobian matrix as $\vec{H}$, one can see that the corrections to the trial solution can be obtained as follows (Equation 2.2).

$$\begin{aligned} 0 &= \vec{F}(\vec{y_i}) + \vec{H_i}\delta\vec{y_i} \\ \delta\vec{y_i} &= -(\vec{H_i})^{-1} \bullet \vec{F}(\vec{y_i}) \end{aligned} \tag{2.2}$$

Once the values of the correction and the residuals are below the specified tolerances, MESA will accept the model has 'converged'. Due to the use of analytic Jacobian matrices (a Jacobian where the partial derivatives have all been directly evaluated by the code), this approach is generally very quick to converge. If the new structure does not converge within a small number of iterations, the code will try again with a smaller time step (retry), and if this continues to fail, it will return to the structure from the previous step and repeat this with a smaller time step (backup).

Thirdly, the size of the next time step is estimated. This will be informed by the rate of convergence of the current step. Finally, output files for this evolutionary step are generated. A more detailed description of these methods can be found in section 6 of Paxton *et al.* (2011) and appendix B of Paxton *et al.* (2013).

While this method is very good at providing a numerically stable solution very rapidly, it is very important to verify that the results are physically reasonable.

Care should be taken to ensure that the resolution of the model is sufficiently high in both the spatial and temporal dimension, otherwise the model my diverge from true physical behaviour, despite converging to a mathematically valid result. Such errors are likely to occur in situations where conditions are changing very rapidly in time or in a very localised region of the model. MESA anticipates these issues by using strict constraints on how much properties of an individual cell in the model can change in one step to limit the size of the time steps and will increase the resolution of the grid if it finds a region in the model where the properties are changing rapidly, so as to adequately resolve steep gradients. One evolutionary stage where this is of critical importance in this work is the ignition of helium and hydrogen shell flashes, where there are sudden increases in luminosity in the star. Strict time step controls were employed in the stellar models in this work in order to progress through these flashes in an accurate manner.

2.1.2.2 Data Output

There are two main forms of output file; 'history' files and 'profile' files. A history file records information about the global properties of the model (mass, luminosity, radius, age, etc.) and stores the value at regular increments, allowing the user to produce evolutionary diagrams such as a HR diagram (an example of which will be seen in Figure 3.2). A profile file provides a complete description of the structure (pressure, density, composition, etc.) of the star at a specific point in its evolution. These profiles are useful for interpreting the structure of a star at a fixed point in time and identifying what processes are significant for its structure. An example of this can be seen in Figure 4.5, where the opacity and composition of some models as a function of interior temperature are plotted. In both the history and profile files, the choice of parameters listed and the frequency at which data is written can be determined by the user. Other forms of output include the `pgstar` module, which can produce live plots of the evolution while the simulation is running and specially formatted pulsation data output which is directly compatible with the input to a number of stellar oscillation calculations.

2.1.2.3 Data Visualisation

A number of tools exist which process the tabulated MESA output data and convert it into a data structure for manipulation in a variety of programming languages. In this work, the `read_mesa` subroutine for IDL (Townsend, 2019) and the `mesareader` package[1] for Python were used. These tools, along with a number of other open-access tools for MESA are made available on the MESA community website[2].

2.2 Analysing Stellar Oscillations with GYRE

A stellar oscillation code calculates the eigenfrequency spectrum for any arbitrary stellar model provided to it, providing a useful tool for identifying the structure and driving mechanism of a pulsating star. The GYRE[3] oscillation code (Townsend & Teitler (2013); Townsend *et al.* (2018)) was used for this project due to its robust and efficient nature and the fact that it is fully integrated with the MESA package. Output files from MESA can be provided directly to GYRE for analysis.

2.2.1 Numerical Methods

GYRE begins by reading an input model, and placing it onto a spatial grid, which in the first instance is the same as that of the stellar evolution model. The user can decide to increase the resolution in certain intervals to better resolve boundaries which may be important for determining the eigenfrequencies. Then GYRE solves the equations of adiabatic stellar oscillations, a set of linear, homogeneous ordinary differential equations, similar to the adiabatic wave equation mentioned above. It achieves this by placing the system of equations into a matrix form

$$\mathbf{S}\mathbf{u} = \mathbf{0} \tag{2.3}$$

where $\mathbf{S}$ is the system matrix containing the differential equations and the boundary conditions, and $\mathbf{u}$ is a vector containing the dependent variables at each grid

[1] `https://github.com/wmwolf/py_mesa_reader`
[2] `http://cococubed.asu.edu/mesa_market/add-ons.html`
[3] Latest version available at `https://bitbucket.org/rhdtownsend/gyre/wiki/Home`

point. The dependent variables chosen for use in GYRE are identified in the Appendix of Townsend & Teitler (2013). The pulsation equations are then solved using a method referred to as the Magnus Multiple Shooting scheme Magnus (1954) as described in Section 3 of Townsend & Teitler (2013). By constructing the system in this way, the non-trivial solutions to the equations are found when the determinant of $\mathbf{S}$ is zero. As $\mathbf{S}$ depends on the value of ω, evaluating the determinant of $\mathbf{S}$ along a grid of frequency points can identify the roots of the function. If the determinant changes sign between two frequency points, then a root exists between them and a root-finding scheme is employed to accurately determine the eigenfrequency. Finally, the eigenfunctions are normalised and GYRE writes its output. The procedure for calculating the non-adiabatic eigenfrequency spectrum is similar to the adiabatic case outlined here, except the oscillation equations have been modified to account for the non-adiabatic effects. GYRE then uses the results of its adiabatic analysis as starting values for its non-adiabatic frequency search. This method may have difficulties in regimes where the star is in a highly non-adiabatic state. In such scenarios, the imaginary component of the eigenfrequency may be comparable in size to the real component. Therefore using the adiabatic eigenfrequency as an initial trial frequency may not be sufficiently close to converge to a solution. Situations where this can occur is in stars with a very high luminosity-to-mass ratio or with extremely large opacity bumps. Such a situation is encountered in Chapter 5.

2.2.2 Running GYRE and Analysing the Results

GYRE functions in a similar way to MESA. The input files provide GYRE with a stellar model and specify the mode orders, frequency ranges and numerical tools with which to carry out the calculation and the results are returned in summary files which list the frequencies and other overall properties of each of the identified modes, and individual files for each mode containing information such as the derivative of the work function and the displacement as a function of radius. The choice of parameters to be stored in the files can be specified by the user in the input file. Data from these output files has been used in Chapters 4 and 5, such as in Figure 4.5, where the value of $\frac{dW}{dx}$ for the radial fundamental

mode as a function of stellar temperature is plotted providing a diagnosis of where the driving region in the star is located.

2.3 Summary

MESA and GYRE provide powerful tools for understanding the structure and evolution of stars. They were chosen for this research due to their open-source nature, helpful community of developers and users and the close integration of the two codes which allows for efficient calculations.

3

Atomic diffusion in subdwarf progenitors

The work in this chapter has been published as Byrne *et al.* (2018), co-authored with C. Tout and H.Hu, whose discussions provided the inspiration for the project. The co-authors provided some feedback during the writing of the manuscript.

3.1 Introduction

The abundances of chemical elements on the surface of a star depend on many different physical processes. These include mass transfer in a binary star system, accretion from a circumstellar disc, mixing of nucleosynthesised material from the interior to the surface, magnetic fields and atomic diffusion. If a star shows large deviations in abundances of certain elements from a standard or average star of its type, it may be classed as a chemically peculiar star.

Atomic diffusion is a term used to describe a group of particle transport processes which act to modify the chemical structure of a star, provided the material is hydrodynamically stable. These processes are thermal diffusion, concentration diffusion, gravitational settling and radiative levitation.

3. ATOMIC DIFFUSION IN SUBDWARF PROGENITORS

In most stellar atmospheres, one element (either H or He) typically dominates and the effects of concentration diffusion can be neglected. If a star has a steep pressure gradient, this dominates over thermal diffusion, so reducing the diffusion problem to a balance between the inward force of gravity and the outward force of radiation. The different forces acting on different elements lead to changes in the composition of the atmosphere and has been shown to explain different types of chemically peculiar stars, such as the Ap stars (Michaud, 1970).

One particular group of stars which show many anomalous surface abundances are the hot subdwarf stars. These low-mass (about $0.5\,M_{\odot}$), helium core burning stars can vary massively in appearance from atmospheres almost entirely comprised of hydrogen to those which are extremely helium-rich. Some subdwarfs show extremely anomalous abundances of lead, zirconium and other heavy elements (Jeffery *et al.*, 2017; Naslim *et al.*, 2011). This diverse population of stars is thus an ideal environment in which to test the treatment of diffusion in stellar evolution simulations. Diffusion is necessary to explain some of the unusual properties of these stars, such as the presence of pulsations, caused by Z-bump opacity due to radiative levitation of iron (Charpinet *et al.*, 1997; Fontaine *et al.*, 2003) and nickel (Jeffery & Saio, 2006b).

Three main formation channels for hot subdwarfs have been identified (Han *et al.*, 2002, 2003). Hot subdwarfs may be formed by the merging of two low-mass white dwarfs, by stable mass transfer via Roche lobe overflow (RLOF) from a red giant to a low-mass binary companion or by unstable mass transfer between a red giant and a low-mass star which leads to the formation of a common envelope that is subsequently ejected. These three channels produce single hot subdwarfs, subdwarfs in long-period binary orbits and subdwarfs in short-period binary orbits respectively.

Computational modelling of double white dwarf mergers has shown that this can explain the formation of helium-rich hot subdwarfs (Zhang & Jeffery, 2012). However this evolution channel would produce single hot subdwarfs and not binaries. At least one helium-rich subdwarf is known to be in a spectroscopic binary with an orbital period of 2.3 d, which indicates a post-common-envelope rather than a merger origin (Naslim *et al.*, 2012). The common envelope ejection is a poorly understood phase of evolution, and the exact outcome of such events is

unclear. A recent review of common envelope evolution is given by Ivanova *et al.* (2013), while hot subdwarfs are discussed at length by Heber (2016).

What makes hot subdwarfs such an interesting area of research is the diversity of surface chemistries which exist in the same region of the HR diagram. Spectroscopic determinations of the surface helium abundances of these stars as a function of effective temperature reveal 2 distinct sequences of stars as seen in fig. 6 of Németh *et al.* (2012). The majority follow a trend of increasing helium abundance with increasing temperature. However, a small number of hot subdwarfs fit into a more helium-deficient sequence. The observations also illustrate that a majority of subdwarf B type stars (sdBs) are helium-deficient, with a small number being helium-rich. The concentration of many different types of stars into a small region of the HR diagram indicates that these populations may have had different evolutionary histories.

Studies of the evolution of post-common-envelope hot subdwarfs have been carried out by, for example, Xiong *et al.* (2017). However the effects of atomic diffusion have not always been considered. Clear understanding of the results of diffusion processes in these stars is needed in order to find the conditions in which the surfaces of hot subdwarfs become hydrogen-rich or helium-rich.

We carry out an investigation of both of these key elements of hot subdwarf physics (namely diffusion and evolution) in an attempt to quantify the effects of the history of these objects on their present state and attempt to link this to the different populations of observed hot subdwarf stars.

3.2 Methods

Version 7624 of the MESA stellar evolution code (Modules for Experiments in Stellar Astrophysics; Paxton *et al.* (2011, 2013, 2015)) was used to carry out this research. MESA was chosen because it is a robust code capable of approximating the evolution through helium flashes, a key step in the evolution of hot subdwarfs which populate the extreme horizontal branch (EHB) and in which helium core burning has started.

Input physics parameters were chosen to be similar to those in other works using MESA to study hot subdwarfs. A composition with a metallicity of $Z =$

Table 3.1: Key physics choices made for the models produced

Parameter	Value
Opacity	OP, Type I (Opacity Project Team, 1995, 1997)
$\alpha_{\rm MLT}$	1.9
Composition	Grevesse & Sauval (1998)
Mass loss	`relax_mass` (during CE ejection only)
Convection	Schwarzschild criterion
Diffusion	None (basic models)
	Thermal Diffusion (standard & complete)
	Concentration Diffusion (standard & complete)
	Gravitational Settling (standard & complete)
	Radiative Levitation (complete models only)

0.02 and $X = 0.7$ was used for the initial main sequence star, in line with that used by other recent works (e.g. Schindler *et al.*, 2015; Xiong *et al.*, 2017). The composition mixture was taken as that of Grevesse & Sauval (1998). The Grevesse & Sauval (1998) composition was chosen over the more recent Asplund *et al.* (2005) composition as the former mixture is better reconciled with the results of helioseismology and provides a better converged solar calibration model in MESA, whereas using the latter makes it difficult to calibrate the observable properties of the Sun simultaneously (Stancliffe *et al.*, 2016).

Convection is determined in these models using the Schwarzschild criterion and the effects of semiconvection, convective overshooting and thermohaline mixing have not been considered in this work. A value of 1.9 for the mixing length parameter, $\alpha_{\rm MLT}$ was chosen based on the calibrations of the mixing length parameter in MESA by Stancliffe *et al.* (2016). Because the phase of evolution examined during this work was the transition from the red giant branch (RGB) to the extreme horizontal branch (EHB) at the onset of core helium burning, Type I opacity tables were used. These simulations were carried out under the assumption that the star is sufficiently stable in this transition phase to allow atomic diffusion to operate. These parameters are listed in Table 3.1.

3.2.1 Atomic Diffusion

Diffusion in MESA is based on the Burgers equations (Burgers, 1969), with the approach of Thoul *et al.* (1994) including the modifications of Hu *et al.* (2011) to include radiative levitation as an option. The normal flag for diffusion in MESA only considers thermal and concentration diffusion and gravitational settling, with the inclusion of radiative levitation being included with an additional flag.

Three separate sets of simulations were carried out. As listed in Table 3.1, these were, one in which no atomic diffusion was carried out (basic models), one in which MESA's standard atomic diffusion was included (standard models) and a third set of models which included both standard diffusion and radiative levitation (complete models). MESA includes gravitational settling and thermal diffusion and concentration diffusion as the standard processes with the `use_element_diffusion` flag, whereas radiative levitation is included as an extra option. The calculation of radiative forces on all of the ions at each mesh point is a computationally expensive task so only a small set of models was produced which included radiative levitation, to investigate the effect it has on the results compared with the standard diffusion experiment. In this work, the elements for which diffusion velocities were calculated are H, He, C, N, O, Ne, Mg, Ar, Cr, Fe and Ni. For the models with radiative levitation, this was only enabled after the onset of helium burning at the first helium flash. Doing so before this caused numerical issues when the model encountered the large convective region driven by the flash. The convection generated would wash away the effects of any diffusion that occurred prior to this in any case. Results for the basic models are presented in Section 3.3.2, with the results of the standard and complete simulations in Sections 3.3.3 and 3.3.4 respectively. Diffusion velocities are calculated throughout the entire star for standard diffusion. For the complete models, the standard diffusion component of the calculations (thermal diffusion, concentration diffusion and gravitational settling) is carried out throughout the entire star while diffusion velocities owing to radiative levitation are calculated only in the outer layers of the star with a temperature less than 10^7 K. Radiative levitation is only activated after the first helium flash to avoid numerical instabilities.

3.2.2 Generating Subdwarf Models

We adopt, as subdwarf progenitor models red giant models at various points close to the tip of the red giant branch, shortly before helium core ignition. These models were produced from a $1\,M_\odot$ main sequence (MS) star. No mass loss was included in this phase of evolution because there is little difference in core mass across the range of MS masses which produce degenerate helium ignition ($0.8 - 2.0\,M_\odot$) and the fully convective red giant envelope means that the exact mass of the star has little effect on the structure of the stellar envelope. The model was then evolved to the tip of the RGB. At this point, the subdwarf progenitor models were chosen. These models then serve as the starting points for the common envelope phase. The initial positions of subdwarf progenitor models on the red giant branch are shown in Fig. 3.1, with the tip of the RGB also indicated. The numbers on the plot indicate specific models at different distances from the RGB tip, with the position of the resulting models on the horizontal branch indicated in subsequent figures.

The common envelope ejection was approximated by invoking a high mass-loss rate in MESA (the `relax_mass` option which removes mass at a rate of about $10^{-3} M_\odot\,\mathrm{yr}^{-1}$) down to a specified envelope mass. In the case of this experiment, the residual envelope mass was $6 \times 10^{-3}\,M_\odot$. This choice of envelope mass was arbitrary, but represented a typical value for a hot subdwarf. Choosing a larger or smaller initial envelope mass for a fixed core mass will shift the zero-age horizontal branch model to cooler or hotter temperatures respectively. Following this rapid mass loss, evolution was followed up to the point of helium core ignition. The simulation was stopped once the central helium mass fraction drops below 0.925. At this point the models were deemed to have reached the zero-age extended horizontal branch.

3.3 Results

When the star leaves the RGB, hydrogen-shell burning continues, until the core of the star become hot enough and massive enough for helium to ignite. This generally happens slightly off-centre before undergoing a series of smaller flashes,

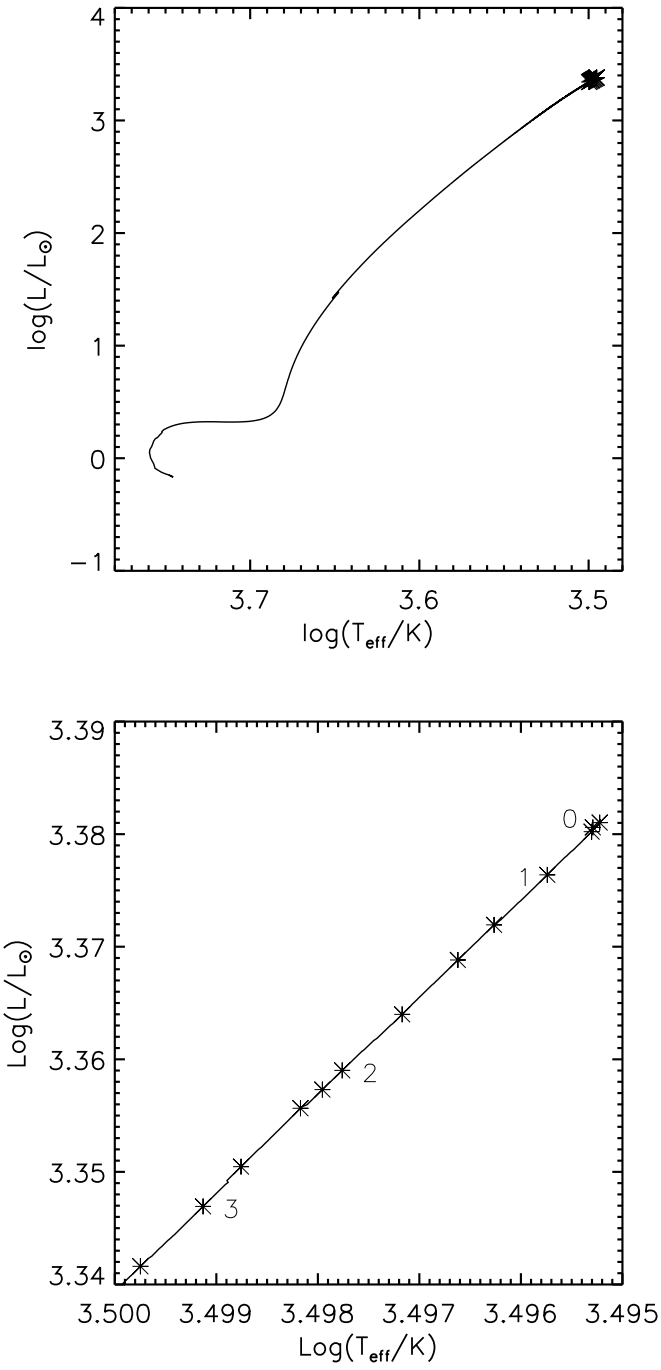

Figure 3.1: A Hertzsprung-Russell diagram illustrating the evolution of a $1\,M_{\odot}$ star along the RGB. The crosses illustrate the different starting points on the RGB at which common envelope ejection events were carried out, close to the RGB tip. The lower panel shows an expanded view of these points. Models labelled 0–3 are referred to in the text and subsequent figures.

until helium ignition reaches the centre of the star. This explains the 'loops' in the evolution tracks shown in Fig. 3.2. After helium ignition, the core expands and hydrogen-shell burning is quenched.

3.3.1 Evolution from the RGB to the ZAEHB

Three different evolution tracks are shown, representing the different stages at which the flash can occur. The numbers next to the tracks indicate which of the numbered progenitor models in Fig. 3.1 they are associated with. The solid line (model 3) shows a model that has a very late flash, owing to the fact that the envelope is removed when it still requires a significant amount of growth in core mass, and has reached the white dwarf cooling track before the core contracts and heats enough to ignite. The dashed line (model 1) is the evolution track of a model which underwent a CEE immediately before the point of the first helium flash. No additional burning is needed to reach the threshold mass and the envelope left behind after the ejection is mostly unaltered by the ignition of helium, meaning it arrives on the cooler end of the EHB. The dotted track (model 2) is a model which is intermediate between these two extremes. These evolution tracks are similar to those in the literature (Brown *et al.*, 2001, panels c, d and e of their fig. 4).These are referred to as early, intermediate and late hot flashers, based on how soon after leaving the red giant branch that the first helium flash occurs. The formation of He-rich stars from very late helium flashes is also in agreement with the results of Miller Bertolami *et al.* (2008). The model with the largest core mass (model 0) represents an RGB star at the point of first helium flash. Using sudden mass loss to replicate a common envelope ejection at this point leads to an unphysical result whereby mass loss continues while the star contracts significantly. Thus results for this model have been excluded from subsequent plots.

The effects of these flashes can be seen in Fig. 3.3, where the time evolution of hydrogen and helium luminosity are plotted, along with surface helium mass fraction. In this instance, and all further instances of reference to 'surface' abundances in the models in this Chapter refer to the average abundance in the outer 10^{-8} $M_{\odot}$ of the star. This measurement is not directly comparable to the surface

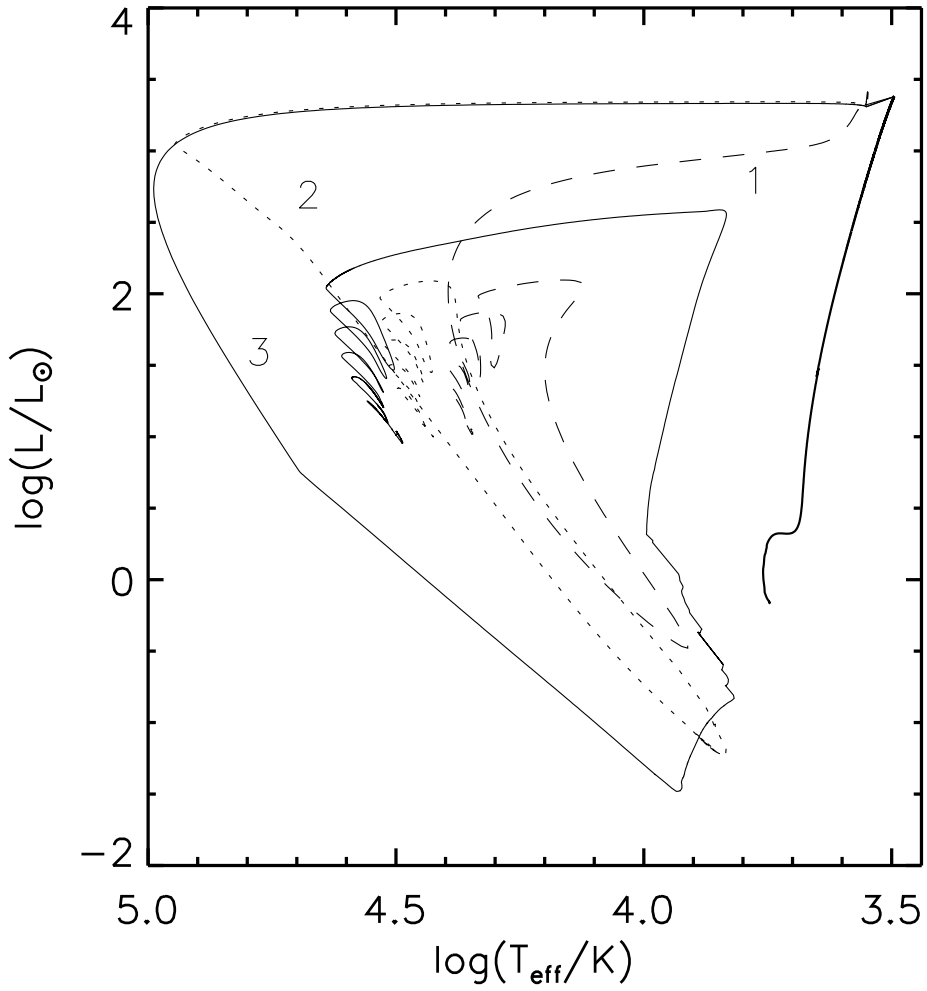

Figure 3.2: A Hertzsprung-Russell diagram illustrating the evolution of three different post-CEE models. The solid line (1) is that of a very late hot flasher which forms a hot, helium-rich hot subdwarf, the dashed line (3) is an early late hot flasher which forms a cooler, hydrogen rich hot subdwarf, and the dotted line (2) is a model which flashes at an intermediate time after the CEE and forms a hydrogen-rich, intermediate temperature hot subdwarf.

abundances from observations, which relate to measurement of the abundances of the atmosphere, which comprises a much smaller portion of the star. Therefore caution must be exercised when comparing 'surface' abundances from these simulations to observed abundance trends.. This reveals that model 3, which underwent the common-envelope ejection with a smaller core mass, takes more time to ignite helium. However when it does, it also has a large hydrogen shell flash which burns some of the residual hydrogen envelope and also drives a significant amount of convective mixing which further depletes the surface of hydrogen, and results in the formation of helium-rich models. Another notable result that can be seen in Fig. 3.3 is that, at the point of reaching the zero-age horizontal branch, the surface helium abundance of models which include diffusion is still in a decline and is yet to reach an equilibrium value. Therefore the expected values of the surface helium mass fraction, $\log(Y)$, for hot subdwarfs which are more evolved will be lower than the abundances found in these simulations. Further analysis of an individual example is carried out in Section 3.3.5.

3.3.2 Basic Models

A total of 34 models were produced to populate the EHB, using three different sets of diffusion physics. The ZAEHB positions of the models are shown in a surface gravity - effective temperature diagram in Fig. 3.4. Diffusion makes very little difference to the ZAEHB positions, as they all populate the same linear region of the gravity-temperature domain.

Table 3.2 shows the key properties of the progenitor and subdwarf models for all 3 sets of input physics, including core mass at departure from the RGB, M_{Core}, total subdwarf mass, M_{sdB}, subdwarf envelope mass, M_{Env} and surface helium mass fraction, $\log(Y)$, for zero-age horizontal branch models for the different diffusion options. The mass contained between the surface and the point in the star where the hydrogen mass fraction drops below 0.01 gives the value of M_{Env}. $\log(Y)$ and all subsequent elemental mass fractions refer to the average abundance of the outer 10^{-8} of the total stellar mass. As mentioned above, this 'surface' mass fraction is not directly comparable to measurements from spectroscopic observations.. The final envelope mass reported in Table 3.2 differs from the

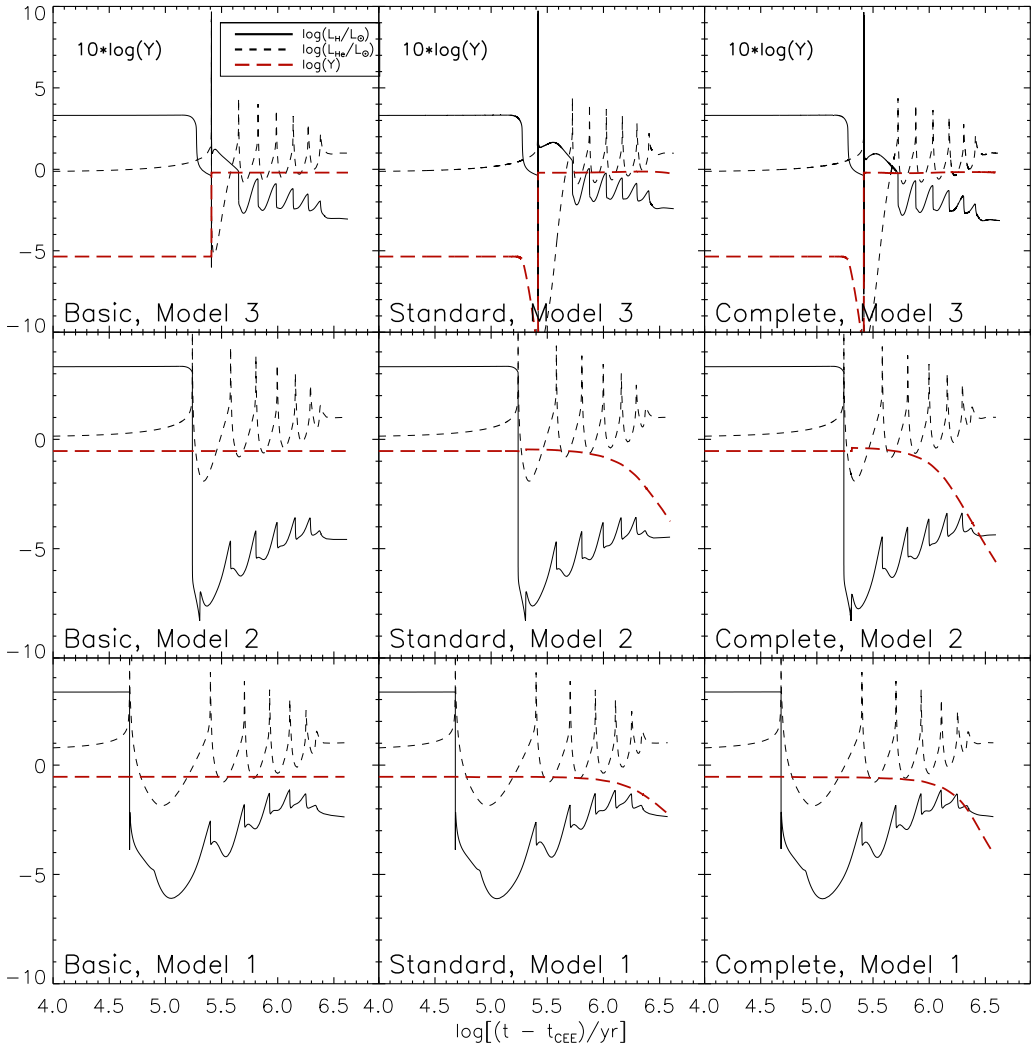

Figure 3.3: Time evolution of hydrogen luminosity, helium luminosity (both in solar units) and surface helium mass fraction from common envelope ejection up to the point of helium core ignition on the zero-age horizontal branch. The model numbers refer to the representative models indicated in previous figures. The terms basic, standard and complete refers to models with no diffusion, models with diffusion and models with diffusion and radiative levitation respectively. For the top panels, $\log(Y)$ has been multiplied by 10 for clarity.

Table 3.2: Summary of key properties of the subdwarf models produced and the core mass of their corresponding progenitor. The numbered models referred to in figures and the text are also indicated.

			Basic (No Diffusion)		Standard Diffusion		Complete Diffusion	
N_{model}	$M_{Core}/M_\odot$	$M_{sdB}/M_\odot$	$M_{Env}/M_\odot$	$\log(Y)$	$M_{Env}/M_\odot$	$\log(Y)$	$M_{Env}/M_\odot$	$\log(Y)$
–	0.4550	0.4610	–	-0.0204	9.366×10^{-9}	-0.0172	–	–
3	0.4561	0.4621	–	-0.0203	1.488×10^{-8}	-0.0291	1.156×10^{-9}	-0.0231
–	0.4569	0.4629	–	-0.0218	1.620×10^{-8}	-0.0336	–	–
–	0.4581	0.4641	–	-0.0220	2.633×10^{-6}	-1.8928	–	–
–	0.4585	0.4645	4.607×10^{-3}	-0.0717	5.161×10^{-3}	-4.8077	–	–
2	0.4588	0.4648	2.254×10^{-3}	-0.5356	2.286×10^{-3}	-3.7528	2.392×10^{-3}	-5.6146
–	0.4600	0.4660	1.605×10^{-3}	-0.5356	1.853×10^{-3}	-3.0379	–	–
–	0.4611	0.4671	2.676×10^{-3}	-0.5356	3.052×10^{-3}	-2.6275	–	–
–	0.4619	0.4679	3.374×10^{-3}	-0.5356	3.838×10^{-3}	-2.4416	–	–
1	0.4630	0.4690	4.450×10^{-3}	-0.5356	5.021×10^{-3}	-2.2191	5.006×10^{-3}	-4.0330
–	0.4637	0.4698	5.147×10^{-3}	-0.5356	5.805×10^{-3}	-2.0921	–	–
–	0.4641	0.4701	5.498×10^{-3}	-0.5356	6.144×10^{-3}	-2.0489	–	–
–	0.4645	0.4705	5.853×10^{-3}	-0.5356	6.540×10^{-3}	-1.9803	–	–
–	0.4646	0.4706	6.003×10^{-3}	-0.5356	6.687×10^{-3}	-1.9786	–	–
0	0.4647	0.4707	6.014×10^{-3}	-0.5356	6.790×10^{-3}	-2.3461	6.797×10^{-3}	-4.3458

initial envelope mass for a number of reasons. First, the core mass at envelope ejection is a key quantity. Models further from the tip of the giant branch need to grow larger cores before igniting helium and thus consume some of the remaining envelope before becoming a horizontal branch star. In the case of the very late flashers, the envelopes are so thin at the time of helium flash that the flash driven convection leads to the formation of a helium-rich star. Secondly, the choice of diffusion physics affects the reported envelope mass. This is due to the settling of helium in the models including diffusion, which shifts the position where the hydrogen mass fraction drops below 0.01 deeper into the star. Hence some of the models close to the tip of the red giant branch end up with zero-age horizontal branch envelope masses slightly larger than their initial values.

These models have a spread of effective temperatures in the range of $22\,000 - 32\,000\,\mathrm{K}$ ($4.34 \leq \log T_{\mathrm{eff}}/\mathrm{K} \leq 4.51$), where the surface temperature is directly related to the mass of hydrogen envelope remaining. This variation in hydrogen envelope mass is partially due to the time taken for stars to ignite helium. The models which undergo a CEE event earlier on the RGB start with a smaller core, and spend time burning some of the remaining envelope hydrogen into helium to achieve a large enough core for helium burning to begin.

Surface helium abundances were calculated for the zero-age horizontal branch models and were plotted as a function of the effective temperature. The results of this can be seen in Fig. 3.5, with the basic models being indicated by the crosses (+). The solar helium mass fraction is indicated by the dashed line, while the dotted line represents typical sdB mass fractions found by Geier (2013). These typical observational abundances are presented here as a linear interpolation between the average abundances of 'cool' and 'warm' sdBs as in Table 2 of Jeffery *et al.* (2017).

This behaviour is quite similar to that seen in other theoretical models of hot subdwarfs produced with MESA where the hottest models tend to form helium-rich subdwarfs due to convective mixing of the remaining low-mass envelope, as seen in fig. 9 of Xiong *et al.* (2017), for example. The distribution of abundances and temperatures is far from a good match to observations. This will be discussed in more detail in section 3.4.3.

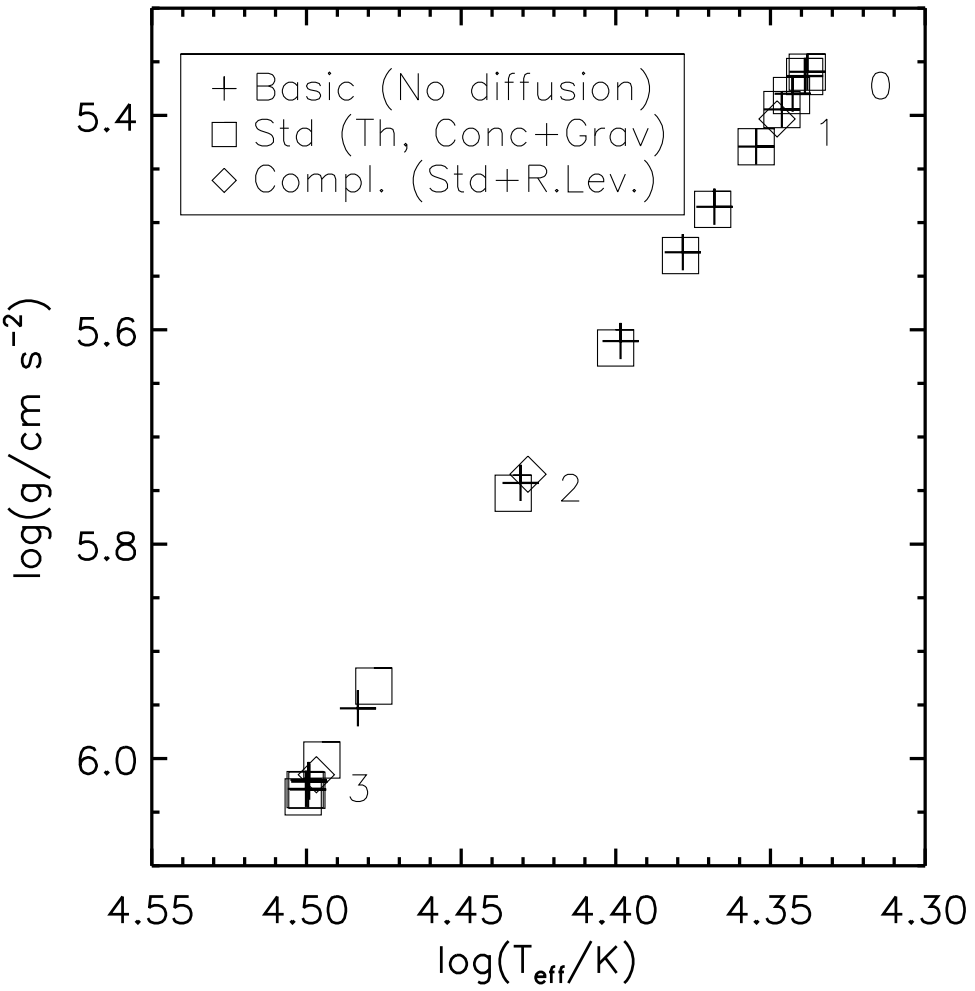

Figure 3.4: A surface gravity - effective temperature diagram illustrating the zero-age horizontal branch positions of the post-common envelope models. The three sets of models (basic, standard and complete) are indicated by crosses (+), squares (□), and diamonds (◊) respectively. The labels 0-3 indicate the approximate positions of the models referred to in the text and in Table 3.2.

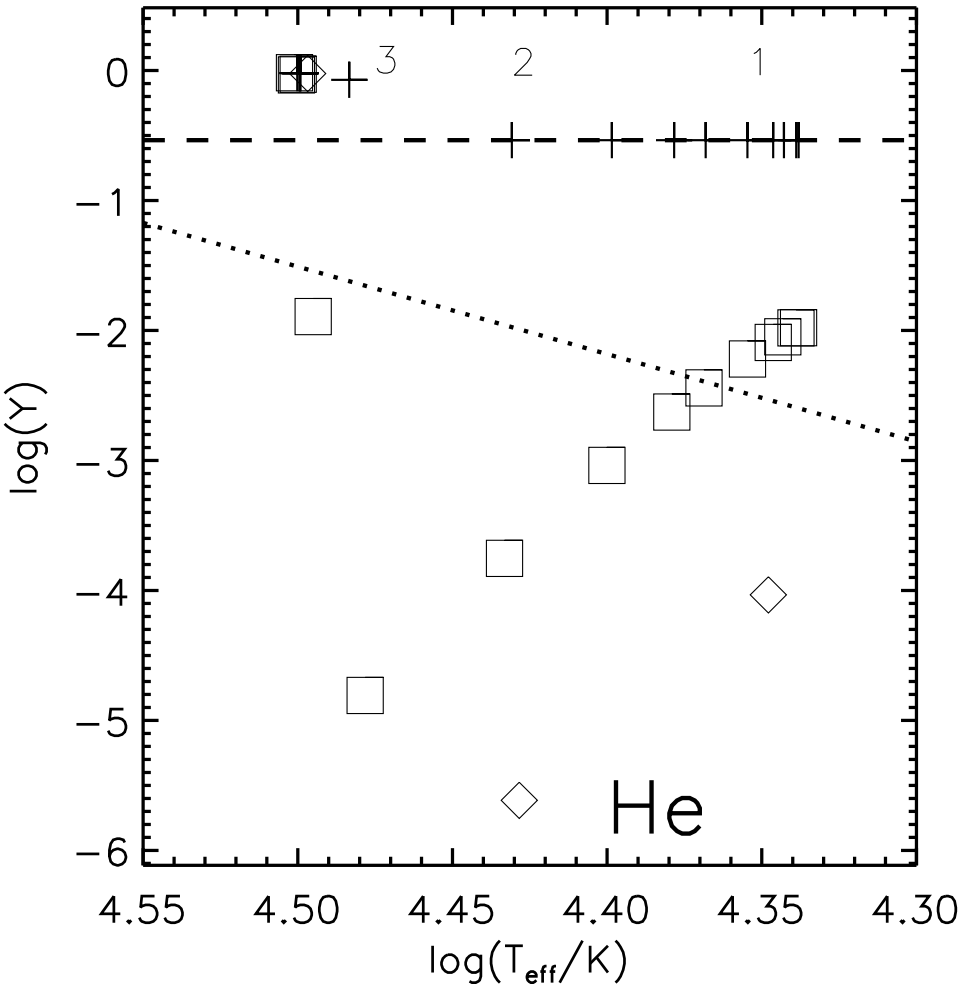

Figure 3.5: Zero-age horizontal branch surface helium abundances (mass fraction) as a function of effective temperature. The symbols have the same meaning as in Fig. 3.4. The numerals indicate the basic models corresponding to the representative progenitor models also numbered in Fig. 3.2. The dashed and dotted lines indicate solar values and observational values for hot subdwarfs from the work of Geier (2013) respectively. The observational values are based on an interpolation between average 'cool' and 'warm' sdB abundances as in Table 2 of Jeffery *et al.* (2017).

3.3.3 Standard Diffusion Models

To investigate the effects of atomic diffusion (with the exception of radiative levitation) on the evolution of these stars, a second set of models was produced via identical methods, with diffusion included. The luminosity and effective temperatures of the models were mostly unchanged, as shown in Fig. 3.4.

The effects of diffusion are much more noticeable in the surface helium mass fractions. These models show a significant depletion of helium in the envelopes of the hydrogen-rich subdwarfs, which increases with effective temperature. This is a consequence of the surface gravity being higher in the hotter stars. As soon as the hydrogen envelope has become thin enough for it to be mixed during the helium shell flashes, the decline in helium abundance is reversed and the models develop helium-dominated atmospheres. From this it can be inferred that, in order to form a hydrogen-rich hot subdwarf on the zero-age horizontal branch, a red giant must be quite close to undergoing a helium flash at the time of common-envelope ejection. However, helium-deficient subdwarfs are known to exist at temperatures higher than these models predict, so the choice of input physics in these simulations may not accurately represent the aftermath of a common-envelope event. For example, as suggested by Fig. 3.3, and expanded upon in Section 3.3.5 the surface helium abundance generally declines over the horizontal branch lifetime owing to diffusion, therefore such stars are likely more evolved stars. Additionally, over the horizontal branch lifetime, hot subdwarfs move to hotter temperatures and higher luminosities.

3.3.4 Complete Diffusion Models

Radiative levitation has been known to play an important role in hot subdwarf physics. Levitation of iron has been shown to cause an opacity bump large enough to produce the pulsations observed in many subdwarfs (Charpinet *et al.*, 1997). Later studies showed that nickel opacity also played a key role in the driving of these pulsations (Jeffery & Saio, 2007). Due to the computational effort required to determine radiative forces on all ions at all depths within the model stars, a smaller set of models (4 in total) was produced in order to determine the change in results expected from the inclusion of all aspects of atomic diffusion at different

positions along the EHB. The diamonds in Fig. 3.5 show that radiative levitation leads to further depletion of helium from the atmosphere in the pre-horizontal branch phase, for the cooler, hydrogen rich models, while the helium abundance of the helium-rich model is comparable to that of the standard diffusion model. Experiments with diffusion only being calculated for H and He show a similar difference between the models with and without radiative levitation, regardless of the inclusion of other elements in the calculations. Some modelling of the evolution on the extreme horizontal branch was carried out to investigate this further and is presented in Section 3.3.5. This can also be seen in the time evolution of $\log(Y)$ in Fig. 3.3, where the complete diffusion models show a more pronounced decline in surface helium than the corresponding standard models.

3.3.5 Beyond the Zero-Age Horizontal Branch

The presence of a difference between surface helium abundances in the zero-age horizontal branch models with and without radiative levitation is an interesting result. In order to investigate further, a selected model (model 1) was taken from the post-common envelope stage all the way to the end of the horizontal branch (determined as the point where central helium mass fraction reaches 0.1). Both the standard and complete diffusion options were simulated. The evolution of $\log(Y)$ is shown in the upper panel of Fig. 3.6. Here it can be seen that discrepancy continues for most of the horizontal branch lifetime, reaching an equilibrium at an insignificant level of helium towards the end of the horizontal branch. The vertical line illustrates the time at which the zero-age horizontal branch is reached, and illustrates the difference seen between the results shown in Fig. 3.5. The fact that both models show an insignificant amount of helium by the end of their lifetime suggests that mass loss and/or other processes must reduce the effectiveness of diffusion in order to match observed helium abundances.

The other issue which onward evolution can address is the fate of the helium-rich zero-age models present in these results. Using standard diffusion, model 3 was evolved along the horizontal branch. The evolution of $\log(Y)$ is shown in the bottom panel of Fig. 3.6. The helium enrichment of the surface due to the hydrogen shell flash is quite evident. The model remains helium rich at the

zero-age horizontal branch (again shown by a vertical line). Beyond the zero-age horizontal branch however, the remaining hydrogen begins to resurface and $\log(Y)$ decreases over the horizontal branch lifetime. This indicates that helium-rich and intermediate helium-rich subdwarfs are more likely to be young extreme horizontal branch stars or even pre-horizontal branch objects. These indications assume that diffusion acts the same throughout the 'surface' of the models, when in fact it is generally understood that gravitational settling will act much faster in the observable atmosphere as this will be the first part of the theoretical 'surface' (outer 10^{-8} $M_\odot$ of the star) to be depleted of helium as it sinks.

3.3.6 Differences Between Standard and Complete Diffusion Models

The behaviour of helium following the introduction of radiative levitation is interesting. Fig 3.7 illustrates the diffusion velocity of helium in model 1 as a function of temperature. In all cases, the outer layers of the model have a much larger negative diffusion velocity when radiative levitation is included. This larger velocity leads to a larger reduction in the surface helium abundance. Once the mass fraction of a particular element in a cell drops below 10^{-15}, a diffusion velocity is no longer calculated. Once the helium mass fraction of all the outermost cells drops below this diffusion of helium is no longer calculated, producing the flat line at lower-right in the top panel of Fig. 3.6. The other noticeable feature in Fig. 3.7 is the constant diffusion velocity for temperatures $\log T/\mathrm{K} < 5.2$ in the standard models. This results from the MESA input parameter choice for standard diffusion, which consequently treats a number of the outermost cells as a single entity to improve numerical stability. This approximation alone is not responsible for the velocity difference, because the radiative levitation velocities become substantially greater than the standard diffusion velocities at $5.2 < \log T/\mathrm{K} < 5.5$. Reduction of cell sizes in the standard diffusion calculation is not expected to lead to any significant difference in the results, and the difference between the surface abundance of helium in the standard and complete models would persist. This different behaviour highlights a number of issues which should be considered.

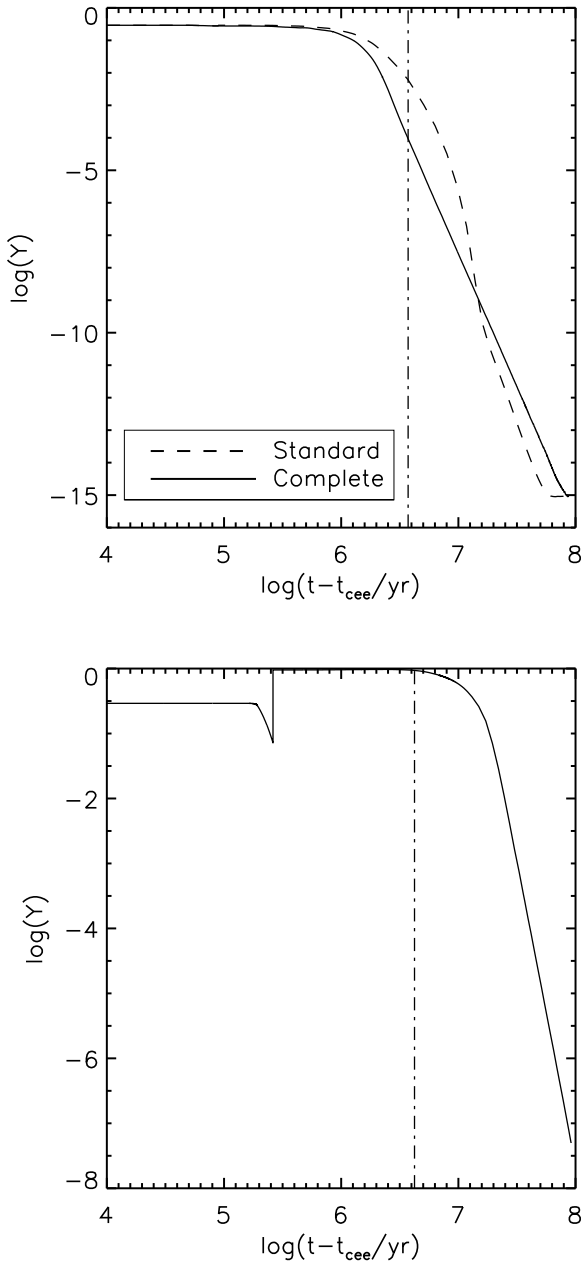

Figure 3.6: *Top:* Surface helium mass fraction as a function of time for Model 1 from post-common envelope phase right through to the end of core helium burning, with the dashed line representing a model with standard diffusion, while the complete diffusion model is shown by the solid line. The vertical dot-dashed line indicates the time at which the models reached the zero-age horizontal branch. *Bottom:* Surface helium mass fraction as a function of time for Model 3 with standard diffusion. The vertical dot-dashed line indicates the time at which the model reached the zero-age horizontal branch.

Opacity Project data only details monochromatic opacities (used for detailed radiative acceleration calculations) for 'metals' (C, N, O and beyond) and not for He. Therefore it is quite interesting that the inclusion of radiative acceleration calculations on helium leads to larger negative diffusion velocities in the envelope compared to when just gravitational settling is present. No additional monochromatic opacity data has been provided for helium, and therefore this does not exclude the possibility that there remain numerical issues in calculating helium diffusion velocities. Further testing of the implementation of these routines in MESA should be carried out in future, as the radiative levitation functionality has not been extensively tested outside of the work presented in this thesis.

3.4 Discussion

3.4.1 Comparison to Other Evolutionary Models

The set of basic models reproduce quite well the results of Xiong *et al.* (2017), both in terms of surface abundances and distribution on the HR diagram. The stars cooler than 28 000 K ($\log T_{\rm eff} = 4.45$) retain the chemical composition of the envelope that they had while on the RGB and immediately after the common envelope ejection. The stars hotter than 30 000 K ($\log T_{\rm eff} = 4.48$) all show significant helium enhancement, while a gap in temperature distribution is seen between the two groups of stars. This is a consequence of having envelopes sufficiently small. In this case, hydrogen gets depleted by the hydrogen shell flash and associated convective mixing of the core and envelope. Rather than a uniform decrease in envelope size, there is thus a point at which the hydrogen envelope is too thin to survive the flash-driven mixing and these models develop helium-rich atmospheres. This leads to a jump in the effective temperature distribution also, due to the sudden change in the mean atomic weight of the envelope.

The inclusion of diffusion makes a substantial difference to the surface composition of the models. Gravitational settling is more dominant in the hotter stars, which have a higher surface gravity, thus hydrogen becomes more dominant at higher temperatures. This trend gets reversed once the flash mixing is able to penetrate through the entire envelope. Helium becomes dominant from

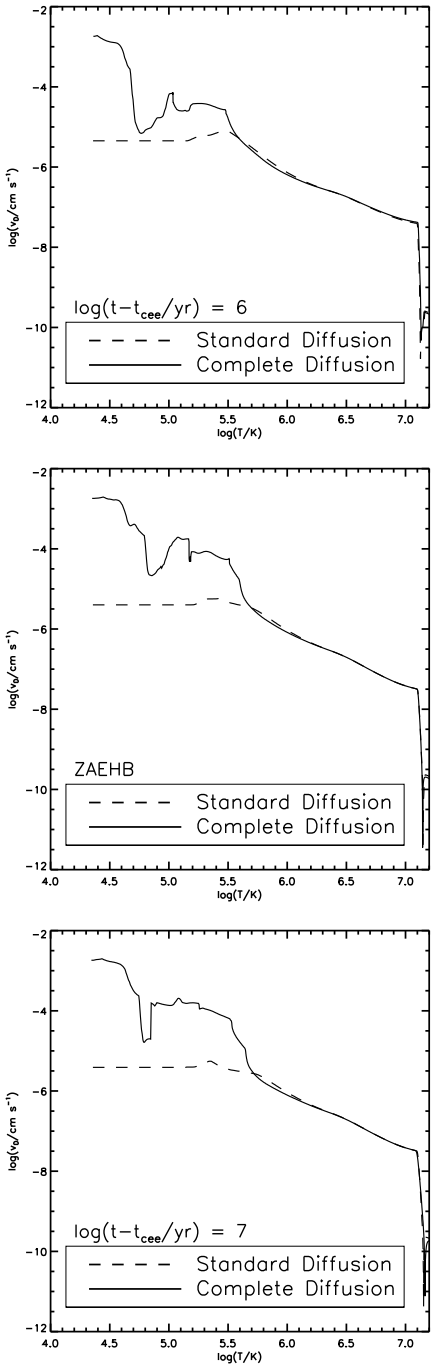

Figure 3.7: Diffusion velocity (v_D) of helium as a function of temperature in model 1 at 3 separate stages of evolution, 10^6 years after envelope ejection (top panel), at the zero age horizontal branch (approximately $10^{6.6}$ years after envelope ejection, middle panel) and 10^7 years after envelope ejection. The results for the standard and complete model are shown by the dashed and solid lines respectively. The value of v_D is negative up to temperatures of $10^{7.1}$ K where a sign inversion takes place.

this point onwards for the zero age models. Recovery of any remaining hydrogen to the surface is likely over the horizontal branch lifetime. The addition of radiative levitation further depletes the helium from the hydrogen-rich atmospheres. The helium-rich model (model 3) with radiative levitation has a similar helium abundance to that of the corresponding 'standard' diffusion model. This is in stark contrast to observations which show a general trend for the helium abundance to increase with increasing temperature.

3.4.2 Comparison to Other Diffusion Studies

This work also set out to investigate the effects of diffusion on the surface abundances of other elements. Studies into the effects of diffusion on hot subdwarf stars have been carried out before (Hu *et al.* (2011); Michaud *et al.* (2011) for example). However these studies used approximate methods for the helium flash in order to generate their subdwarf models. This study takes advantage of the fact that MESA is capable of evolving through the helium flash, albeit still with a certain amount of approximation. Using MESA, however, allows the effects of diffusion in the evolution from common envelope ejection through to core helium ignition to be examined in a more self-consistent manner. It is also worth noting that this study does still require the use of approximations for the common-envelope phase. By evolving through the helium flash, it was possible to investigate the effects of diffusion in the pre-horizontal branch phase of evolution. Under the assumption that the star is stable enough for atomic diffusion, it is found that diffusion plays a role in the surface properties of these stars before they reach the EHB, compared to earlier studies which start with a ZAEHB model for their diffusion studies.

Fig. 3.8 shows the surface abundances of the elements which were included in the diffusion calculations, plotted as a function of the ZAEHB temperatures of the models. The symbols have the same meaning as in the previous plots. The abundances are shown as mass fractions of the surface composition. With the basic models with no diffusion, most elements maintain their initial abundances across the entire set of models. The only exceptions to this are carbon, nitrogen and neon, which become enriched and oxygen which becomes depleted. This is a

direct consequence of the CNO and α processes at work during the hydrogen shell flash. In the standard models, the behaviour of the cool, hydrogen-rich models is comparable to that of helium, with all elements increasingly depleted with increasing surface gravity. In the flash-mixed models, the mass fractions show an increase. However, they remain below the initial values found in the models with no diffusion.

The behaviour of elemental surface abundances as a function of temperature upon the inclusion of radiative levitation is markedly different. Ar, Cr, Fe and Ni all show significant overabundances. This is expected, particularly for Fe and Ni, where the enhancement due to radiative levitation is known to explain the presence of pulsations in some hot subdwarfs (Charpinet *et al.*, 1997; Fontaine *et al.*, 2003; Jeffery & Saio, 2006b) and also reasonable given the complex atomic spectra of these elements. Radiative levitation seems to have no effect on Ne, with the data points lying in the same region of the plot as for standard diffusion. The behaviour of N and O is similar to He, while the depletion of Mg from the atmosphere is less significant, meaning it is partially supported by radiation pressure.

These results are in broad agreement with the findings of other studies. Michaud *et al.* (2011) shows the depletion of most light elements and the enhancement of elements heavier than argon, with the exception of iron. These results which include radiative levitation agree qualitatively with these findings, although a moderate enhancement to the iron abundance is also found. It is worth noting that these simulations do not use the turbulent mixing used by Michaud *et al.* (2011) to obtain their results. In the models of Hu *et al.* (2011) which include either mass loss or turbulent mixing, a slight enhancement of iron abundance is also seen, so a small enhancement of iron in the atmosphere is not an unusual result.

3.4.3 Comparison to Observations

The hottest subdwarfs produced by this method are the helium-rich models at about 32 000 K, which is slightly cooler than would be expected for subdwarf B stars, which have temperatures of up to 35 000 K or 40 000 K. However, this

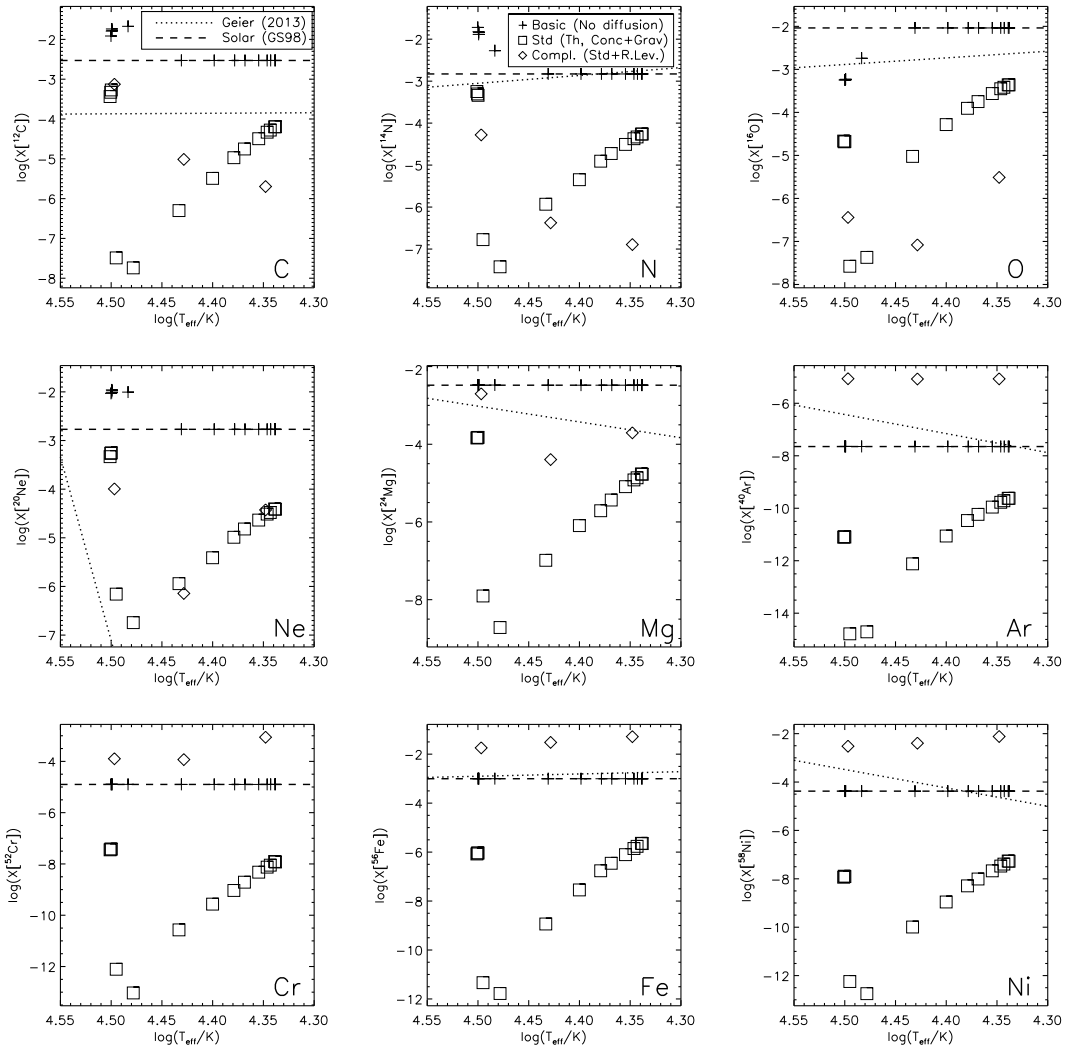

Figure 3.8: Zero-age horizontal branch surface abundances (mass fractions) as a function of temperature for the elements included in the models produced in this work. The symbols have the same meaning as in Fig. 3.4. The dashed and the dotted lines have the same meaning as in Fig. 3.5

issue is not unique to these models. Fig. 4 of Németh *et al.* (2012) includes the theoretical ZAEHB from the work of Dorman *et al.* (1993) in the surface gravity - effective temperature domain and the results agree extremely well with the ZAEHB produced in this work. There are a number of ways by which hotter subdwarfs could be produced, such as more massive stars, or allowing the stars to evolve away from the zero-age horizontal branch.

For models cooler than 28 000 K that are not flash mixed to the surface, models with diffusion give a surface helium abundance that is too low when compared to the observed data of Németh *et al.* (2012), while the models with no diffusion (like the models of Xiong *et al.* (2017)) give helium abundances which are too large for the vast majority of subdwarfs in this temperature range. Including mass loss and/or turbulent mixing in the outer layers of hot subdwarfs has been shown to improve the abundance mismatch between observations and models (Hu *et al.*, 2011). However, this comes at the expense of affecting the ability of the stars to pulsate and a physical explanation for the turbulent mixing remains unclear. The results presented here also imply that some other mechanism must reduce the effectiveness of the diffusion processes in order to produce subdwarfs with the observed surface helium abundances. The lack of observational evidence for a large population of helium-rich subdwarfs in short period binaries suggests that this evolutionary scenario is not favourable. However, resurfacing of hydrogen in some of the flash-mixed models reduces the number of helium-rich subdwarfs expected. Some close binaries containing helium-rich hot subdwarfs are known to exist. One such example is the helium-rich subdwarf CPD–20° 1123 (Naslim *et al.*, 2012), which is believed to be a post-common-envelope object, given its orbital period of 2.3 d. However, the surface temperature of this star has been measured at around 23 000 K ($\log \mathrm{T_{eff}/K} = 4.36$), much cooler than the temperatures at which the post-common envelope models presented here (either with or without diffusion) begin to develop super-solar helium abundances due to flash-driven convective mixing of the envelope. This disagreement between theory and observation suggests a problem in the assumptions made in the stellar evolution models. This could potentially be the treatment of diffusion physics or the method of simulating the common envelope ejection.

Another area of input physics which may be causing a discrepancy is the treatment of convection in 1-dimensional stellar evolution codes. Studies of convection in evolution models of subdwarf B stars have been carried out, and show that the size of convective cores in the models are considerably smaller than the convective core masses calculated from asteroseismic data (Schindler *et al.*, 2015). This implies that the Schwarzchild criterion, which is typically used to determine whether material is convective, may underestimate the true extent of convective mixing. The implications for the results presented here may be that even larger hydrogen envelopes could be fully mixed by a hydrogen shell flash, leading to a larger number of models which are helium-rich on the zero-age horizontal branch.

In terms of the abundances of other metals, the observational results of Edelmann *et al.* (2001) show depletion of C, N, O and Mg, super-solar Ar abundances and roughly solar Fe. For the complete models which include radiative levitation, the behaviour of these elements is in agreement with the observations, although the magnitude of the depletion is much higher than found observationally (2-3 dex below solar, rather than about 1 dex found in the observations). As discussed earlier, this is likely due to the need for an additional mixing process to oppose the action of radiative levitation. Other observational data for metal abundances in hot subdwarfs (Geier, 2013) show similar behaviour with light elements being depleted and heavier elements being enhanced. However, the magnitude of the changes are not as extreme as the results of the simulations which included radiative levitation.

3.4.4 Impact of Common Envelope Assumptions

The outcome of these simulations relies on a number of assumptions and approximations used to treat the common envelope phase. One way in which the results may be affected is the mass-loss rate used to replicate the envelope ejection. The mass loss rate of 10^{-3} $M_{\odot}\,yr^{-1}$ was chosen for this work. Using a lower mass-loss rate is physically unreasonable as the star will have time to respond to the changes, which would terminate mass transfer, rather than producing a common envelope. This would be better suited to probing the RLOF evolution channel. Choosing a higher mass loss rate will not significantly affect the outcome, but will

potentially lead to numerical difficulties as the model tries to adjust to having a significant portion of the outer layers being removed in each timestep.

Another area which could affect the results is the choice of residual envelope mass in the post-CE phase. The value of 3×10^{-3} $M_{\odot}$ was used in this work as it produced hot subdwarfs with a range of ZAEHB envelope masses, (between 0 and 6×10^{-3} $M_{\odot}$, as shown in Table 3.2) in reasonable agreement with other works. For example, Han *et al.* (2002) found that most observed subdwarfs lie on evolutionary tracks with envelope masses between 0 and 5×10^{-3} $M_{\odot}$. Choosing a smaller residual envelope mass would likely produce a larger number of helium-rich subdwarfs as there is less material to penetrated during helium ignition and thus more models might undergo a very late helium flash, becoming helium rich. Conversely, a larger remnant envelope mass would likely lead to fewer helium-rich subdwarf models. As seen in the simulations, models further from the tip of the RGB at the point of CEE will consume some of their remnant envelope before helium ignition. This means the model is functionally similar to a model which was slightly closer to the RGB tip with a smaller post-CEE envelope mass. This means that scenarios with a smaller assumed post-CEE envelope mass have been examined somewhat indirectly, although models with larger envelope masses can not. Future studies could investigate the evolution of models with more massive post-CEE envelopes.

3.5 Conclusions

Three sequences of post-common envelope stellar evolution models, one without diffusion and two with different diffusion physics, were created. These models had a self-consistent evolution from the red giant branch, through the helium flash to the onset of helium core burning at the zero-age horizontal branch.

The surface abundances of many elements were examined when the models reached the horizontal branch. The most significant result was the formation of helium-rich models at effective temperatures above 30 000 K. This was found to be due to a large hydrogen shell flash and significant convective mixing. This only happens when the model leaves the red giant branch due to common-envelope ejection, much earlier than the tip of the giant branch. In these cases, much of

the remnant of the envelope is burnt before the core grows massive enough to ignite helium, when it has already reached the white dwarf cooling track. This was found to be the case regardless of the diffusion physics used. However, the abundances of other elements were highly dependent on which diffusion processes were included. This helium-rich phase will not necessarily last for the entirety of the horizontal branch lifetime, as any remaining hydrogen in the envelope will diffuse towards the surface.

For the basic models with no diffusion, all elements remained at their initial abundances, apart from the flash-mixed, helium-rich models where carbon, nitrogen and neon were enhanced and oxygen was depleted due to the enrichment of the surface by CNO processed material from the hydrogen shell flash. With diffusion included, all elements are depleted in the hydrogen-rich models, with abundances increased in the flash-mixed models, but less than their initial abundances without diffusion, assuming the star is stable enough for diffusion during this phase of evolution. When radiative levitation is also included, elements lighter than neon become depleted even more than in the standard diffusion scenario, while elements heavier than magnesium are enhanced.

The results suggest that a population of helium-rich subdwarfs in short period binaries should be seen with temperatures of $30\,000 - 32\,000\,\mathrm{K}$, produced after common envelope events. However very few such systems are known to exist. This indicates that in order to produce hydrogen-rich subdwarfs at these temperatures, common envelope ejection must happen very close to the tip of the red giant branch, or a mechanism must exist for material ejected in the common envelope event to be accreted back on to the surface of the star. Another consideration is that in general, the observed stars will have evolved away from the zero-age horizontal branch to a varying degree. This will allow any remaining hydrogen to re-surface. The time evolution of the surface helium abundance shows it is still in decline at the zero-age horizontal branch and is yet to reach an equilibrium. Further study of the evolution beyond the zero-age horizontal branch could provide insight into the origins of intermediate helium-rich subdwarfs.

On the other hand, the cooler, hydrogen-rich models have practically no helium which implies that some form of turbulence or additional mixing must be present in order to reduce the effectiveness of diffusion. The results of Schindler

et al. (2015), which suggests that convection is presently underestimated in 1-D evolution models may be an additional source of mixing to counteract levitation and provide a closer match to observations.

Comparisons of these results to the observations of the proposed post-common envelope hot subdwarf CPD–20° 1123 shows that helium-rich hot subdwarfs are only produced at temperatures greater than 28 000 K, which is too hot to explain such a system. Given that the effective temperature of CPD–20° 1123 is quite well determined, this suggests a flaw in the evolution models. The two key areas of input physics where there is uncertainty in the models is the treatment of convection and the treatment of the common envelope ejection itself.

4

The origin of blue large-amplitude pulsators

The work in this chapter has been published as Byrne & Jeffery (2018).

4.1 Introduction

Pulsational instability is a behaviour observed in stars all across the Hertzsprung-Russell diagram, from classical pulsators such as the Cepheid and Mira variables, to more recent discoveries such as the blue large-amplitude pulsators (BLAPs), variable stars found in the OGLE survey by Pietrukowicz *et al.* (2017). As previously detailed in Section 1.8.1, these objects have a high surface temperature and show pulsations of significant amplitude.

The surface gravity and effective temperature of OGLE-BLAP-001 place it below the main sequence, suggesting that a significant amount of mass may have been lost during its evolution Pietrukowicz *et al.* (2017). This is one of the similarities with extreme horizontal branch (EHB) stars, or hot subdwarf stars (Section 1.7). Proposed formation mechanisms for hot subdwarf stars include common envelope evolution by a red giant with a core of sufficient mass to begin fusing helium. A similar mechanism acting on a red giant with an inert $0.31\,\mathrm{M}_{\odot}$ core could produce an object with properties comparable to those observed for

BLAPs, according to envelope models of the pulsations computed by Pietrukowicz *et al.* (2017).

Most hot subdwarfs have a peculiar surface composition. Although most have helium-depleted surfaces, surface helium abundances can vary from almost 0 to 100 percent. A few show overabundances of elements such as lead and zirconium (Naslim *et al.*, 2011). Some hot subdwarfs show helium-rich surfaces comparable to that of OGLE-BLAP-001 with a helium mass fraction of 0.52. Like BLAPs, many hot subdwarfs are known to show brightness variations due to pulsations. As described in Section 1.7.3, some hot subdwarfs are known to oscillate in p-modes with periods of 2–9 minutes. These pulsations are driven by the κ-mechanism and it is found that atomic diffusion process known as radiative levitation is required. Radiative levitation has been explained in Section 1.5 and Chapter 3.

Chapter 3 investigated the effects of atomic diffusion and radiative levitation in particular on the evolution of a post-common envelope star as it evolves from the red giant branch (RGB) to the extreme horizontal branch (EHB) following the onset of helium burning in the core. Here we expand the analysis of these simulations to include searches for pulsations in pre-EHB models. We also investigate post-common envelope models of lower mass, to investigate the extent of any instability strip which may exist, as well as the driving mechanism behind it. The analysis focuses on specific models in the evolutionary sequence which have surface gravities and temperatures comparable to those of BLAPs in order to test the possibility that the direct progenitors of either hot subdwarfs or low mass white dwarfs could correspond to BLAPs.

4.2 Methods

Models of stellar evolution were computed using the computer program MESA (Paxton *et al.*, 2011, 2013, 2015, 2018, revision 7624). The methods adopted and parameter space explored closely follow those of Chapter 3 (henceforth referred to as Byrne *et al.*, 2018).

The evolutionary tracks of some of the pre-EHB models calculated by Byrne *et al.* (2018) pass close to the region of the luminosity – effective temperature di-

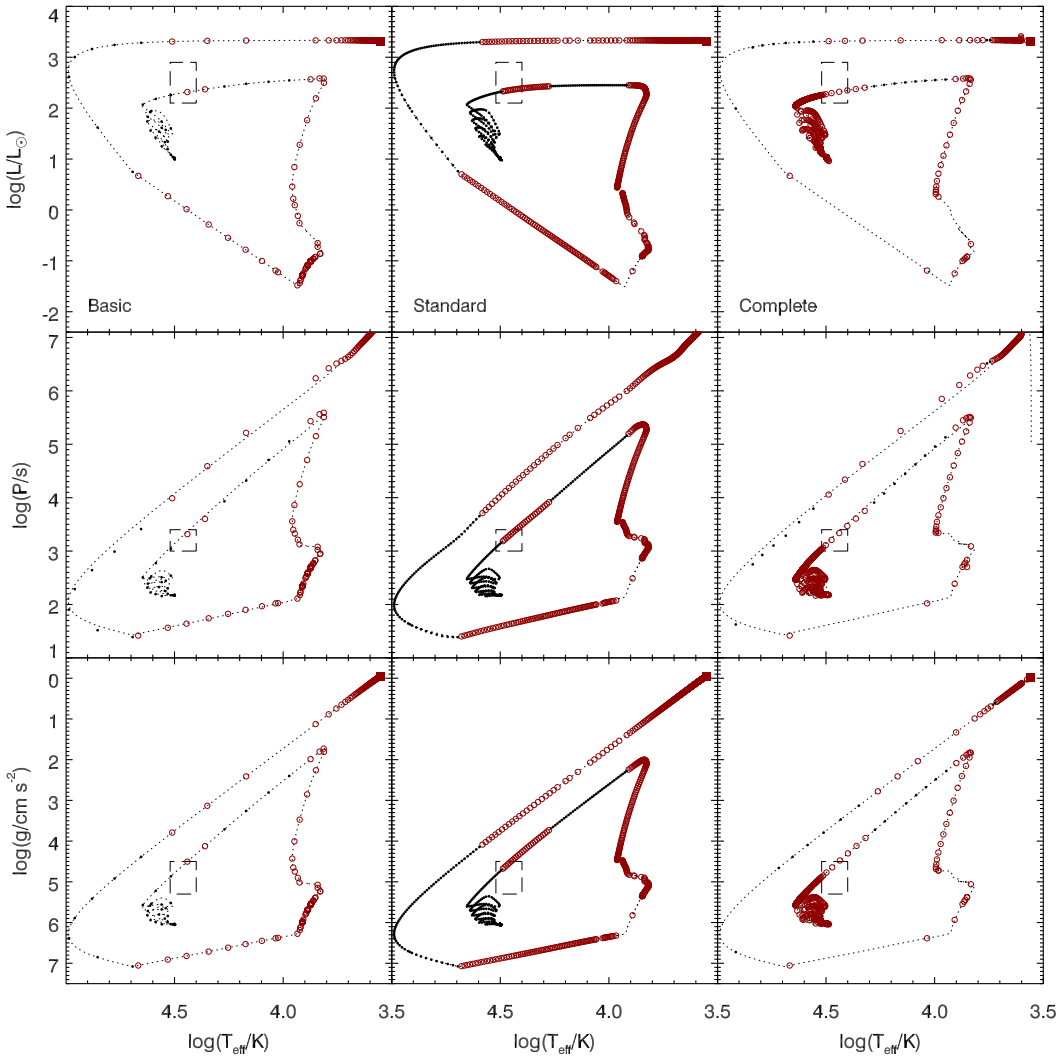

Figure 4.1: Evolution of luminosity (top row), fundamental period (middle row) and surface gravity (bottom row) as a function of effective temperature for the basic, standard and complete models of the 0.46 $M_\odot$ post-common-envelope models. Solid black dots indicate models found to be stable, while the open red circles indicate those with an unstable fundamental mode. The dashed rectangles indicate the approximate range of values of these parameters within which BLAPs have been found as reported by Pietrukowicz *et al.* (2017). Interpolation of a smoothly varying pulsation constant over the evolution means that not all points in the period-effective temperature diagram fall precisely on the evolution track fitted to the data.

agram where BLAPs have been identified. In this region, pre-EHB models match several of the observed properties of BLAPs, including inflated envelopes and helium-enriched surfaces. In this chapter, we consider in detail one model from Byrne *et al.* (2018), namely model 3, having an initial (zero-age main sequence) mass of 1 $M_\odot$, and a pre-EHB mass of 0.46 $M_\odot$ after simulated common-envelope ejection close to the tip of the RGB.

As described in Byrne *et al.* (2018), key model parameters include the mixing length $\alpha_{\rm MLT} = 1.9$, following Stancliffe *et al.* (2016), metallicity $Z = 0.02$ with the mixture of Grevesse & Sauval (1998), the Schwarzchild criterion for convection and a helium mass fraction $Y = 0.28$. More particularly, this model shows strong hydrogen-shell burning and flash-driven mixing which succeed in removing nearly all the surface hydrogen. The product is a helium main-sequence star, which might be identified spectroscopically as a helium-rich subdwarf O star (He-sdO).

Another possible structure for a BLAP, proposed by Pietrukowicz *et al.* (2017) and partially explored by Romero *et al.* (2018), is a star with a small helium core of about 0.31 $M_\odot$ that has been stripped of its envelope. For this work, a 0.31 $M_\odot$ post-common envelope star was produced using the same method as for the hot subdwarf stars in Byrne *et al.* (2018). That is, by implementing a large mass loss rate ($\dot{M} = 10^{-3}$ $M_\odot\,{\rm yr}^{-1}$) to strip most of the envelope, leaving only a small hydrogen envelope of $\sim 3\times10^{-3}$ $M_\odot$. This was allowed to evolve until it becomes a white dwarf with $\log L/L_\odot < -2$. The zero-age main sequence star had a mass of 1 $M_\odot$, $Y = 0.28$ and $Z = 0.02$.

Common envelope evolution remains a poorly understood phase of evolution. However, given that it is believed to happen on a dynamical timescale, the approach taken in this work is quite reasonable, as any detailed analysis of the structure is only done when the time since envelope ejection is longer than the thermal timescale of the star.

4.2.1 Diffusion and Radiative Levitation

The primary objective is to examine the effect of atomic diffusion, and radiative levitation in particular, on the chemical structure of the stellar envelope and the pulsation stability of the models as they pass through different phases of

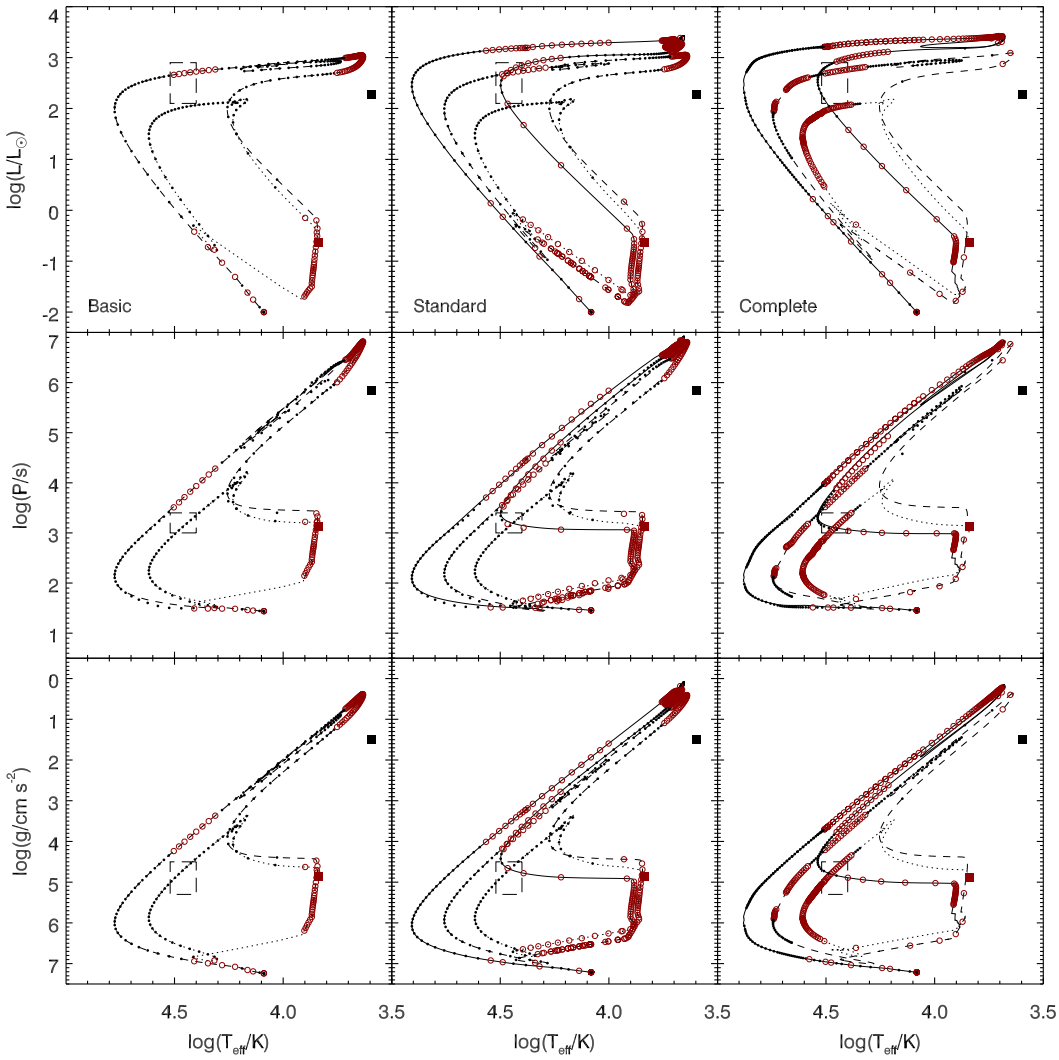

Figure 4.2: As Fig. 4.1, but for the 0.31 $M_\odot$ post-common-envelope models. The black squares indicate the location of the red giant model before envelope ejection, while the corresponding red squares indicate the first snapshot following envelope ejection. To assist with clarity, the first 'loop' in the diagram is indicated by a dotted line, while the second and third loops are represented by dashed and solid lines respectively.

evolution. MESA uses the approach of Thoul *et al.* (1994) to solve Burgers diffusion equations (Burgers, 1969). Modifications to this approach which are required in order to compute radiative levitation are described by Hu *et al.* (2011). This allows calculation of the radiative forces on all ions of specified elements for the chemical mixture in each of the outer layers of the star. In this study, radiative accelerations are calculated for all layers of the star with a temperature less than 10^7 K. In order to isolate the effects of radiative levitation and following Byrne *et al.* (2018), the evolution was calculated without diffusion (hereafter referred to as basic models), with thermal diffusion, concentration diffusion and gravitational settling (standard models), and with thermal diffusion, concentration diffusion, gravitational settling and radiative levitation (complete models).

4.2.2 Pulsation

To analyse the stability of the models, the oscillation code GYRE was used (Townsend & Teitler, 2013; Townsend *et al.*, 2018). Outputs from MESA can be configured as input to GYRE which allows for straightforward analysis of pulsation stability.

An adiabatic analysis was carried out to determine the eigenfrequencies of the model, followed by a non-adiabatic analysis to investigate the stability of the modes identified. As BLAPs are known to be large-amplitude pulsators, only radial modes ($\ell = 0$) were investigated in detail, although the excitation of other low-degree modes ($\ell \leq 2$) is possible. A brief discussion of higher mode orders is presented in Section 4.3.5. A frequency scan was chosen to identify the fundamental mode and the first few radial overtones ($k \lesssim 5$). The sign of the imaginary component of the eigenfrequency ω, determined from the non-adiabatic analysis was used to determine the stability of the mode. The sign convention in GYRE is that eigenfunctions are of the form

$$y(t) = A \exp[-i\omega t]. \tag{4.1}$$

Thus, if the imaginary component of the eigenfrequency is positive (negative), this mode is unstable (stable) and there is driving (damping) of that mode. In this

work, models described as stable/unstable are defined solely from the fundamental mode ($\ell = 0, k = 0$).

4.3 Results

We examine first the evolution of an EHB star progenitor, followed by that of a low-mass WD progenitor. The primary difference between the two cases is that, while both suffer a series of hydrogen shell flashes which lead to one or more loops in the HR (or $g - T_{\rm eff}$) diagram, only the first ignites helium in the core. Models for post-CEE pre-WD evolution have been presented elsewhere (Romero *et al.*, 2018, e.g.), but none have included the effects of radiative levitation.

4.3.1 0.46 $\mathrm{M}_\odot$ Post-Common-Envelope Pre-Extreme Horizontal Branch Star

The EHB progenitor model corresponds to model 3 of Byrne *et al.* (2018). This is a $1\,\mathrm{M}_\odot$ red giant star near the tip of the red giant branch, which has had almost all of the envelope removed to leave a $0.46\,\mathrm{M}_\odot$ star. This model was chosen as it undergoes a hydrogen shell flash, leading to a helium rich surface for at least part of its evolution, thus mimicking the surface properties of OGLE-BLAP-001. Fig. 4.1 shows the evolution of luminosity, fundamental period and surface gravity against effective temperature for the $0.46\,\mathrm{M}_\odot$ post-CEE star, for each of the diffusion options. Each symbol along the evolution tracks represents a MESA snapshot of the model which was analysed for pulsations. The small black dots represent models where the fundamental mode is stable. The red open circles indicate models that have an unstable fundamental mode and would be expected to pulsate. The dashed rectangle indicates the region of parameter space in which BLAPs are typically found, as defined by Pietrukowicz *et al.* (2017).

The results demonstrate three regions of instability during the transition from common envelope ejection to the horizontal branch. The first in the constant luminosity phase immediately succeeding the common envelope ejection. This region appears reasonably similar regardless of the choice of diffusion physics. The second begins in the low luminosity phase preceding the first helium flash (and corresponding hydrogen shell flash) and persists until the model reaches maximum

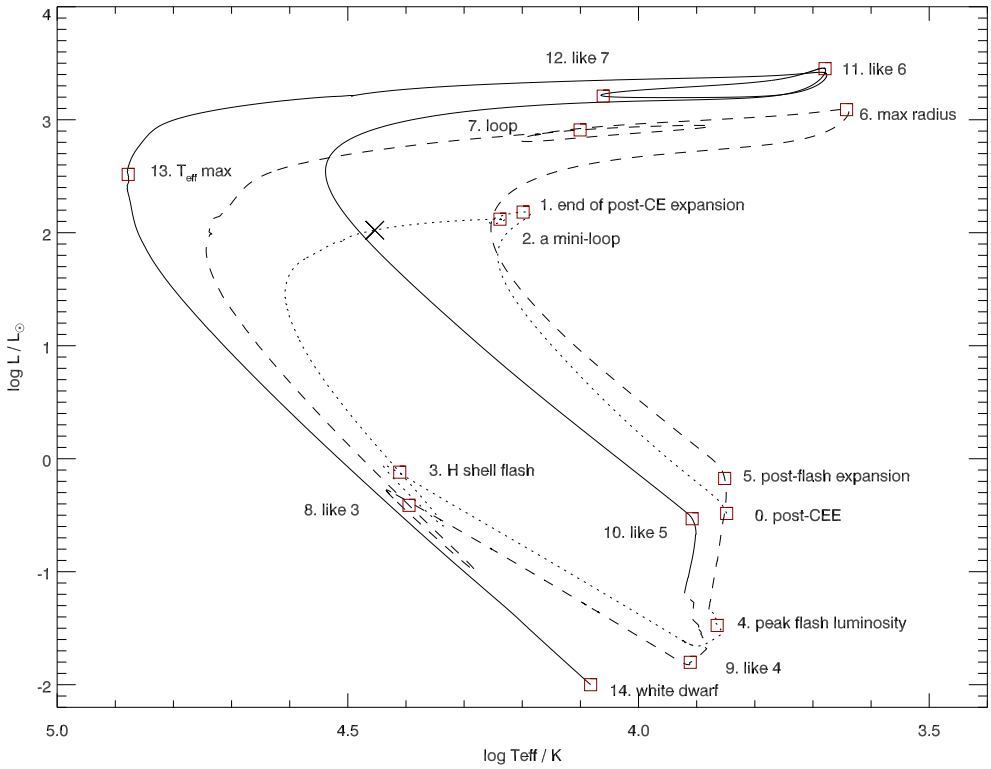

Figure 4.3: Evolution track of a $0.31\,M_\odot$ post-common-envelope model including radiative levitation. The square symbols indicate the location of the numbered points. For clarity, the continuous track is represented by three line-styles, from dotted, through dashed, to continuous. The cross indicates the model with parameters comparable to a BLAP which was chosen for further investigation.

post-flash luminosity. This phase is also seen in all three models. The final phase of instability begins when the model returns to an effective temperature of around 20 000 K ($\log(T_{\rm eff}) = 4.3$). In the basic and standard models, stability returns once the temperature exceeds around 32 000 K ($\log(T_{\rm eff}) = 4.5$), while instability persists in the complete model all the way to the extreme horizontal branch. The time taken to cross the instability strip between 20 000 K and 32 000 K (which roughly corresponds to the region of interest in which a BLAP may be observed) is approximately 1.5×10^4 yr.

4.3.2 0.31 $M_\odot$ Post-Common-Envelope Pre-White Dwarf Star

Fig. 4.2 shows the same results as Fig. 4.1, but for the model with a core mass of 0.31 $M_\odot$. One significant difference between these models is the number of hydrogen shell flashes which occur. In the basic model, only one hydrogen shell flash is seen, while both the standard and complete models undergo two hydrogen shell flashes, completing two loops in the diagram. Each loop occurs at a higher temperature and luminosity than the previous loop. The reason for the larger number of flashes is likely due to diffusion creating a hydrogen-abundance gradient such that shell flashes are less efficient, and leaving hydrogen-rich layers sufficiently massive to trigger additional flashes. As with the EHB progenitor, pulsation modes are unstable at a number of points. Similarly these occur during the constant luminosity phases of the evolution and in the aftermath of the hydrogen shell flash. However, in the case of the complete model, a large portion of the first (innermost) loop is found to be unstable, and it is this phase of evolution when the surface gravity, effective temperature and fundamental pulsation period tend to best match that of the BLAPs.

Since the track in Fig. 4.2 is complicated and novel, it is expanded and annotated in Fig. 4.3. Key points are identified as follows. The point labelled 0 indicates the initial state of the model after the rapid removal of mass from the envelope at a rate of 10^{-3} $M_\odot\,yr^{-1}$. The model then expands in order to return to equilibrium, reaching maximum radius at point 1, after about 5×10^2 yr. In doing so, it overshoots its equilibrium radius leading to another phase of contraction and expansions, which manifests itself as the loop at point 2, taking 6×10^4 yr. The star then evolves towards the white dwarf cooling track, taking 10^7 yr to reach point 3. At this point, the hydrogen luminosity begins to increase rapidly, indicating the onset of the hydrogen shell flash, which reaches peak luminosity when the model is at point 4 in the figure. After this, the strength of the flash starts to decline; energy produced during the flash is transported into the envelope, which heats and expands. The transition from point 3 to point 6 takes approximately 100 yr. At point 6, maximum expansion is achieved and the star

begins to contract towards white dwarf cooling track again. A small loop occurs, labelled as point 7. This appears to be related to a slight increase in the hydrogen

Table 4.1: Features in Fig 4.3 with a brief description of the events related to the numbered points, the time elapsed since the previous numbered point, the duration of the 'loops' (where relevant), total time elapsed since the end of the CE ejection phase and a brief description of the behaviour at these points.

Feature	$T_n - T_{n-1}$/yrs	T_{loop}/yrs	T_{tot}/yrs	Notes
0	0	0	0	Initial model properties after CE mass loss completed
1	4.16×10^2	-	4.16×10^2	End of post-CE expansion phase
2	4.75×10^2	6.12×10^4	6.23×10^4	A small loop as the model settles into an equilibrium state
3	1.03×10^7	-	1.04×10^7	Onset of the first hydrogen shell flash
4	8.81×10^0	-	1.04×10^7	Peak in hydrogen flash luminosity
5	2.86×10^1	-	1.04×10^7	Star expands in response to flash
6	5.71×10^1	-	1.04×10^7	End of post-flash expansion
7	5.30×10^1	3.91×10^2	1.04×10^7	A post-flash loop
8	2.93×10^7	-	3.97×10^7	Onset of the second hydrogen shell flash
9	1.10×10^{-1}	-	3.97×10^7	Peak in the flash luminosity, as 4
10	3.79×10^0	-	3.97×10^7	As 5
11	3.17×10^1	-	3.97×10^7	As 6
12	-	1.20×10^2	3.97×10^7	As 7
13	3.08×10^3	-	3.97×10^7	Temperature maximum
14	2.24×10^8	-	2.64×10^8	White dwarf with $\log L/\,L_\odot = -2$

luminosity, and possibly a redistribution of energy within the stellar envelope. The behaviour of the model from points 8 to 12 is similar to that from points 3 to 7, with comparable timescales. The star eventually cools to become a white dwarf at 14, taking 3.1×10^4 yr to contract from point 11 to maximum temperature at point 13, and a further 2.24×10^8 yr to cool to point 14, where the star has a luminosity of $10^{-2}\,L_\odot$.

Table 4.1 shows the elapsed time and time between various points on the evolution track shown in Fig. 4.3.

A clear result is that the inclusion of atomic diffusion and radiative levitation has a major impact, not only on the chemical structure and hence, potentially, on the pulsation properties, but also on the overall evolution of the models from envelope ejection through to the white dwarf phase. To compare with the $0.46\,M_\odot$ model, the time taken for this model to cross the temperature range of 20 000 K to 32 000 K is around 8×10^5 yrs. Thus, purely from an evolutionary timescale standpoint, a BLAP is more likely to be a $0.31\,M_\odot$ post-common envelope star than a $0.46\,M_\odot$ star, since the lower mass object spends about 50 times as long crossing the region of interest.

4.3.3 Driving

In order to identify if any of these models could produce BLAP behaviour, individual models from each evolution track falling in the BLAP parameter range were selected (Fig. 4.4, Table 4.2). Figs. 4.5 and 4.6 show the logarithm of opacity ($\log(\kappa)$) and the derivative of the work function ($\mathrm{d}W/\mathrm{d}x$) as a function of interior temperature for the pre-EHB and pre-WD models respectively. The mass fraction of helium and combined mass fraction of iron and nickel are also included.

These figures show that the driving zones in the models (the location of the peak in dW/dx) coincide with the location of the opacity maximum related to the ionisation of iron and nickel at $\log(T) \simeq 5.3$. This is a clear indication that for models with unstable modes, the pulsations observed in these models are driven by the κ-mechanism arising from the opacity of iron-group elements. It is particularly apparent in the case of the $0.31\,M_\odot$ model, that the size of the opacity bump is significantly larger when radiative accelerations are computed.

Table 4.2: Properties of models selected for detailed analysis, as shown in Fig. 4.4.

Model	Physics	$\frac{M}{M_\odot}$	$\frac{M_{Core}}{M_\odot}$	$\log\left(\frac{R_*}{R_\odot}\right)$	$\log\left(\frac{L_*}{L_\odot}\right)$	$\log\left(\frac{g}{cm\,s^{-2}}\right)$	$\log\left(\frac{T_{eff}}{K}\right)$	$\log\left(\frac{P_0}{s}\right)$	Stability
pre-EHB	Basic	0.46215	0.46215	-0.2002	2.3163	4.5030	4.4408	3.0445	Stable
	Standard	0.46215	0.46215	-0.3237	2.3171	4.7502	4.5028	3.1309	Stable
	Complete	0.46215	0.46215	-0.3416	2.2738	4.7712	4.5009	3.1096	Unstable
pre-WD	Basic	0.31045	0.30776	-0.3919	2.0201	4.7137	4.4626	3.1169	Stable
	Standard	0.31045	0.30772	-0.3724	2.0264	4.6747	4.4544	3.1465	Stable
	Complete	0.31045	0.30774	-0.3727	2.0223	4.6798	4.4536	3.1236	Unstable

This is due to the accumulation of iron and nickel in this region of the envelope, which illustrates the important role played by radiative levitation. Additionally, the fundamental modes of the horizontal branch models are only unstable when radiative levitation is included, as shown in Fig. 4.1. This is indicative that radiative levitation plays a key role in causing sufficient amounts of iron to accumulate in the envelope of the star to drive pulsations. This result is not surprising, as it has been widely shown that the presence of enhanced levels of iron and nickel in the envelope of hot subdwarfs is needed to drive the pulsations (Charpinet *et al.*, 1996; Fontaine *et al.*, 2008; Hu *et al.*, 2011; Jeffery & Saio, 2007; Michaud *et al.*, 2011, e.g). Furthermore, Romero *et al.* (2018) suggested that iron and nickel opacity was the driving mechanism for BLAPs. They used an artificial uniform enhancement of metallicity to replicate the effects of radiative levitation in a simple manner. The more detailed radiative levitation calculations carried out in this work agree with the suggestion that iron and nickel opacity is responsible for the pulsations seen in BLAPs.

4.3.4 Rate of Period Change

Observed period changes provide vital clues about other changes in a star, particularly one which may be evolving quickly. The observations of Pietrukowicz *et al.* (2017) report rates of period change, $\dot{\Pi}$, in the range $-3 \times 10^{-7}\,\mathrm{yr}^{-1} \leq \dot{\Pi} \leq +8 \times 10^{-7}\,\mathrm{yr}^{-1}$, where $\dot{\Pi}$ is defined as

$$\dot{\Pi} = \frac{\Delta P}{\Delta t}\frac{1}{P} \tag{4.2}$$

and where ΔP is the change in period in a time interval Δt. Romero *et al.* (2018) report values of $\dot{\Pi} \approx \pm 10^{-7} - 10^{-5}\,\mathrm{yr}^{-1}$ for their template model.

With the inclusion of the effects of radiative levitation, the rate of period change derived for the $0.31\,\mathrm{M}_{\odot}$ model with radiative levitation in this work, identified as the 'complete' $0.31\,\mathrm{M}_{\odot}$ model in Fig. 4.4 and Table 4.2, we find a value of $\dot{\Pi} \simeq -3 \times 10^{-6}\ \mathrm{yr}^{-1}$, which is comparable in magnitude to those of the Romero *et al.* (2018) models and the Pietrukowicz *et al.* (2017) observations.

A puzzle for both of the latter is that both negative and positive values of $\dot{\Pi}$ are reported. Generally speaking, a pulsation period will decrease (negative $\dot{\Pi}$)

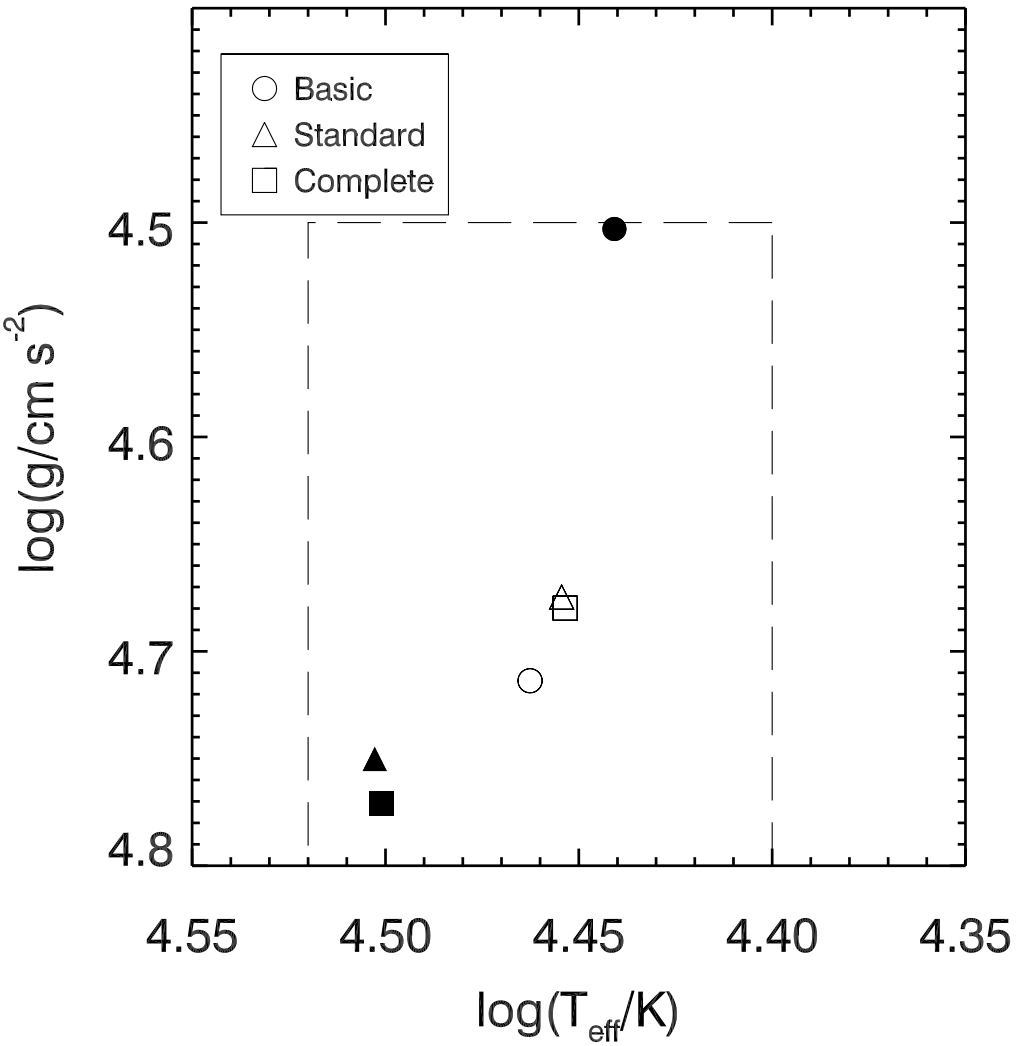

Figure 4.4: Models chosen from the different evolution tracks as candidate BLAP objects on a surface gravity-effective temperature diagram. The filled symbols represent models of the $0.46\,M_{\odot}$ post-CEE star while the open symbols represent models of the $0.31\,M_{\odot}$ post-CEE star. The dashed box indicates part of the boundary region in which BLAPs have been identified, and extends to $\log(g) \approx 5.3$.

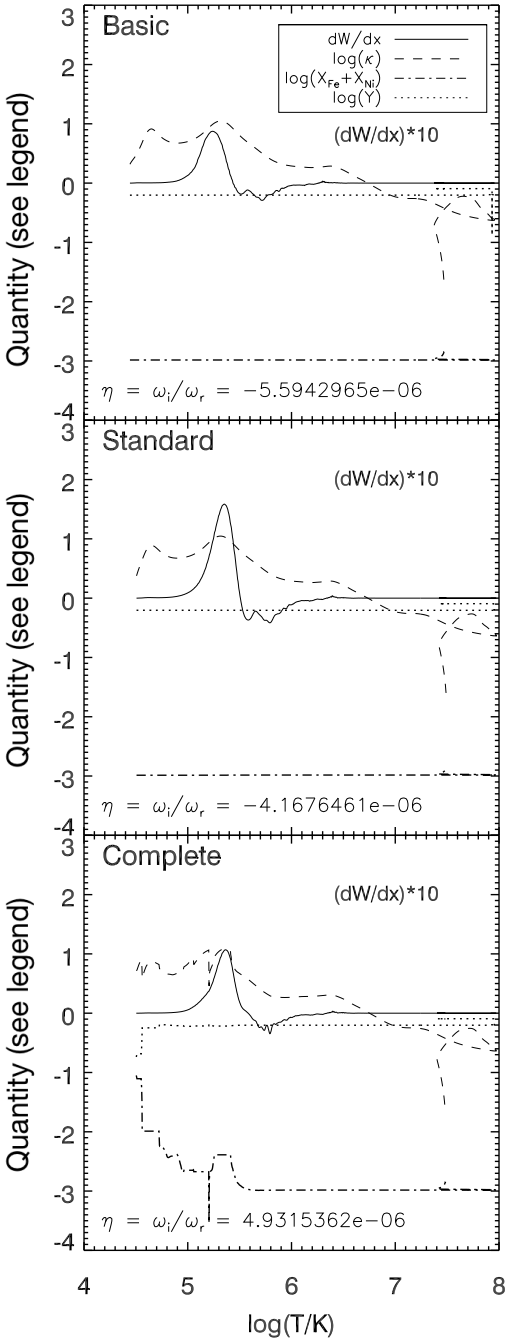

Figure 4.5: Opacity ($\log \kappa/\mathrm{cm}^{-1}$) and derivative of the work function of the fundamental mode ($\mathrm{d}W/\mathrm{d}x$, in units of $\mathrm{G\,M_*^2\,R_*}$) as a function of temperature for the $0.46\,\mathrm{M}_\odot$ pre-EHB models from Table 4.2. Where indicated, $\mathrm{d}W/\mathrm{d}x$ has been multiplied by 10 for visibility. The mass fraction of helium and the combined mass fraction of iron and nickel are also shown. All functions are multiply valued for $\log T/\mathrm{K} > 7.5$ owing to the temperature inversion caused by neutrino cooling in the degenerate core.

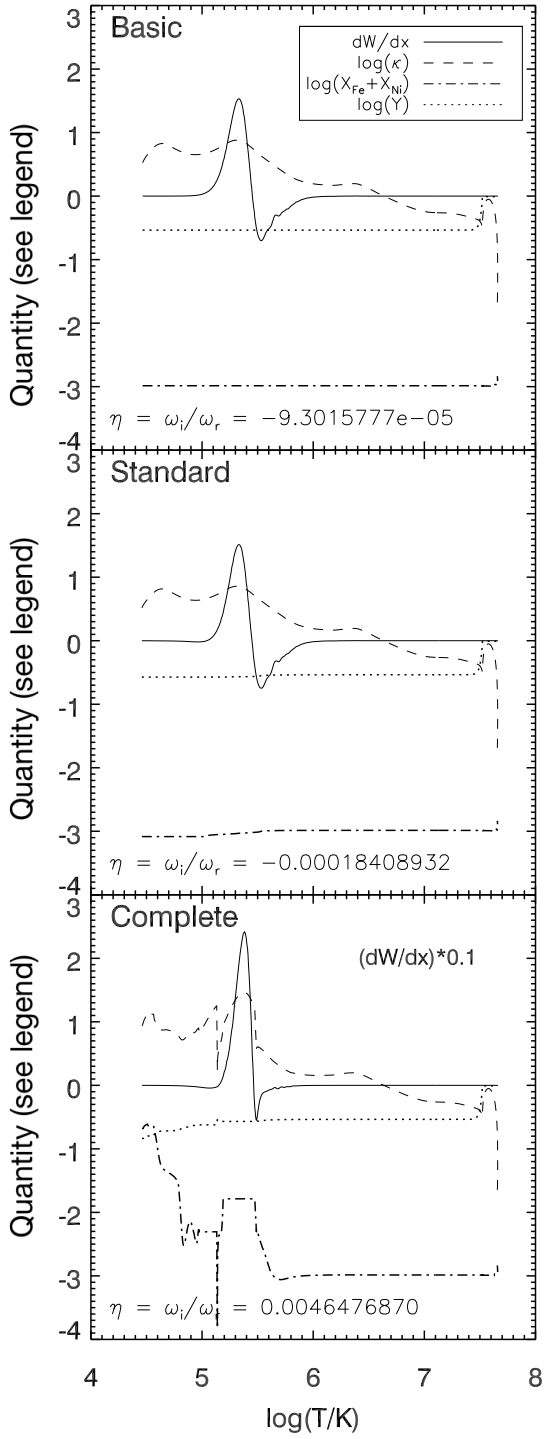

Figure 4.6: Same as Fig. 4.5 for the 0.31 $M_\odot$ pre-WD models from Table 4.2. Where indicated, dW/dx has been multiplied by 0.1 for visibility alongside the other parameters in the diagram.

in a star which is contracting, and increase in a star which is expanding. It is not entirely clear from Romero *et al.* (2018) how values of $\dot{\Pi}$ were computed for their template model, but since all of their models are for contracting stars, only negative values should be expected. The challenge provided by the Pietrukowicz *et al.* (2017) observations is that they imply BLAPs include both contracting and expanding stars.

Since the model is on the contracting stage of the evolution track (between points 2 and 3 on Fig. 4.3, we obtain a negative value of $\dot{\Pi}$. Another part of the track passes close to the BLAP zone (points 10 to 11 on Fig. 4.3) during an expansion phase, but with such a short lifetime (31 yr, Table 1) that (a) it would be an unlikely observation and (b) $\dot{\Pi}$ would be orders of magnitude larger than any observed.

The most likely source of positive values of $\dot{\Pi}$ is an expanding star. From the models studied in this chapter, the closest match to this is provided by loops associated with off-centre helium ignition flashes in the 0.46 $M_{\odot}$ star, prior to core helium ignition, as seen in Fig. 4.1. While the temperature and luminosity of the models presented here do not agree with the observations by Pietrukowicz *et al.* (2017), the exact locations of these loops are dependent on the models used and the assumptions around the behaviour of common envelope ejection, such as the amount of hydrogen envelope remaining after common envelope ejection among other things. Thus it is possible that stars in this phase of evolution could be the source of BLAPs with a positive value of $\dot{\Pi}$.

4.3.5 Detailed Pulsation Properties

Close examination of the results of the stability analysis provides an interesting insight into the theoretical predictions. In this section the pre-subdwarf and pre-white dwarf models referred to are the models in Figure 4.4, specifically the individual models which include radiative levitation (labelled as 'complete'). For the purposes of this section, the pre-subdwarf and pre-white dwarf models shall be referred to as Model S and Model W respectively. A list of the properties of the radial modes analysed in Model S and Model W are presented in Table 4.3 and Table 4.4 respectively. In these tables, n_p represents the p-mode wavenumber

Table 4.3: Pulsation properties for the first few $\ell = 0$ modes for a representative pre-subdwarf model including radiative levitation, model S.

n_p	$\nu/\,[\mu\mathrm{Hz}]$	$\Pi/\,[\mathrm{min}]$	Stability	$\tau_g/\,[\mathrm{day}]$
1	777.0	21.5	Unstable	481
2	1063	15.7	Unstable	13.0
3	1297	12.9	Unstable	1.54
4	1512	11.0	Unstable	0.78
5	1743	9.56	Unstable	19.8
6	1988	8.39	Stable	-0.33
7	2239	7.45	Stable	-0.15

Table 4.4: Pulsation properties for the first few $\ell = 0$ modes for a representative pre-white dwarf model including radiative levitation, model W.

n_p	$\nu/\,[\mu\mathrm{Hz}]$	$\Pi/\,[\mathrm{min}]$	Stability	$\tau_g/\,[\mathrm{day}]$
1	752.3	22.2	Unstable	0.53
2	872.9	19.1	Unstable	0.24
3	1111	15.0	Unstable	0.87
4	1328	12.6	Unstable	0.65
5	1516	11.0	Stable	-1.03
6	1766	9.44	Stable	-0.10

(with 1 representing the fundamental mode), ν is the frequency of the pulsation in units of μHz, Π is the period of the pulsation in minutes, and τ_g is the growth time of the pulsation. τ_g is calculated by first taking the ratio of the real and imaginary parts of the eigenfrequency (ω_r/ω_i) and dividing the result by 2π to obtain the growth time in pulsation cycles. Multiplying by Π will give the physical growth time, the amount of time it takes the pulsation to grow by a factor of e, Euler‘s number. This follows the approach of Jeffery & Saio (2006a).

One striking result is that the growth time of the pulsations is extremely short, implying the modes are generally highly unstable. This is much shorter than the evolutionary timescale of these stars. The fundamental mode in Model S has a growth time about 4 orders of magnitude longer than Model W (500 days compared to 0.5 days), providing further reason to prefer the pre-white dwarf evolutionary scenario to explain these high-amplitude pulsations. The tables also show that a number of other radial modes are expected to be unstable in addition to the fundamental mode. At present, there is no evidence of multi-mode

Table 4.5: Basic summary of pulsation properties for $\ell = 1$ and $\ell = 2$ modes which are most unstable in models S and W.

Model	ℓ	$\Pi_{\text{most unst.}}$ / [min]	$\tau_{g,\,\text{most unst.}}$ / [day]	$N_{\text{unst. modes}}$
S	1	10.80	1.08	19
S	2	11.33	2.23	30
W	1	18.83	0.61	25
W	2	19.63	1.51	40

pulsation in any known BLAPs. Further study of these stars, both observational and theoretical, may be able to provide insight into this discrepancy.

4.3.5.1 Extension to Higher Mode Orders

A similar pulsation analysis can be carried out for higher mode orders to examine whether non-radial modes are also driven. Figure 4.7 presents a propagation diagram for $\ell = 1$ and $\ell = 2$ modes for both Model S and Model W. This is similar to Figure 1.6, but with the addition of some pulsation information. The horizontal dashed lines indicate the eigenfrequencies of pulsation modes which are found to be unstable in each case. A number of unstable modes exist, all passing through both the g-mode and p-mode cavities, producing mixed modes (modes with both p-mode and g-mode characteristics). In each case, the periods of the unstable modes lie between 10 and 27 minutes. Modes of higher and lower frequencies were found to be stable. Growth rates for some of these modes are quite large, with values of τ_g of thousands of years for some modes, while the most unstable non-radial modes in both models have growth times on the order of 1 day. The most unstable mode in each case is listed in Table 4.5, along with the total number of unstable modes present in each model for both values of ℓ. As with the additional unstable radial modes, these unstable non-radial modes are not observed in any BLAPs observed to date. It is worth noting that while the stability analysis can tell us whether a mode is stable or unstable, it can not make definitive predictions about the relative amplitudes of the different modes. It is possible that these non-radial modes are present in BLAPs, but have much lower amplitudes.

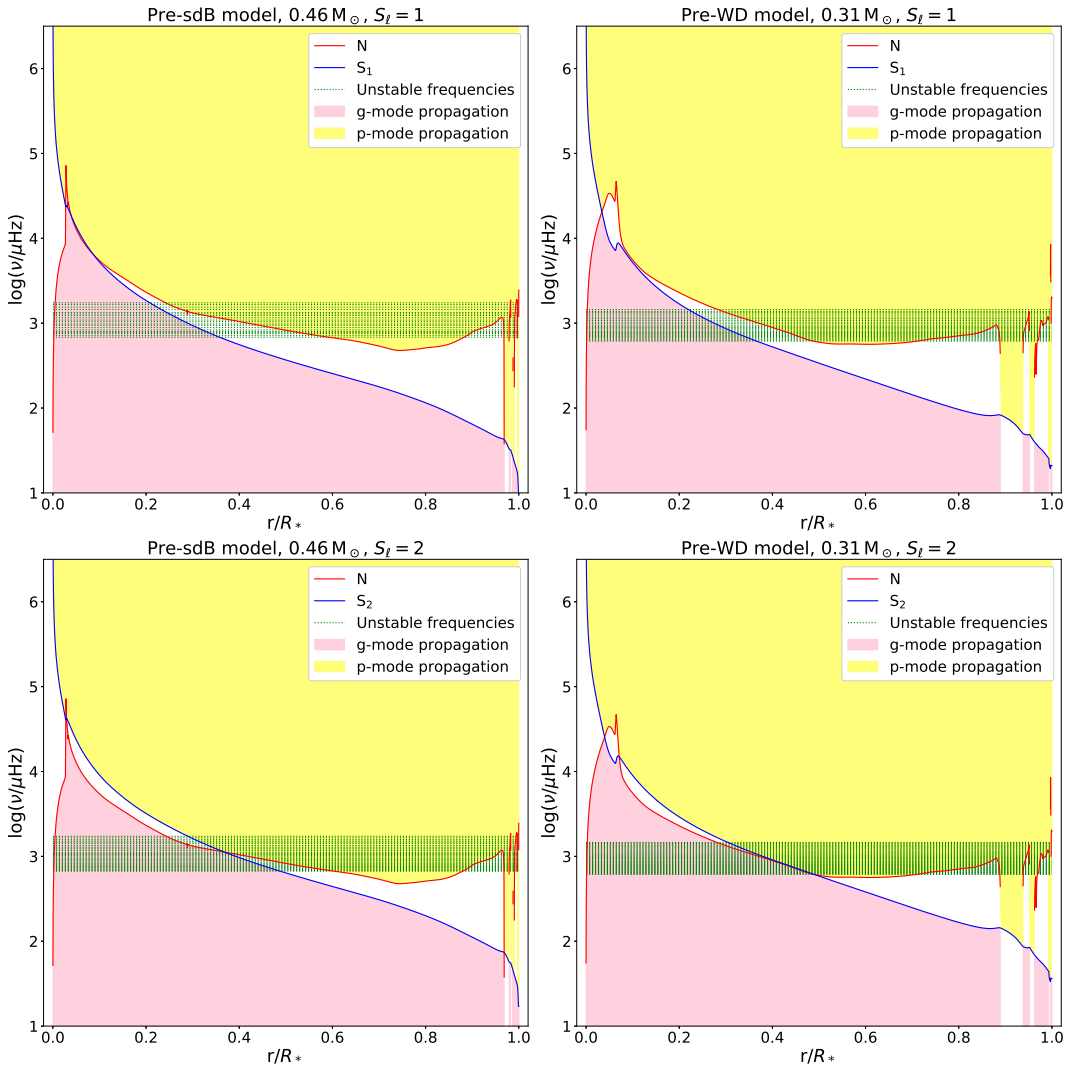

Figure 4.7: Mode propagation diagrams for $\ell = 1$ (upper panels) and $\ell = 2$ (lower panels) for Model S (left panels) and Model W (right panels). The p-mode and g-mode propagation regions are highlighted in light yellow and light magenta respectively. The frequencies of unstable pulsation modes are indicated by the green dotted lines.

4.4 Discussion

Fig. 4.8 compares the instability of models shown in Figs. 4.1 and 4.2 with the survey of instability in hydrogen-deficient stellar envelopes by Jeffery & Saio (2016). The high-luminosity tracks, show blue edges in approximately the same locations. Given that the computational tools are completely independent, this validates the methods. The most significant differences are instability in the models approaching the EHB and in hottest pre-WD models each time they approach a maximum in effective temperature.

There are several significant differences between the models of Jeffery & Saio (2016) and those presented here. The former consider homogeneous stellar envelopes in full radiative and hydrostatic equilibrium. Such models work well for early-type stars which evolve slowly. The mean-molecular weight in the envelope, which governs the equation of state, is dominated by the hydrogen and helium abundances. The opacity in the major driving zones is governed by these and the metal abundances. The energy flux (luminosity) is assumed to be constant throughout the envelope. By ensuring that the composition reflects the mean-molecular weight through the envelope, and the distribution of metals in the potential driving zones, pulsation stability can be explored in large parameter spaces.

The envelope models shown in Fig. 4.8 differ from the current MESA models in two crucial ways. The first is that, as a result of radiative levitation, metal abundances in the driving zones are very substantially enhanced relative to the initial metallicity (Z), which is similar to that adopted in the envelope models. The radiative enhancement can be simulated in the envelope models by increasing the iron and nickel contribution to the opacity by, say, a factor 10 (Jeffery & Saio, 2006b, cf.). The bottom row of Fig. 4.8 shows how such an increase also increases the parameter space (for hot stars) in which the models are unstable. As shown in Figs. 4.5 and 4.6, the combined mass fraction of iron and nickel, $\log(X_{\rm Fe}+X_{\rm Ni})$, in the driving region is around –2.4 for the chosen evolutionary phase of the 0.46 $M_\odot$ model which closely resembles a BLAP, while $\log(X_{\rm Fe}+X_{\rm Ni})=-1.8$ for the 0.31 $M_\odot$ model.

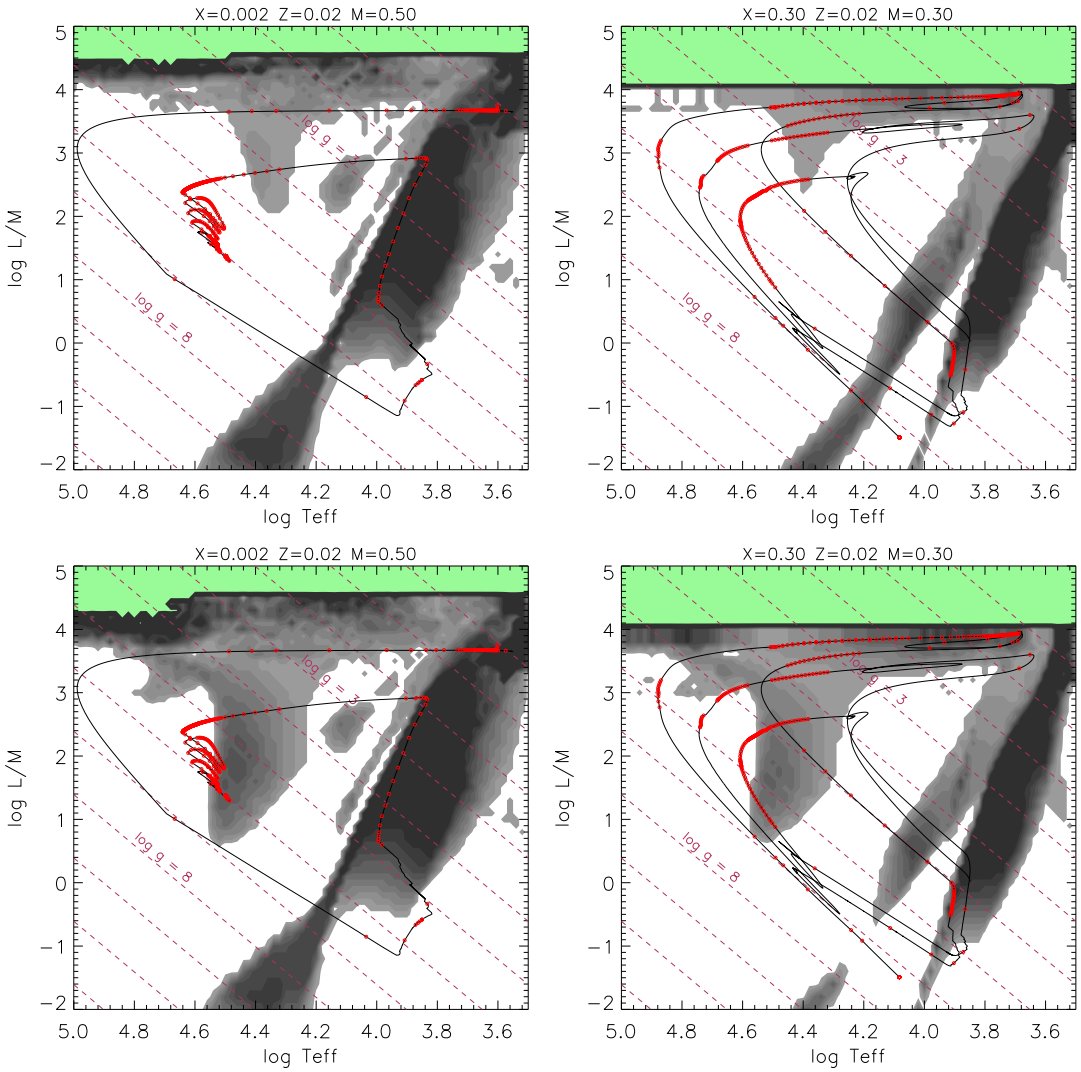

Figure 4.8: Evolution tracks for post-CEE stars with radiative levitation superimposed on the loci of pulsationally unstable homogeneous envelopes obtained by Jeffery & Saio (2016), with compositions and masses as labelled. $T_{\rm eff}$ is in degrees kelvin; the luminosity and mass are in solar units. The left panels show the track (solid line) of a 0.46 $M_\odot$ pre-EHB star (cf. Fig. 4.1) and the right panels show the track of 0.31 $M_\odot$ pre-WD (cf. Fig. 4.2). Red circles represent pulsationally unstable models on the evolution track of post-CEE models. The grey-scale contour plot represents the *number* of unstable radial modes, with the lightest shade marking the instability boundary (one unstable mode), and the darkest shade representing ten or more unstable modes. Broken diagonal lines represent contours of constant surface gravity at $\delta \log g = 1$ (g labelled in cms^{-2}). Pale green denotes regions where envelope models do not converge. The top row assumes a scaled-solar metallicity with $Z = 0.02$. The bottom row assumes the same metal abundances but with iron and nickel increased by a factor of 10 (Jeffery & Saio, 2006b).

The second difference is that the MESA evolution models correctly include the gravothermal term in the energy equation ($\mathrm{d}l/\mathrm{d}m = \epsilon - T\mathrm{d}S/\mathrm{d}t$) which is non-negligible during phases of rapid evolution such as those illustrated in Figs. 4.1 and 4.2. It is not clear how much this affects the constant flux assumption ($\mathrm{d}l/\mathrm{d}m = 0$) used for the Jeffery & Saio (2016) stability survey, but it is an interesting question of wider significance to objects sometimes referred to as 'bloated' stars.

4.4.1 Bloated Stars

Terms such as 'bloated' or 'inflated' are sometimes used to refer to envelopes of stars which are not in full hydrostatic, radiative and thermal equilibrium. This may be a consequence of either a sudden increase in the core luminosity (core or shell flash), or a loss of radiative support when a nuclear energy source is depleted. The implication is that flux entering the envelope from below is substantially different from that leaving the surface. The temperature and density structure must therefore adjust until the two quantities are equal; the envelope must either contract to make good a deficit, or expand to absorb an excess. In the case of contraction, the process will normally be quasi-static and changes take place on the thermal timescale of the envelope. Expansion phases may also be in thermal equilibrium, but can sometimes be driven dynamically by more explosive events (e.g. shallow shell flashes). The latter can give rise to two types of 'bloated' envelope; first, the expanding envelope driven dynamically by a nuclear ignition and, second, a contracting envelope after the nuclear energy source has switched off. The fact that the model is either expanding or contracting on short timescales indicates that it is not in equilibrium. In either case, the structure may be quite different from that of an envelope in which $\mathrm{d}l/\mathrm{d}m = 0$. The question is how this affects pulsation stability, which occurs on a dynamical timescale.

The question can be addressed for an individual case by looking at the magnitude of the gravothermal term in models pertaining to BLAPs. Fig. 4.9 shows the magnitude of the gravothermal term in the sense $\mathrm{d}l/\mathrm{d}m$ through the envelopes of two models. Note that the sign of $\mathrm{d}l/\mathrm{d}m$ changes in the region of the iron-nickel opacity bump. So although the bulk of the envelope is contracting, and hence

converting gravitational potential energy to heat ($\mathrm{d}l/\mathrm{d}m > 0$), heat is being re-absorbed within the opacity bump. The reason is that the opacity bump can be attributed primarily to the ionization of K- and L-shell electrons in the iron and nickel atoms Opacity Project Team (1995, 1997). The same ionization produces an increase in the local specific heat capacity. As the envelope contracts, all layers of the star contract and heat; as the ionization zone moves outward into a new layer, it locally traps heat ($\mathrm{d}l/\mathrm{d}m < 0$). Once ionization is complete, the same layer, which is now beneath the ionization zone, continues to contract and release heat as before ($\mathrm{d}l/\mathrm{d}m > 0$).

The non-zero value of the gravothermal term has several consequences for the structure and stability of the envelope. The most obvious is that it directly affects the radiative gradient through the transport equation (Equation 4.3)

$$\frac{\mathrm{d}T}{\mathrm{d}m} = \frac{3\kappa\rho^2 l}{4acT^3} \tag{4.3}$$

via the flux l. The gradient is further affected through the opacity κ when radiative acceleration operates to concentrate material in locations where its own specific opacity is high. The perturbation to the radiative gradient will propagate through the equation of state to the pressure and density, and hence to the overall stability.

Previous studies have shown that the non-adiabatic term for stars in thermal imbalance contributes to a destabilisation of the star (Aizenman & Cox, 1975; Cox, 1980, e.g.). This contraction, which manifests as a local heat loss in a static model appears as a source of heat in the pulsating star, tending to lead to an amplification of the pulsations, as pressure variations begin to lag slightly behind density variations. This appears to be the case here, as the models appear to be unstable beyond the blue-edge of the instability regions found in Fig. 4.8.

4.5 Conclusions

The pulsation properties of post-common envelope stars with core masses of 0.31 $\mathrm{M}_\odot$ and 0.46 $\mathrm{M}_\odot$ were investigated as they evolve from the red giant branch to become a low mass helium white dwarf and a hot subdwarf star respectively. The

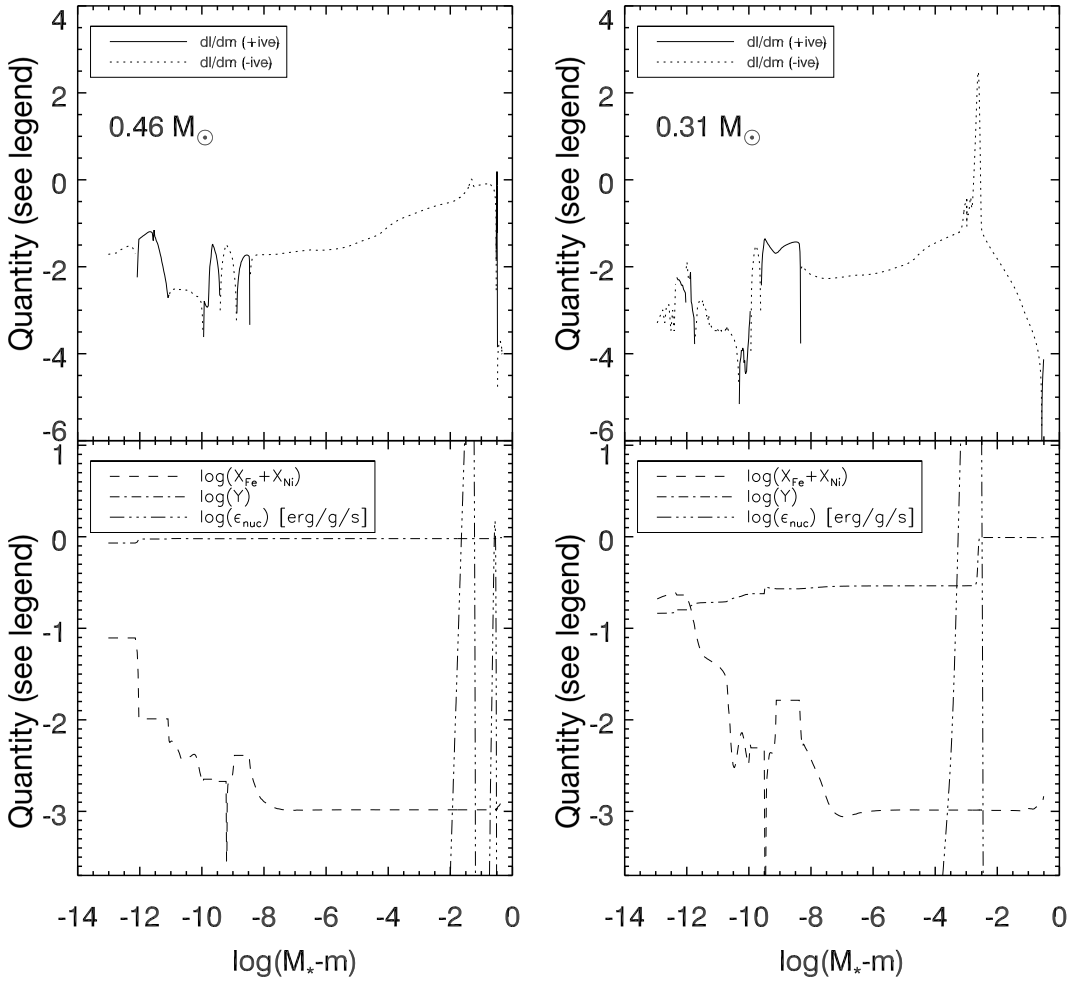

Figure 4.9: Properties of the $0.46\,M_\odot$ (left) and $0.31\,M_\odot$ (right) candidate models as a function of mass co-ordinate. The top panels show the magnitude and sign of dl/dm. The lower panels show the rate of energy generation due to nuclear burning, the mass fraction of helium and the combined mass fraction of iron and nickel.

effect of the presence or absence of atomic diffusion and radiative levitation on the results was also examined. It was shown that objects with effective temperatures comparable to those of the BLAPs measured by Pietrukowicz *et al.* (2017) are unstable to pulsations with fundamental mode periods in the range of around 15-40 minutes, comparable to that seen in BLAPs. In the case of the $0.31\,M_\odot$ model, these fundamental modes are only unstable in the case where radiative levitation is included. In the $0.46\,M_\odot$ model, some of the evolution through this region is unstable without radiative levitation, however the addition of radiative levitation significantly expands the region of instability. One of the proposed BLAP structures from the envelope models of Pietrukowicz *et al.* (2017) is a $0.31\,M_\odot$ shell hydrogen burning object. As these models have shown, radiative levitation is necessary in order for such objects to pulsate in the fundamental mode.

Comparison of the time during which the $0.46\,M_\odot$ and $0.31\ M_\odot$ models are evolving through the instability region associated with the BLAPs finds that the $0.31\,M_\odot$ are much longer-lived in this region and are more likely to be observed. Additionally, in terms of temperature and gravity, the $0.31\,M_\odot$ model passes more centrally through this region than the $0.46\,M_\odot$ model (compare the lower right panels of Fig. 4.1 and Fig. 4.2). These results indicate that BLAPs with negative rates of period change are more likely to be low mass pre-white dwarfs than pre-extreme horizontal branch stars. The situation is less clear for BLAPs with a positive rate of period change. The closest matching objects in these models are pre-extreme horizontal branch stars in the expanding phase of their off-centre helium flashes, but these do not match the observational parameters of BLAPs given the methodology and assumptions about common envelope evolution made in this work.

The enhancement of iron and nickel occurs almost exclusively in the pulsation driving zone, which is around the iron opacity peak at $T \simeq 2 \times 10^5\,K$. This spatially confined enhancement is likely to give more realistic structure of the star than the uniform envelope abundance enhancement usually added to static pulsation models. When radiative levitation is added to the $0.46\,M_\odot$ model it reinforces the fact that levitation of iron and nickel is key to the development of pulsations in hot subdwarf stars.

These results have also led to the consideration of the effect of thermal imbalance in the envelope on the pulsational stability of the star. Previous work by Aizenman & Cox (1975) and others showed that contraction of the star tends to be destabilising, which provides an explanation for why the instability region for the models presented here extended bluewaard of the instability region for models in thermal equilibrium presented by (for example) Jeffery & Saio (2016).

5

Pulsations in faint blue stars

The work in this chapter has been published as Byrne & Jeffery (2020)

5.1 Introduction

Stellar variability enables astronomers to learn more about a star or stellar system than from a star of constant brightness. For example, eclipses can be used to determine binary orbital parameters, novae can be used to learn more about close binary interactions and stars which are intrinsically unstable and pulsate can provide clues about the internal structure of a star through asteroseismology.

As previously discussed in Section 1.8.1 and Chapter 4, the discovery of a new class of pulsating star, referred to as blue-large amplitude pulsators (BLAPs), was reported by Pietrukowicz *et al.* (2017). A new class of pulsating star presents challenging theoretical questions such as what the driving mechanism is, what their evolutionary status is and how many such objects could be found. Detailed evolutionary calculations for both pre-EHB stars and low-mass pre-white dwarfs including the effects of atomic diffusion were carried out in Chapter 4 (henceforth referred to as Byrne & Jeffery, 2018) to test the hypothesis that pre-hot subdwarf and pre-low-mass white dwarf stars could pulsate in a manner comparable to the

observations. By carrying out non-adiabatic pulsation analyses, it was shown that models of both types will evolve to become unstable in the temperature region in which BLAPs are observed, with pulsations in the appropriate period range. The driving mechanism was identified as the opacity bump (κ-mechanism) at the iron opacity peak. Byrne & Jeffery (2018) found that it is necessary to account for the effects of radiative levitation.

Radiative levitation is a diffusive process whereby the outgoing radiative flux from the star imparts a force on the ions in the star, with the magnitude of the force depending on the precise atomic structure of the ion. Elements such as iron have a complex 'forest' of atomic transition lines and are thus more susceptible to the radiative force than relatively simple species such as helium. Stellar models including the effects of radiative levitation in hot subdwarf stars have confirmed that iron accumulates in the metal opacity bump, or Z-bump, (Hu *et al.*, 2011; Michaud *et al.*, 2011) and in a self-consistent stellar evolution model, radiative levitation has been demonstrated to have a significant effect in the pre-subdwarf phase of evolution (Chapter 3 and Byrne *et al.*, 2018).

Radiative levitation enables sufficient accumulation of iron and nickel around the opacity maximum at $\sim 2 \times 10^5\,\mathrm{K}$ to create a large enough opacity bump to drive the pulsations. However, it was concluded that on the basis of evolutionary timescales at the observed surface gravities, the $0.3\,\mathrm{M}_\odot$ pre-white dwarf model was a more likely candidate to explain the BLAPs than the shorter-lived pre-EHB models.

Low-mass white dwarfs ($\mathrm{M} \lesssim 0.5\,\mathrm{M}_\odot$) are unusual in that they cannot form within the current age of the Universe through single-star evolution channels, thus requiring interaction with a binary companion to form. A more detailed description of low-mass white dwarfs has been provided in Section 1.8.

The κ-mechanism and radiative levitation of iron and nickel are also known to be responsible for the pulsations seen in hot subdwarf stars. Hot subdwarfs are low-mass ($\sim 0.46\,\mathrm{M}_\odot$) core-helium-burning stars with low-mass hydrogen envelopes. Like low-mass white dwarf, hot subdwarfs also form through binary interactions removing the bulk of their hydrogen rich envelope, with the important distinction that the envelope is only stripped when the star has grown a core

large enough for helium fusion to take place. There are both rapid and slow subdwarf pulsators which were discovered by Kilkenny *et al.* (1997) and Green *et al.* (2003) respectively. Radiative levitation of iron-group elements was predicted to be responsible for the rapid pulsators before they were discovered (Charpinet *et al.*, 1996), and the same mechanism was subsequently found to be responsible for the slow pulsators (Fontaine *et al.*, 2003).

Following the discovery of BLAPs, another new group of pulsating variable stars was discovered by the Zwicky Transient Facility (ZTF) (Kupfer *et al.*, 2019). These variable stars show similar large amplitude variability as that seen in BLAPs, while their spectroscopically determined surface gravities are much higher and they have much shorter periods. These higher surface gravities and surface temperatures place them amongst the hot subdwarf pulsators in the $\log g - \log T_{\rm eff}$ diagram. Table 5.1 compares the general population properties of the Kupfer *et al.* (2019) and Pietrukowicz *et al.* (2017) pulsators and both classes of hot subdwarf variables, while Table 5.2 lists the properties of the individual stars for which spectroscopic follow-up has been completed. This new discovery raises an interesting question of whether these two groups of faint, large-amplitude pulsators are related to each other and/or to the hot subdwarfs. Kupfer *et al.* (2019) computed some helium-core pre-WD models and found that lower mass ($\sim 0.28\,M_{\odot}$) pre-WDs provide a very good match in terms of the pulsation periods, while a model of a shell He-burning, post-EHB star gives pulsation periods which are longer than those observed, making this a less likely candidate. Thus the current opinion appears to be that the pulsators of Pietrukowicz *et al.* (2017) and Kupfer *et al.* (2019) are related objects, different only in mass. This raises the question of whether these are two distinct groups of pulsator or part of a contiguous region of instability, which may become populated as these large-scale sky surveys such as ZTF and OGLE continue to monitor the sky.

In order to investigate this, we decided to expand on the work of Byrne & Jeffery (2018) and examine a larger region of parameter space, looking at a wide range of pre-WD masses and probe the stability of these stars as they evolve. This will enable us to determine the extent to which these pre-white dwarf stars could be unstable and make predictions about what further discoveries might be expected in this region of parameter space.

Table 5.1: Observed properties of the two groups of faint blue variable stars, alongside the rapidly-pulsating and slowly-pulsating subdwarf B stars for comparison.

	'Low-gravity BLAPs'[1]	'High-gravity BLAPs'[2]	sdBVr[3]	sdBVs[4]
Effective temperature (K)	$26\,000 - 32\,000$	$31\,000 - 34\,000$	$30\,000 - 36\,000$	$24\,000 - 30\,000$
Surface gravity ($\log g/\mathrm{cm\,s^{-2}}$)	$4.20 - 4.61$	$5.31 - 5.70$	$5.2 - 6.1$	$5.2 - 5.7$
Pulsation period (s)	$1\,340 - 2\,360$	$200 - 480$	$90 - 500$	$2\,700 - 7\,200$
Pulsation amplitude (mag)	$0.2 - 0.4$	$0.05 - 0.2$	$0.001 - 0.064$	$\lesssim 0.05$

References: 1: Pietrukowicz *et al.* (2017), 2: Kupfer *et al.* (2019), 3: Østensen *et al.* (2010), 4: Green *et al.* (2003)

Table 5.2: Spectroscopically determined properties of BLAPs for which follow-up observations have been carried out.

Name	T_{eff}/K	$\log g/\mathrm{cm\,s^{-2}}$	P (s)	Ref.
OGLE-BLAP-001	30 800	4.61	1695.6	1
OGLE-BLAP-009	31 800	4.40	1916.4	1
OGLE-BLAP-011	26 200	4.20	2092.2	1
OGLE-BLAP-014	30 900	4.42	2017.2	1
HG-BLAP-1	34 000	5.70	200.20	2
HG-BLAP-2	31 400	5.41	363.16	2
HG-BLAP-3	31 600	5.33	438.83	2
HG-BLAP-4	31 700	5.31	475.48	2

Souces: 1: Pietrukowicz *et al.* (2017), 2: Kupfer *et al.* (2019)

5.2 Methods

A grid of models was constructed to examine a wide range of masses for pre-WD objects, from very low masses ($< 0.2\,\mathrm{M}_\odot$) to just below the critical mass for helium ignition, at which point the star would evolve to become a hot subdwarf prior to becoming a white dwarf ($\sim 0.46\,\mathrm{M}_\odot$).

5.2.1 Evolution Models

Evolution models were computed using MESA (Paxton *et al.*, 2011, 2013, 2015, 2018, 2019, revision 11701). Physics options were similar to those used in Byrne & Jeffery (2018), namely the Schwarzchild convection criterion, a convective overshoot parameter $\alpha_{MLT} = 1.9$ following Stancliffe *et al.* (2016), no mass loss (aside from the initial stripping of the red giant progenitor) and an initial metallicity of $Z = 0.02$ with the mixture of Grevesse & Sauval (1998). Atomic diffusion in MESA uses the Burgers equations (Burgers, 1969), following the approach of Thoul *et al.* (1994), with radiative accelerations computed using the methods outlined by Hu *et al.* (2011). The effects of radiative levitation make use of the monochromatic opacity data from the Opacity Project (Opacity Project Team, 1995, 1997) and in this work are computed for the isotopes ^{1}H, ^{4}He, ^{12}C, ^{14}N, ^{16}O, ^{20}Ne, ^{24}Mg, ^{40}Ar, ^{52}Cr, ^{56}Fe and ^{58}Ni.

An example low-mass white dwarf progenitor model was constructed starting from a $1\,\mathrm{M}_\odot$ zero-age Main Sequence model. This model evolved to become a white dwarf, with a number of intermediate models saved with a range of helium core mass from $0.18\,\mathrm{M}_\odot$ to $0.38\,\mathrm{M}_\odot$ in steps of $0.005\,\mathrm{M}_\odot$ and $0.38\,\mathrm{M}_\odot$ to $0.46\,\mathrm{M}_\odot$ in steps of $0.01\,\mathrm{M}_\odot$. This encompasses the $0.31\,\mathrm{M}_\odot$ stars found by Pietrukowicz *et al.* (2017) and the objects of $0.28\,\mathrm{M}_\odot$ which appear to reproduce well the observations of Kupfer *et al.* (2019). To replicate the effects of a common-envelope ejection event, each of these models was then stripped of their hydrogen envelope through a large mass-loss rate ($\dot{M} = 10^{-3}\,\mathrm{M}_\odot\,\mathrm{yr}^{-1}$) until a relatively small envelope of approximately $3 \times 10^{-3}\,\mathrm{M}_\odot$ remained. Each of these white dwarf progenitors was then evolved, with the effects of radiative levitation accounted for as long as the effective temperature was greater than $\sim 6\,000\,\mathrm{K}$. Models were allowed to evolve until becoming a white dwarf with a luminosity $\log(\mathrm{L}/\,\mathrm{L}_\odot) = -2$.

Intermediate MESA models were saved every 50 time steps for pulsation analysis. Some models underwent a hydrogen shell flash, these models are discussed further in Section 5.3.

5.2.2 Pulsation Models

The stellar models were analysed for stability using the GYRE stellar oscillation code (Townsend & Teitler, 2013; Townsend *et al.*, 2018). The interim MESA stellar profiles from each evolution track were provided as input to GYRE. An adiabatic analysis is computed first to find the eigenfrequencies of the star. These adiabatic results are then used as the initial guess in a non-adiabatic analysis to determine the stability of the identified modes. As with the models analysed in Byrne & Jeffery (2018), the frequency scan was limited to $\ell = 0$ modes and focused on the fundamental radial mode given that both the prototype BLAPs and the high-gravity counterparts show large amplitude pulsations characteristic of the fundamental mode.

Static envelope models produced by Jeffery & Saio (2016) indicate that the Z-bump instability strip extends over a broader range of surface gravities than seen in hot subdwarf stars. As was the case in Byrne & Jeffery (2018), the blue-edge of the instability strip appears to be located at a higher temperature in the whole star evolutionary models with inhomogeneous envelope compositions than in the static homogeneous envelope calculations of Jeffery & Saio (2016).

5.3 Results

Figure 5.1 shows a representative sample of the evolutionary tracks from the grid. Several behaviour characteristics are noticeable. The most massive objects evolve in a relatively simple manner, getting hotter at constant luminosity, before cooling and contracting. At the lowest masses, they likewise show a straightforward evolution. At intermediate masses ($0.255 \leq \mathrm{M_{core}}/\,\mathrm{M_{\odot}} \leq 0.305$) these models are observed to undergo a late hydrogen shell flash, leading them to complete a 'loop' in the $\log g - \log \mathrm{T_{eff}}$ diagram. This ignition of hydrogen causes expansion of the envelope, which causes the star to become a cool giant once more before returning to the white dwarf cooling sequence once more. These sorts of 'late-hot flashers'

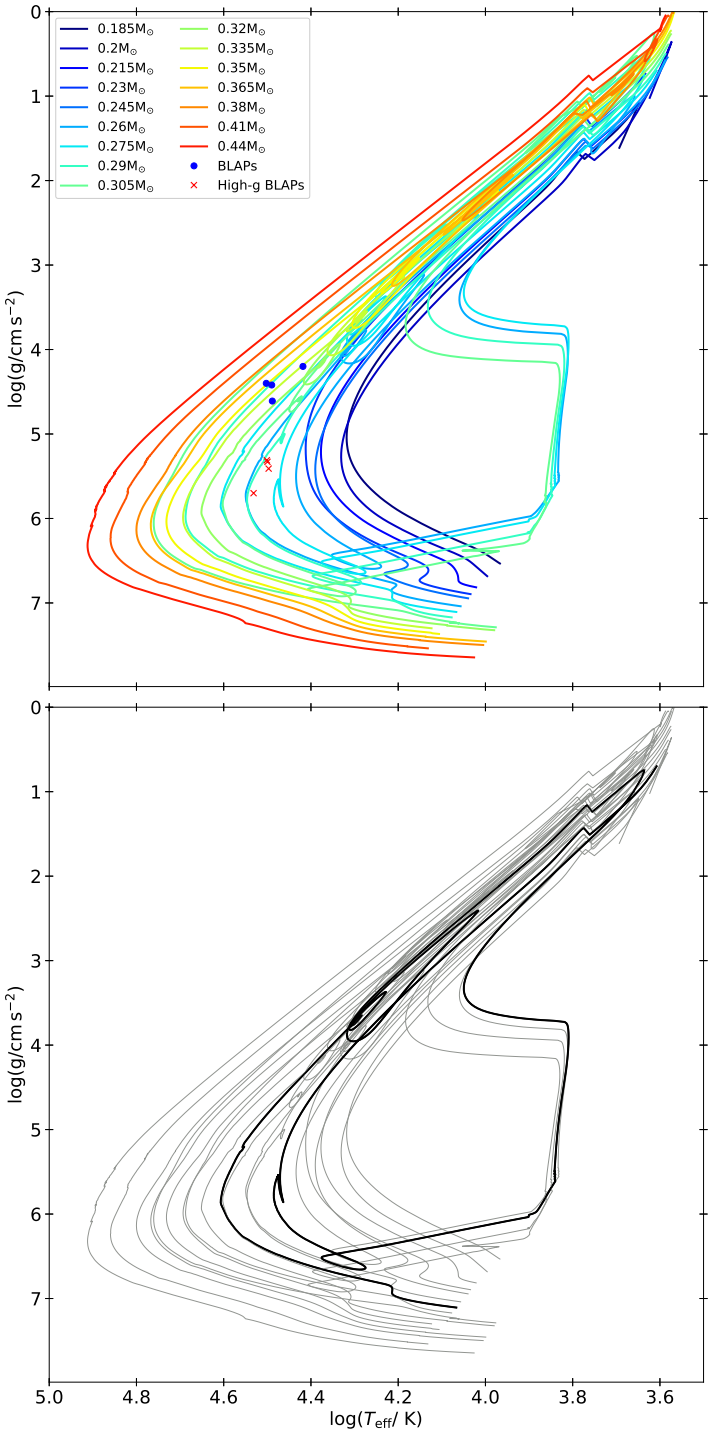

Figure 5.1: Illustrative evolutionary tracks in the log g − log $T_{\rm eff}$ plane of some of the models in the grid. The masses in the legend refer to the core mass. The locations of the low-gravity and high-gravity pulsators are also marked. To aid visibility of the loops in the diagram, the lower panel highlights the evolutionary track of a single model, namely the model with a core mass of 0.275 $M_\odot$ in black, with the other models in grey.

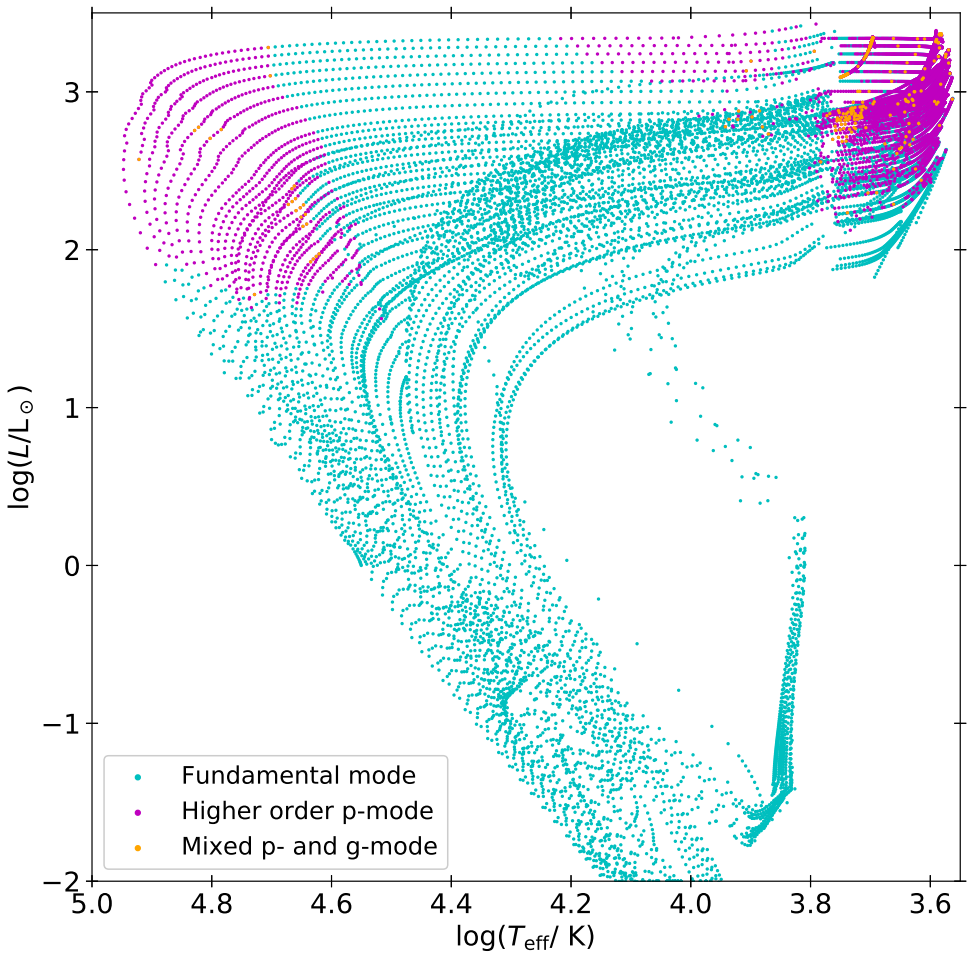

Figure 5.2: Lowest order mode identified by non-adiabatic GYRE analysis. Models where the fundamental radial mode have been identified are shown in cyan. Models where a higher order p-mode is the lowest identified are shown in magenta, while models which purport to have a g-mode component are shown in orange.

are common in low mass pre-WDs and hot subdwarfs (Brown *et al.*, 2001; Miller Bertolami *et al.*, 2008). Overall the evolutionary tracks are in good agreement with those shown in Fig. 1 of Istrate *et al.* (2014). The 'kink' features in the cooling tracks of some of the models ($\log \mathrm{T_{eff}} \sim 4.1$–$4.3$, $\log g/\mathrm{cm\,s^{-2}} \sim 6.5$) are similar to that noted in Driebe *et al.* (1998), where they are identified to be models which transition to unstable hydrogen burning, but where the heat is able to escape sufficiently quickly to not go through a complete hydrogen shell flash.

5.3.1 Mode Identification

Each intermediate MESA model in every evolutionary sequence was analysed non-adiabatically using GYRE to examine the pulsation properties of the stars as they evolve from the red giant branch to the white dwarf cooling track. The initial adiabatic analysis carried out by GYRE typically finds a monotonically increasing sequence of modes, starting at $n_p = 1$ (the radial fundamental mode). The subsequent non-adiabatic analysis, which takes the adiabatic solutions as initial guesses to solve the non-adiabatic case generally finds the same modes of pulsation. In some situations, this is not true, with the non-adiabatic GYRE analysis not finding the $n = 1$ mode, and in some extreme cases, the lowest order mode it identifies claims to be a p-mode mixed with a g-mode component. This is illustrated in Figure 5.2, which shows the lowest order mode found by the non-adiabatic GYRE study. Note that this plot does not indicate the stability/instability of any model, it simply indicates the mode order of the first identified mode. The cyan symbols show the models where the fundamental mode is identified, the magenta symbols show models where a higher order radial mode is the first identified, while the orange symbols indicated models where the mode identified contains a g-mode component. There are three main regimes in which the fundamental mode is not identified. These are $\log \mathrm{T_{eff}} > 4.6$, $3.85 \leq \log \mathrm{T_{eff}} \leq 4.2$ and $3.6 \leq \log \mathrm{T_{eff}} \leq 3.75$, which are a result of highly non-adiabatic conditions associated with enhanced Fe opacity for the first two, and H and He opacity for the latter. The models which GYRE has attributed some g-mode characteristic constitute a relatively small fraction of the models and this has been attributed to numerical noise as a consequence of the highly non-adiabatic conditions in some

of the models. This is a logical conclusion as radial modes, which are not related to buoyancy, should not couple to g-modes (Saio, H., priv. comm.).

5.3.2 Pulsation Analysis

Figure 5.3 plots each individual stellar model on the $\log g - \log T_{\rm eff}$ plane (left panel) and the $\log P - \log T_{\rm eff}$ plane (right panel) and indicates the stability of the lowest order mode identified in the frequency scan of the uniform-in-frequency grid. This grid was chosen as it is best suited to identifying p-modes. There are a number of points of interest in this diagram.

- At low temperature and gravity ($T_{\rm eff} \lesssim 5000\,{\rm K}$, $\log g/{\rm cm\,s^{-2}} \lesssim 2.0$), all the models show instability. The opacity profile of a representative model chosen from this region ($M_{\rm core} = 0.3\,M_\odot$, $T_{\rm eff} = 4400\,{\rm K}$, $\log g/{\rm cm\,s^{-2}} = 0.43$) is shown in Figure 5.4 along with the value of dW/dx, the derivative of the work function for the fundamental mode identified by the non-adiabatic pulsation analysis. The result shows the peak in the driving is located at an effective temperature of 10 000 K, suggesting it could be the result of the H I-II and He I-II partial ionisation opacity bump, also believed to be at least partly responsible for the pulsations in Mira variables (Ostlie & Cox, 1986). It must however be noted that the coupling between pulsation and convection is not considered by GYRE and therefore the nature of these pulsations cannot be deduced with certainty.

- At the highest luminosities (the uppermost diagonal in the $\log g - \log T_{\rm eff}$ plane) the models are also unstable. This can be attributed to strange-mode pulsation due to the highly non-adiabatic nature of these stars, which have a high L/M ratio, close to the Eddington limit.

- Models completing their 'loop' in the diagram are found to be unstable at $\log T_{\rm eff}/{\rm K} < 4.0$, $4.0 \leq \log g/{\rm cm\,s^{-2}} \leq 6.0$ as they re-ascend to the low temperature, high luminosity regime. This phase of evolution is characterised by a significant increase in radius over a relatively short period of time. An example driving/opacity diagram for one of these objects is shown in Figure 5.5. It can be seen that dW/dx is extremely noisy and

the magnitude of the work function is much lower than that seen in Figure 5.4. The likely cause of the instability in this case is the ϵ-mechanism (pulsations driven by changes in nuclear burning rates), as a consequence of the sudden short-lived increase in nuclear burning associated with the shell flash. The $0.3\,M_{\odot}$core model takes 2 000 years to evolve from the onset of the hydrogen shell flash (identifiable by the sudden change to an upward slope in the $\log g - \log T_{\rm eff}$ plane when the model is on the white dwarf cooling sequence) until it reaches the low temperature turning point at the top-right corner of the $\log g - \log T_{\rm eff}$ diagram. Less than 60 years are spent in the portion of the diagram where the star evolves from high surface gravity ($\log g/\mathrm{cm\,s^{-2}} \approx 6$) to lower surface gravity ($\log g/\mathrm{cm\,s^{-2}} \approx 4$) at near constant temperature ($\log T_{\rm eff} \approx 3.85$). This makes it clear that a 1D hydrostatic model of this star is not an appropriate treatment in this phase of evolution and therefore no conclusions should be made about the stability status of the star.

- Some regions of instability are noted in the white dwarf cooling tracks. These appear most prominent between $4.5 \leq \log T_{\rm eff}/\mathrm{K} \leq 4.6$ and approximately $4.1 \leq \log T_{\rm eff}/\mathrm{K} \leq 4.3$, which are in reasonable agreement with the temperature ranges of 'hot-DAV' (Shibahashi, 2005) and DAV (Landolt, 1968) white dwarfs respectively. This seems like a reasonable result as all these models have hydrogen rich envelopes in this evolutionary phase as gravitational settling dominates the atomic diffusion process, leaving mostly hydrogen at the surface.

- A large region of instability is present between 25 000 K and 80 000 K. This is the instability region caused by the iron opacity bump, and is the identified driving mechanism for at least the 'low-gravity' BLAPs (Byrne & Jeffery, 2018). This instability region is the primary focus of this work.

- This high effective temperature region also includes an apparent 'island of stability' for surface gravities $\log g/\mathrm{cm\,s^{-2}} < 6$. As discussed in Section 5.3.1 above, this portion of the diagram is where GYRE has had issues

in its non-adiabatic analysis. As a result the lowest order mode identified is not always the radial fundamental mode, but higher order p-modes. Therefore the results in this region are incomplete, as the stability of the fundamental mode remains undetermined. This is illustrated in Figure 5.6 where the $\log g - \log T_{\rm eff}$ diagram is reproduced, but with the models with no identified fundamental mode plotted in grey. This makes it difficult to estimate the location of the blue-edge of the instability region, as all the high effective temperature models have inconclusive results. A black box highlights models with $\log T_{\rm eff}/{\rm K} > 4.475$ and $\log g/{\rm cm\,s^{-2}} < 6.2$, where the vast majority of the models appear to be unstable, which is relevant when discussing the lifetime of these objects in Section 5.3.3.

- There is an overlapping region of stable and unstable models at $\log T_{\rm eff} \sim 4.4$, $\log g/{\rm cm\,s^{-2}} \sim 4.7$. This region where seemingly stable and unstable stars can coexist is discussed in greater detail in Section 5.3.4, where the models which undergo a hydrogen shell flash are discussed in more detail.

- The issue with mode identification can also be illustrated in the irregular spacing of the points in the high temperature regime in the $\log P - \log T_{\rm eff}$ plane shown in the lower panel of Figure 5.3 which differs from the more uniform spacing found in the $\log g - \log T_{\rm eff}$ diagram in the upper panel. This is further evidence that the fundamental modes are not always being found as the fundamental period should scale via the period-mean density relationship, which scales with radius for a fixed mass, while the surface gravity also scales with radius, so both plots should be similar if the fundamental mode was identified each and every time.

5.3.3 The Faint Blue Variable Instability Region

This large instability region encompasses both the low-gravity and the high-gravity BLAPs, as well as a broader region of temperatures and gravities. Figure 5.7 illustrates the effects of radiative levitation on the evolution of the models. As in the previous figures, the models are placed on the $\log g - \log T_{\rm eff}$ diagram. In this instance, the points are colour-coded to indicate the logarithmic value of

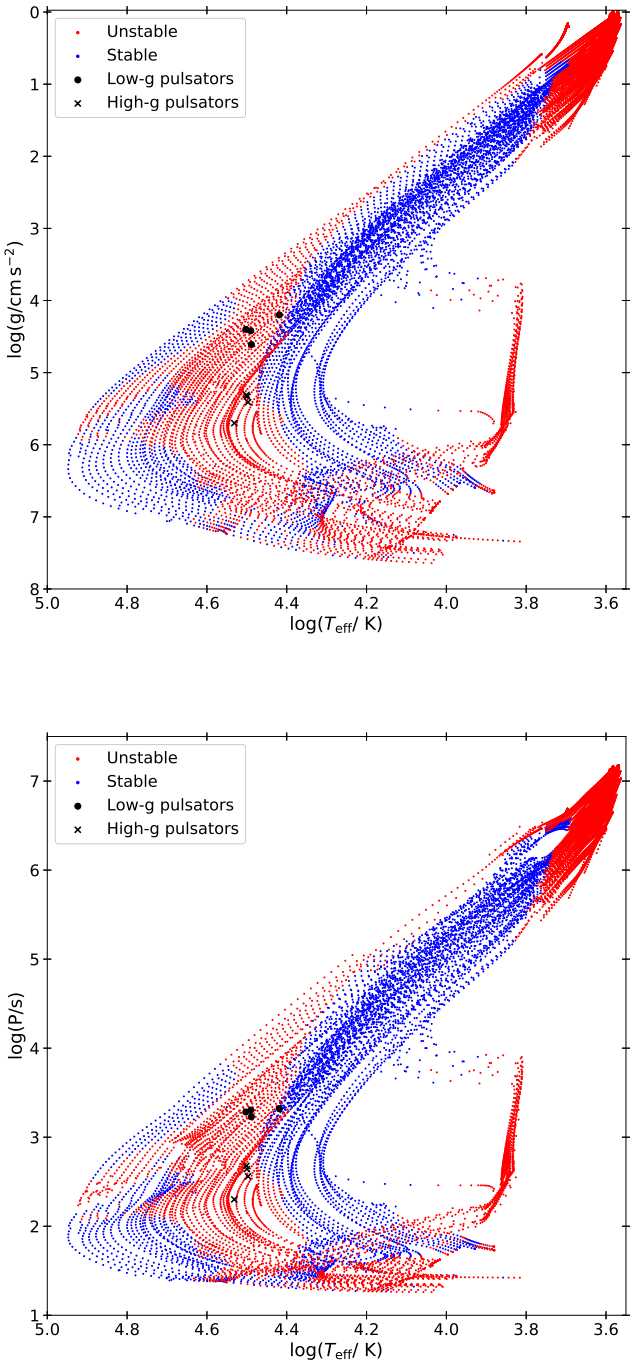

Figure 5.3: *Upper panel:* The log g − log $T_{\rm eff}$ plane showing the pulsation stability of the calculated models. Models where the lowest-order mode to be identified is unstable are shown in red, while those which are stable are shown in blue. The location of the Pietrukowicz *et al.* (2017) and Kupfer *et al.* (2019) variables are also indicated. *Lower panel:* As above, but with the logarithm of the pulsation period of the lowest order mode in seconds plotted on the y-axis.

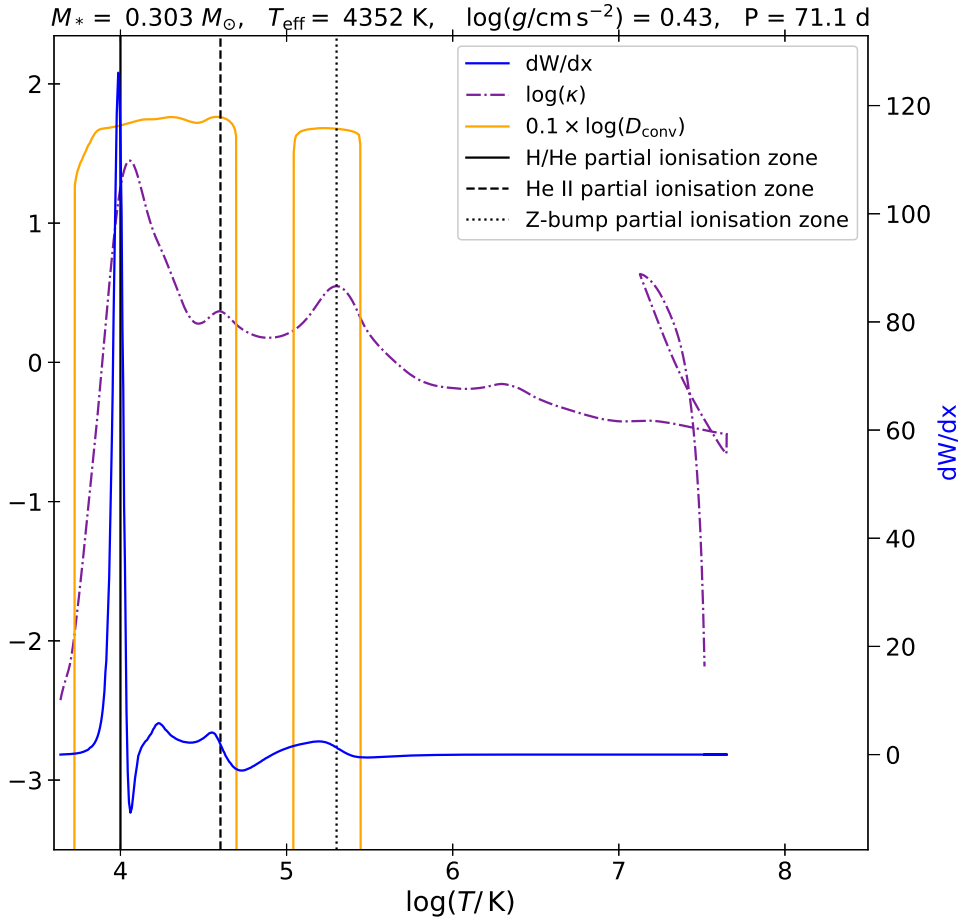

Figure 5.4: Profile of opacity, convective regions and work function derivative of the fundamental mode as a function of stellar interior temperature. The logarithm of the opacity is shown by dot-dashed purple line, the logarithm of the convective velocity (scaled down by a factor of 10) is indicated by the solid orange line, while the value of dW/dx is indicated by the solid blue line. Note that the magnitude of dW/dx is indicated on the right-hand axis, unlike the other variables. The vertical solid, dashed and dotted lines indicate the approximate temperatures of the partial ionisation opacity peaks of H/He, HeII and iron group elements respectively. Note that there is a temperature inversion and hence the variables are double-valued for values of $\log T > 7$.

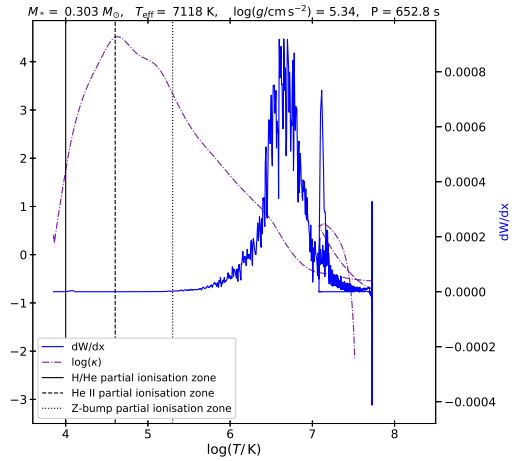

Figure 5.5: As in Figure 5.4, but for a model in the post-hydrogen shell flash evolutionary state. Again, note that there is a temperature inversion and hence the variables are double-valued for values of $\log T > 7$.

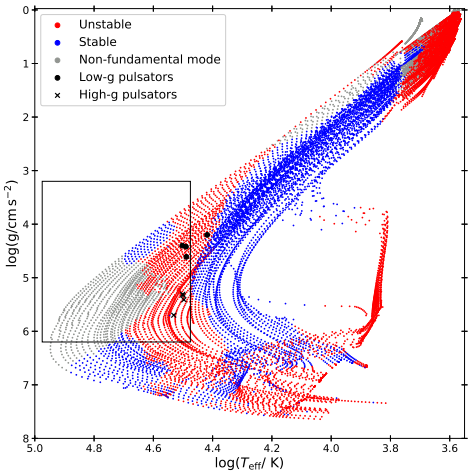

Figure 5.6: As in Figure 5.3, except the models for which the fundamental mode was not identified are plotted in grey. The black box indicates the portion of the instability region which is discussed in more detail in Section 5.3.3.

the mass fraction of ^{56}Fe present in the region of maximum opacity ($\sim 2 \times 10^5$ K), with the purple colour at the lower end of the scale corresponding to the solar value, $\log(X_{\rm Fe}) = -3$. The models where the lowest order mode to be identified is found to be stable are indicated by open symbols. Models where the lowest ordered mode identified is found to be unstable are indicated by the filled symbols. In general, this refers to the radial fundamental mode, except in the cases highlighted in Figure 5.2, where only higher order p-modes are successfully identified. The bulk of the instability region coincides well with the iron opacity reaching its maximal value. This reinforces the result that radiative levitation of iron and nickel is the key mechanism leading to the presence of pulsations in these stars. Figure 5.8 illustrates this for 2 example models. The upper panel shows a $M_{\rm core} = 0.325\,M_\odot$ model with an effective temperature of 30 600 K and a surface gravity of 4.6, which closely matches that of OGLE-BLAP-001 while the lower panel shows a $M_{\rm core} = 0.285\,M_\odot$ model with an effective temperature of 31 700 K and a surface gravity of 5.4, closely resembling the properties of HG-BLAP-2. In both cases, it can be seen that the peak of the driving (indicated by the maximum of the derivative of the work function) corresponds to the location of the peak in the iron abundance and corresponding opacity bump. This confirms that the driving mechanism for both the low-gravity BLAPs of Pietrukowicz *et al.* (2017) and the high-gravity BLAPs of Kupfer *et al.* (2019) is the κ-mechanism, with the opacity bump enhanced by the action of radiative levitation on iron and nickel.

The high temperature instability region in Figure 5.3 is a lot more extended than the region occupied by the objects which have so far been identified on the $\log g - \log T_{\rm eff}$ diagram. As a rough estimate, the instability region roughly extends from when the star exceeds a temperature of around 30 000 K ($\log T_{\rm eff} = 4.475$) and until it moves across at high luminosity to its maximum temperature and then until it contracts to have a surface gravity of ($\log g/{\rm cm\,s^{-2}} \sim 6.2$). This is indicated by the rectangle in Figure 5.6. Considering only those models in which the fundamental mode has been identified, a majority of the models in this region are unstable. Therefore the time spent in this portion of the $\log g - \log T_{\rm eff}$ plane can be used as a rough indication of the lifetime of the pulsator.The stability of the models at the highest temperatures remains unclear. However, given the fact that Figure 5.3 shows that some higher order p-modes show instability, it is not

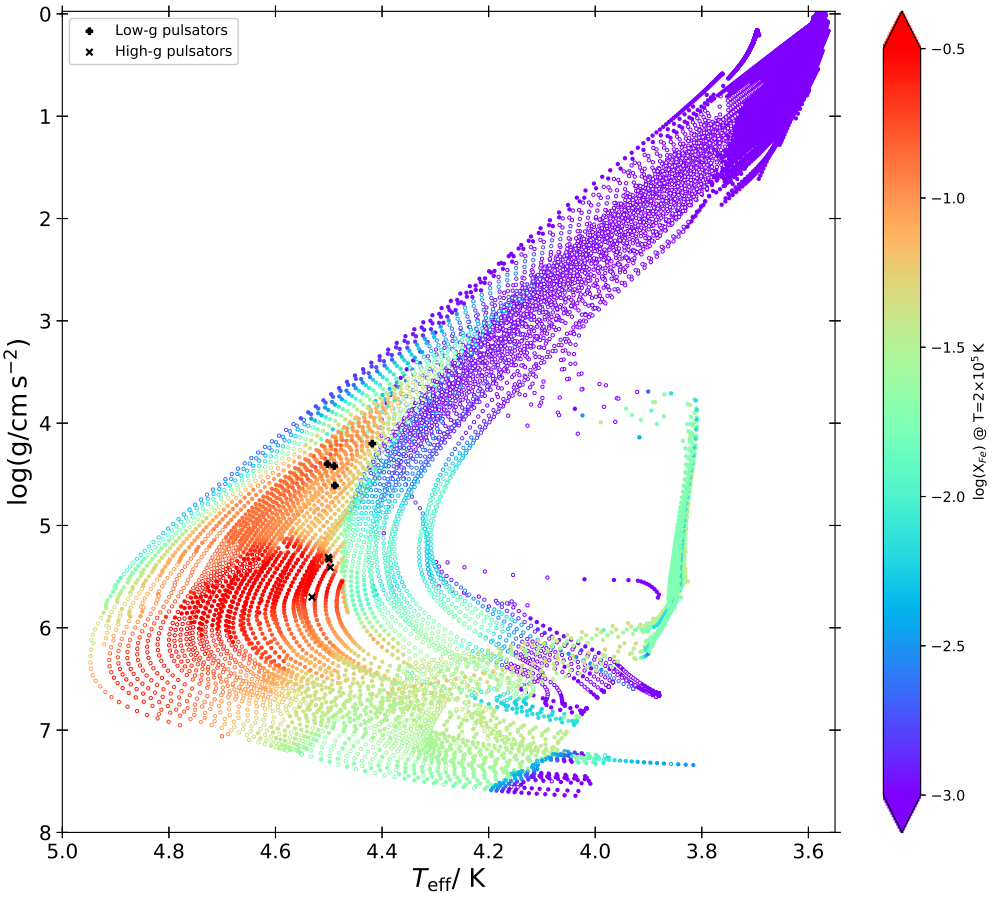

Figure 5.7: log g − log $T_{\rm eff}$ diagram showing the mass fraction of iron present in the iron opacity bump around T=2×10^5 K. Filled symbols indicate models with an unstable fundamental mode, while the open symbols indicate models with a stable fundamental mode. The location of the Pietrukowicz *et al.* (2017) and Kupfer *et al.* (2019) variables are also indicated.

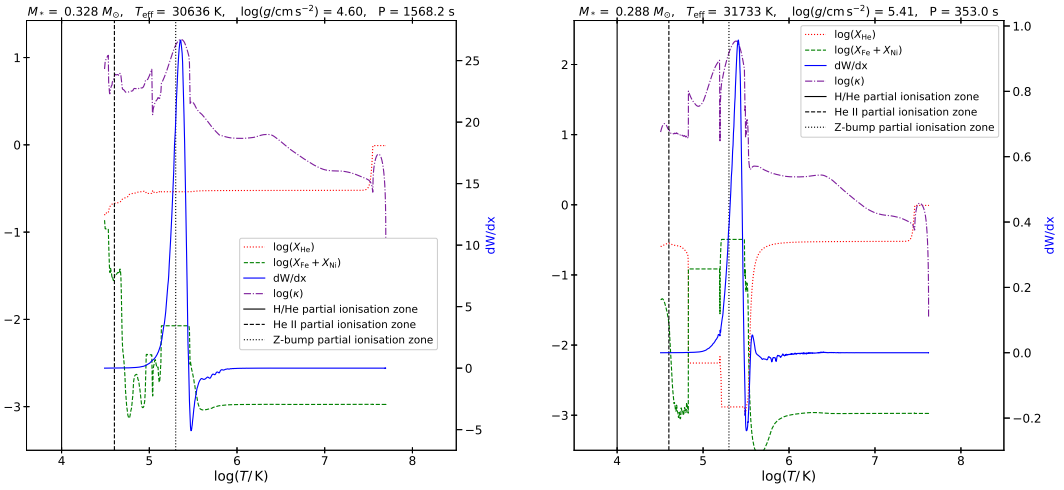

Figure 5.8: As in Figure 5.4, but for models closely resembling OGLE-BLAP-0001 (upper panel) and HG-BLAP-2 (lower panel). Additionally, the logarithm of the combined mass fraction of Fe and Ni, the mass fraction of He are shown by the dashed green and dotted red lines respectively.

unreasonable to assume these stars are unstable for some portion of their evolution through this region. Some stars are unstable at cooler temperatures and/or higher surface gravities, but this provides a conservative estimate on where these stars could be expected to be unstable. Figure 5.9 illustrates the time that each model spends in this portion of the $\log g - \log \mathrm{T_{eff}}$ plane as a function of core mass. The blue squares indicate the time spent in this region of the $\log g - \log \mathrm{T_{eff}}$ diagram on a logarithmic scale. The green histogram represents the mass distribution per unit time spent in the specified region of parameter space, binned into mass increments of $0.015\,\mathrm{M_\odot}$. That is to say, the cumulative lifetime of the models in the area of interest is normalised such that the sum of heights of the bars in the histogram is equal to 1. This provides insight into the range of masses of objects likely to be observed in this faint blue star instability region based on the argument of evolutionary timescales, assuming a uniform proto-WD mass distribution.

This illustrates that there is an optimal range of masses in which these objects are reasonably long lived. The longest lived model in this region is the $\mathrm{M_{core}} = 0.275\,\mathrm{M_\odot}$ model, with models with core masses between $0.255\,\mathrm{M_\odot}$ and

$0.310\,M_\odot$ all having a 'lifetime' of 10^6 yr, with stars with core masses greater than $0.310\,M_\odot$ having a logarithmically decreasing lifetime as they evolve much faster from the post-CEE phase to becoming a white dwarf. Stars with core masses below $0.255\,M_\odot$ don't exceed the required temperature cutoff and are not unstable in any case, so pulsating pre-WDs are not expected for masses below this. From the histogram, it can be seen that 45 per cent of the cumulative lifetime of objects is contained in the mass range $0.2705 \leq M_*/M_\odot \leq 0.3005$, while almost 75 per cent of the cumulative lifetime is located in the mass range $0.2555 \leq M_*/M_\odot \leq 0.3155$, with the remaining 25 per cent found at higher masses.

5.3.4 Shell Flash Models

A number of models in this work are found to undergo a hydrogen shell flash in their post-common-envelope evolution. For the envelope mass used in this work ($3 \times 10^{-3}\,M_\odot$), this corresponds to models with a helium core mass between $0.255\,M_\odot$ and $0.305\,M_\odot$. To examine the effects that this flash has on the pulsation stability of the models, these models were isolated and separated into their pre-flash and post-flash loops. This is illustrated in the panels of Figure 5.10. The upper left panel shows both loops of these 'flasher' models in distinct colours, with the first loop in yellow (cyan) and the second loop in magenta (green) for stable (unstable) models. The remaining models are plotted in grey, with dark grey used to indicate the unstable models. The first loop and second loop are then plotted individually in the upper right and lower left panels respectively.

In the first loop, the low temperature instability region driven by the H/He partial ionisation opacity and the high temperature instability region driven by Z-bump opacity are both present and the extent of the instability is generally in agreement with the adjacent non-flasher models. A curious overlap region is observed at $\log T_{\rm eff} \approx 4.45$ where it appears that stable and unstable models should be able to co-exist. An expanded plot of this region is shown in Figure 5.11, with evolutionary tracks for clarity. In these tracks, a 'hook' or 'mini-loop' feature is evident, with models from before the hook/mini-loop generally being stable, and only becoming unstable while evolving through the hook/mini-loop. This

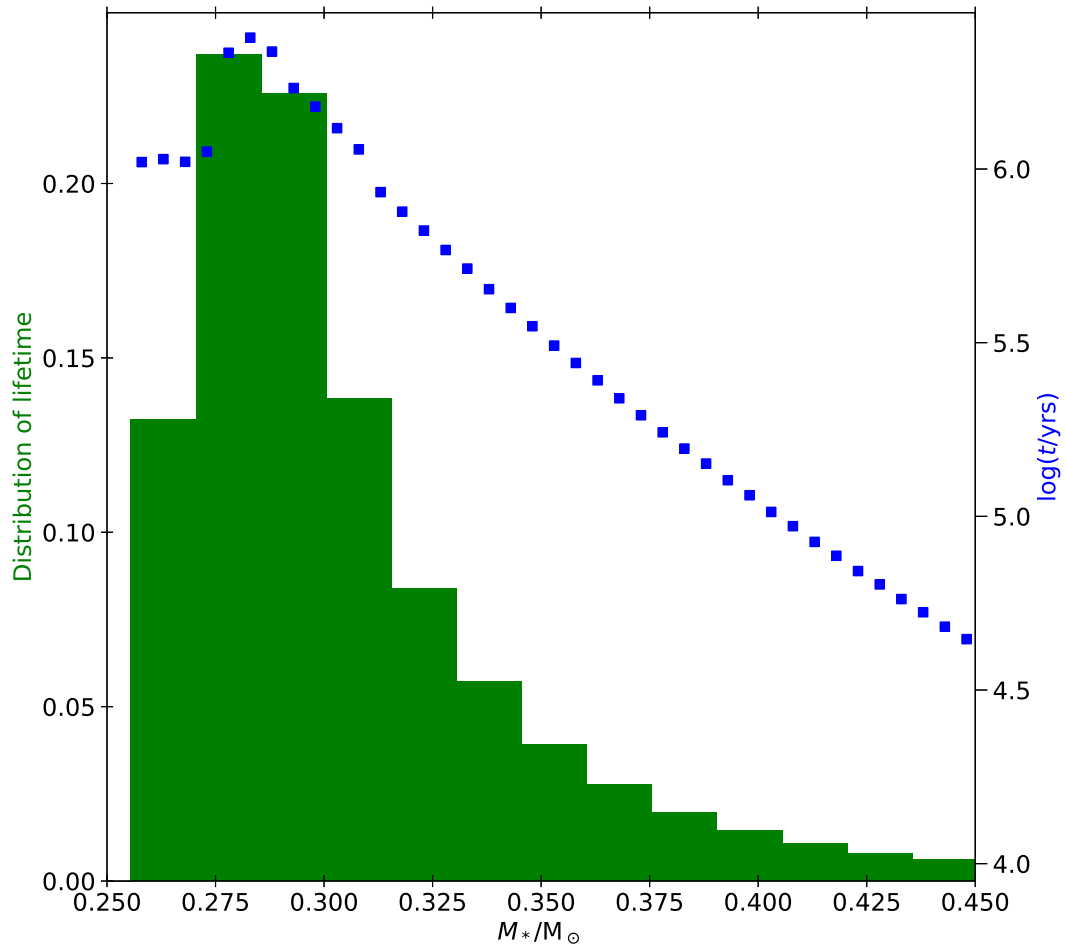

Figure 5.9: Lifetime of potential pulsators in the faint blue star instability region ($\log T_{\rm eff} \gtrsim 4.475$, $\log g/{\rm cm\,s^{-2}} \lesssim 6.2$) as a function of mass. The blue dots indicate the logarithm of the time spent in this region. For models which undergo a hydrogen shell flash, the combined total time spent in this region during both visits to this area is the value plotted. The green histogram shows the normalised distribution of time spent in this region as a function of mass.

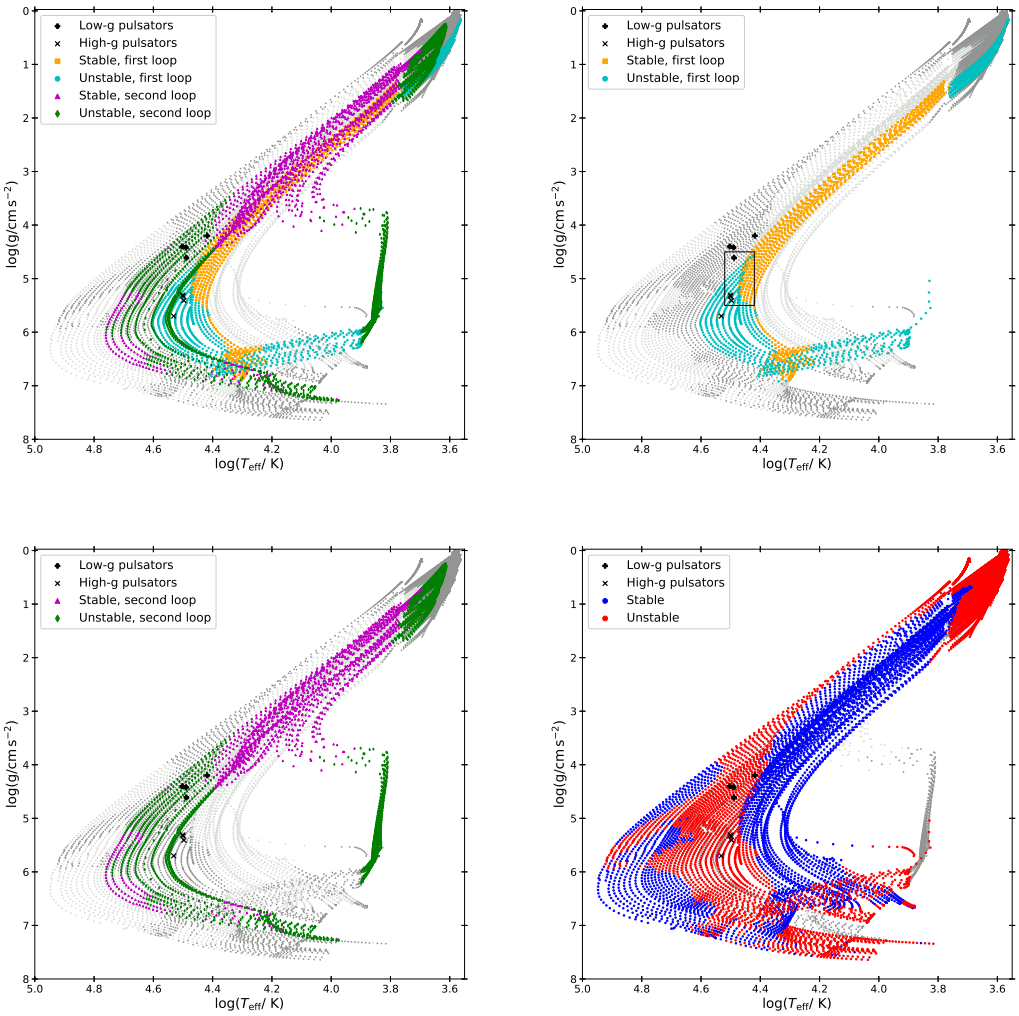

Figure 5.10: Stability diagram in the log $g-$ log $T_{\rm eff}$ plane showing the difference in behaviour between the 'flasher' models and the non-flashing models. *Upper left*: Only the models with core masses between 0.255 $M_\odot$ and 0.305 $M_\odot$ which are observed to undergo a late hydrogen shell flash are coloured. The models are shown as yellow diamonds (cyan circles) when stable (unstable) on their first loop and as purple triangles (green diamonds) when stable (unstable) on their second loop. The other stable (unstable) models are shown in light grey (dark grey). *Upper right*: Only the first loop of the 'flasher' models are coloured, with the same choice of colours as in the first panel. The black rectangle indicates the area which is enlarged and shown in more detail in Figure 5.11. *Lower left*: Only the second loop of the 'flasher' models are coloured, with the same choice of colours as in the first panel. *Lower right*: All models are plotted, using the same colour scheme as Figure 5.3, but the second loop of the flasher has been left in grey. The location of the Pietrukowicz *et al.* (2017) and Kupfer *et al.* (2019) variables are also indicated as black squares and black crosses respectively in each panel.

hook is a result of the transition from envelope contraction following the post-common-envelope phase to the onset of a period of hydrogen shell burning once the envelope reaches the necessary conditions for shell burning to resume. The initial contraction phase is rather rapid, while the hydrogen burning phase is somewhat slower until it too is exhausted and the white dwarf contraction phase begins. For example, the $0.305\,M_{\odot}$ core model (shown by the black line in Figure 5.11) takes $\sim 10^3$ yr to evolve from the post-common-envelope phase to the beginning of the loop, while taking $\sim 10^5$ yr to evolve through the loop. This rapid evolution prior to the loop is not sufficiently long relative to the diffusion timescale to allow iron and nickel to accumulate and therefore the star remains stable. Once they reach the hook/loop, the following phase of evolution is much slower, allowing the heavy metals to accumulate and pulsations are driven. The apparent overlap is due to the shape of these loops, whereby the models initially move to high effective temperature, before cooling slightly during the loop, and then becoming unstable, thus giving the appearance that some models which are slightly hotter are stable unlike their slightly cooler counterparts. Another interesting observation in this diagram is that a number of the pulsators sit quite close to this point in the evolutionary tracks, shortly after the onset of radiative levitation.

For the second loop, both of the main regions of instability, the low temperature and the high temperature regions, are in broad agreement with the rest of the overall population. The evolution of these objects after their flash is at a significantly higher luminosity and reaches a higher maximum temperature than achieved on their first loop.

5.3.5 Effects of Envelope Mass

The presence of shell flashes in some of the models is the result of the remnant hydrogen envelope. Therefore it is instructive to construct further models to investigate the effects of a smaller or larger hydrogen envelope on these results. This is an important area of investigation as the amount of material removed from a star in the common-envelope ejection scenario remains largely uncertain (see, for example a review of this topic by Ivanova *et al.*, 2013). To gauge this,

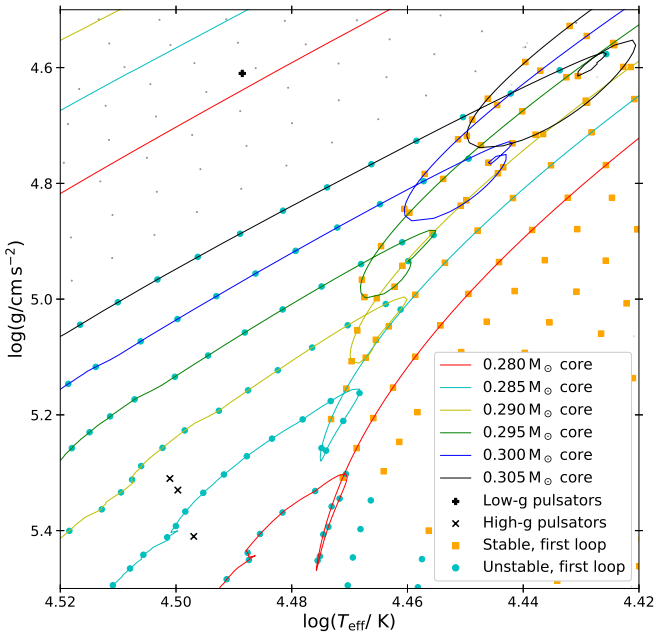

Figure 5.11: A close-up view of the highlighted rectangle of Figure 5.10, focusing on the region with overlapping stable and unstable models. To assist with clarity, the evolutionary tracks of some of the models are also drawn.

a smaller envelope mass model ($2 \times 10^{-3}\,M_\odot$) and a larger envelope mass model ($1 \times 10^{-2}\,M_\odot$) were computed for a $0.31\,M_\odot$ core model. The evolutionary tracks and the corresponding stability of the fundamental or lowest order radial mode in each model are shown in Figure 5.12.

For a smaller envelope mass, indicated by the green and magenta symbols, the model also undergoes a hydrogen shell flash. This indicates that envelope mass plays a key role in determining whether a model will have a shell flash or not, as the $3 \times 10^{-3}\,M_\odot$ envelopes primarily used in this study only lead to flashes in models with core masses up to $0.305\,M_\odot$. Additionally, this model has its 'hook' at a much higher effective temperature than the models shown in Figure 5.11, but the same principles observed in those models apply here, namely that the model remains stable during the fast contraction phase and only becomes unstable once reaching the 'hook'. Apart from these differences, the instability of this model is in reasonable agreement with the instabilities of the $3 \times 10^{-3}\,M_\odot$ envelope model and the complete set of models at large.

This significant difference in the temperature at which the hook is located is an interesting feature of the change in envelope mass, with the inference that smaller envelope masses will lead to hooks at higher temperatures. As a result, it is possible that the red edge of the instability region could provide a diagnostic by which it could determine the minimum envelope mass of a pulsator. This could help provide an indirect means of testing the physics of the common envelope phase of evolution.

For a larger envelope mass, the model evolves in a relatively similar way to the $3 \times 10^{-3}\,M_\odot$ envelope model, with a similar behaviour regarding its stability. The larger envelope mass means the model is able to sustain hydrogen shell burning in the aftermath of the common-envelope ejection, thus the star does not go through a hook/loop in its subsequent evolution. In this case, the model begins to be unstable once it reaches a high enough temperature for radiative levitation to become an effective process and has a post-common-envelope age sufficiently long compared to the diffusion timescale for iron to begin accumulating in the Z-bump.

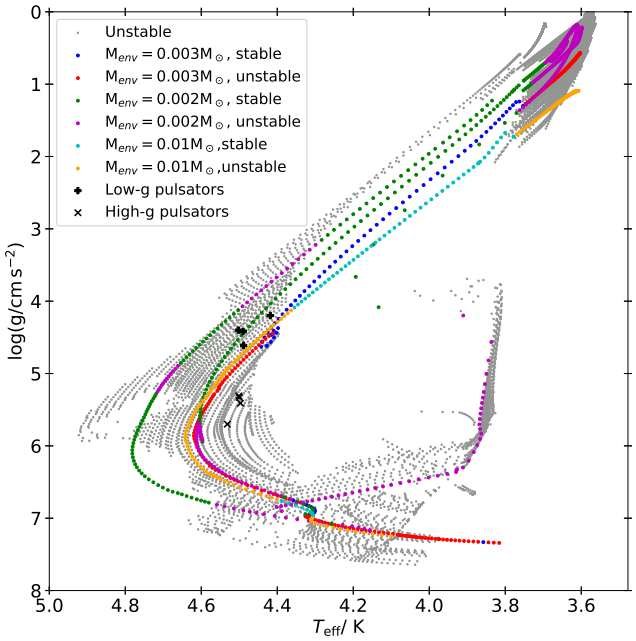

Figure 5.12: A $\log g - \log T_{eff}$ showing the stability of an evolutionary model with a core mass of $0.310\,M_\odot$ and varying envelope mass. The unstable models from the entire dataset of models with $3 \times 10^{-3}\,M_\odot$ envelopes from earlier figures are shown in grey for reference.

5.3.6 Other Potential Effects

There are a number of other areas with unstable models in this data, such as in the white dwarf cooling sequence. As the primary goal of this work was to investigate the population of high amplitude pulsators of Pietrukowicz *et al.* (2017) and Kupfer *et al.* (2019), these models were not investigated in detail in this work. Additionally, as was demonstrated by changing the envelope mass, there are a number of other variables which may play a role and have an impact on the exact morphology of the instability regions. Such analysis and computation is beyond the scope of this work, but will be explored in a subsequent study. These additional effects include, but are not limited to, the method of mass loss (stable Roche lobe overflow rather than common-envelope ejection) and the initial progenitor mass. Another important factor which has not been considered in this work is the mass distribution of low-mass white dwarfs expected from population synthesis calculations. This, combined with the lifetime estimates given in Figure 5.9 would help refine the mass range in which such objects might be detectable. It is also worth emphasising that the results presented here refer to the fundamental mode as much as was physically possible. In principle, this means that the stability of these models in higher order modes and in non-radial modes has not been examined.

5.4 Discussion

In the case of hot subdwarfs, it is known that not all stars in the appropriate temperature range are seen to be pulsators. About 10 per cent of subdwarfs in the sdBVr instability region are observed to pulsate (Østensen *et al.*, 2010), while 75 per cent of stars in the sdbVs instability region are observed to be variable (Green *et al.*, 2003). It is unclear from this work how pure the proto-WD instability region explored in this work could be expected to be.

As this region overlaps with the hot subdwarf instability strip it is worth asking whether it is possible for objects to have been misidentified. From currently existing observations, it would appear that the amplitudes of the pre-white dwarf pulsators are considerably larger than those of the highest amplitude subdwarfs.

However, moving forward it would be instructive to bear in mind that there may be two overlapping populations of objects in this part of the Hertzsprung–Russell diagram.

5.4.1 Nomenclature

As the population of these hot, subluminous variable stars grows, both in number and in extent in the $\log g - \log T_{\rm eff}$ plane, there is potentially some merit to discussing a coherent and descriptive naming system for these stars, as it is evident that intermediate mass/gravity objects have the potential to exist, leading to a breakdown in the dichotomy of 'high-gravity' and 'low-gravity' BLAPs. While their temperatures and brightnesses place them close to hot subdwarf variables, these stars are fundamentally different (shell-hydrogen burning, rather than the hot subdwarfs which are core-helium burning objects). Another potential naming convention would be to describe them as 'Faint Blue Variables', as an analogue to luminous blue variables, which also show dramatic changes in brightness. Given that the variability of the luminous blue variables is an unpredictable rather than periodic variations, this name would likely cause confusion also. What is evident at this point is that all of these stars are blue, subluminous and exhibit radial mode pulsations. Perhaps a name such as faint-blue radial pulsators would be a more appropriate descriptor of this new and growing class of pulsating star.

5.4.2 Completeness of Population

With the growing number of BLAPs being discovered, it becomes crucial to carry out spectroscopic analysis of as many such stars as possible So far, only 4 of the 14 OGLE pulsators have had effective temperatures and surface gravities determined spectroscopically. Locating these objects on the $\log g - \log T_{\rm eff}$ diagram and comparing to the stability diagrams produced in this work will enable a broader understanding of this new class of pulsator. With continuing and new high-cadence photometric surveys, it is inevitable that more such stars will be discovered in the future. These must be combined with distances (e.g. Ramsay, 2018) to construct volume-limited samples and hence to test stellar evolution and binary population synthesis models for pre-white dwarfs.

5.4.3 Relation to EL CVn Stars

From the orbital parameters of the currently known EL CVn systems (see Section 1.8), Chen *et al.* (2017) show that the formation of the low-mass pre-white dwarfs in those systems cannot come from the common envelope channel as systems with a red giant with such a low core mass would lead to a merger rather than a common envelope and subsequent binary system. As discussed in Section 5.3.6 above, the Roche lobe overflow evolution channel and the effects it may have on the instability regions have not been explored in this work and remain an area for future study.

5.4.4 Binarity

Following the implication that these pre-white dwarf variables are products of binary evolution, it would be expected that some, if not all, of the observed pulsators should show evidence of binarity. Currently none have shown any such evidence and further observations are needed to test this expectation. If any of the observed pulsators are descendants of EL CVn stars, an A- or F-type main-sequence star companion should be visible in the spectrum and at least some should still be eclipsing, despite the smaller radius of the contracting pre-white dwarf. No signatures of eclipse have been found. In the case of post-common-envelope pre-white dwarfs with compact companions such as the Gianninas *et al.* (2016) pulsators, evidence should be sought from radial-velocity studies extending over both the pulsation and putative orbital periods.

5.4.5 Extent of the Instability Region

The blue-edge of the instability region remains uncertain owing to the current lack of data on the fundamental mode in the models. For the assumed envelope mass ($3 \times 10^{-3}\,\mathrm{M}_{\odot}$), the red-edge is reasonably well defined, with almost all models above 30 000 K showing instability, with the red-edge dropping to about 25 000 K for the models with the highest and the lowest surface gravities. From the lower panel in Figure 5.3, this corresponds to pulsation periods from ~ 100 s as the models approach the white dwarf cooling sequence up to $\sim 10\,000$ s (2.8 hr) for the more massive models as they contract at high luminosity. The red-edge

is sensitive to the assumed envelope mass, and this should be explored in more detail in future.

5.5 Conclusions

Evolutionary models of low mass pre-white dwarfs including the effects of radiative levitation have provided tremendous insight into the regime in which a new and growing population of faint blue pulsating star has been discovered. A large region of the $\log g/\mathrm{cm\,s^{-2}} - \log \mathrm{T_{eff}}$ diagram shows instability of the radial fundamental mode from effective temperatures around 30 000 K, up to at least 50 000 K and potentially up to 80 000 K. In this temperature range, the periods of the unstable fundamental modes range from around 100 seconds up to 2-3 hours at the longest durations.

The driving mechanism is clearly identified as the κ-mechanism as a result of a large Z-bump opacity as a direct consequence of radiative levitation, with the significant enhancement of heavy metal opacity providing a strong driving force. This region of instability includes both the low-gravity variables discovered by Pietrukowicz *et al.* (2017) and their high-gravity counterparts discovered by Kupfer *et al.* (2019). This confirms that both of these groups of stars are part of the same phenomenon, that is that they are all pulsating pre-low mass white dwarf stars. The location of the instability region coincides remarkably well with the onset of radiative levitation, illustrating the importance of the increase in iron abundance in the Z-bump opacity peak for pulsation driving.

Assuming a flat initial mass function for pre-WDs, over 75 per cent of the cumulative time within the instability zone is spent by stars with mass $0.2555 \leq \mathrm{M_*/\,M_\odot} \leq 0.3155$. Higher mass models evolve faster. Models with masses less than $0.255\,\mathrm{M_\odot}$ do not reach high enough effective temperatures for radiative levitation to become efficient enough to lead to pulsations. Models with core masses between $0.255\,\mathrm{M_\odot}$ and $0.305\,\mathrm{M_\odot}$ undergo a hydrogen shell flash. Closer examination of these models shows that their post-common envelope evolution is characterised by a quick increase in effective temperature as their inert hydrogen envelope remnant contracts, followed by a hook/loop as hydrogen-shell burning resumes. This leads to evolution on a nuclear timescale which allows enough

time for radiative levitation to take effect and make the stars become unstable. A number of the observed pulsators are located close to this region at the red-edge of the instability region.

Experiments with differing envelope masses showed that in general the shape and extent of the instability region is largely unchanged. At larger envelope masses, the star is more likely to maintain hydrogen shell burning after common-envelope ejection and thus does not show a hook/loop feature when hydrogen re-ignites. For lower envelope masses it was found that the effective temperature of the model is much higher when it resumes hydrogen shell burning, thus shifting the effective red-edge of the instability region to higher temperatures. This suggests that with a larger population of such pulsators, the location of the red-edge may provide a diagnostic for determining the minimum envelope mass of these pre-white dwarfs, thus providing an indirect way of measuring the efficiency of common-envelope ejection at removing mass in close binary situations.

A number of uncertainties remain in our understanding of this new class of pulsating star. The calculation of non-adiabatic eigenfrequencies with GYRE becomes challenging in extremely non-adiabatic models with high L/M ratios and/or large opacity bumps. It is hoped that future development will enable more robust non-adiabatic analysis with GYRE and provide a complete picture of the instability region at the highest effective temperatures. The calculations presented in this chapter successfully interpret BLAPs as likely low-mass pre-white dwarfs. Such stars must be produced from a close binary interaction which strips most of the hydrogen envelope. It therefore remains puzzling that no evidence for a binary companions to any of these pulsators has yet been found, although it must be acknowledged that systematic searches for binarity (through radial velocity variations or other means) have not yet been carried out for either the low-gravity or high-gravity pulsators.

We propose that given that both the high-gravity and low-gravity stars under discussion are probably compact fundamental radial-mode pulsators driven by the same pulsation mechanism and are the same kind of stellar object, it may be worth providing the class of stars with a name that better reflects their properties, such as faint-blue radial pulsators.

6

Conclusions and future work

I have carried out a number of stellar evolution calculations probing the evolution of low-mass stars which have undergone common envelope evolution. These have focused on two categories in particular; $0.46\,M_{\odot}$ stars, which evolve to become hot subdwarfs, and lower mass stars which evolve to become low-mass white dwarfs.

Chapter 3 presented models of the evolution of subdwarf progenitors. These are the first self-consistent simulations of the evolution of a hot subdwarf from a Main Sequence star via the Red Giant Branch and common envelope evolution (replicated via a sudden rapid mass loss event to strip the envelope) through to core helium ignition. This highlighted a number of results. Firstly, it is possible to produce both helium-rich and hydrogen-rich hot subdwarfs through this evolutionary channel, with the timing of the envelope ejection playing a key role in determining the outcome. Models further from the point of helium ignition have a thinner envelope when ignition eventually takes place, leading to a flash-mixed surface rich in helium. This helium-rich phase may be a transient phenomenon as over time, the action of atomic diffusion will cause any remaining hydrogen to rise to the surface. The inclusion of radiative levitation in the calculations produces surface abundances which are qualitatively similar to the observed abundance trends. However, the effects are significantly overestimated indicating the need

for additional mixing processes to counteract the effects of levitation. Alternatively a better treatment of convection in stars may provide a mechanism to achieve this.

Chapter 4 analyses the pulsation stability of the radial fundamental mode in both pre-subdwarf models and $0.31\,M_{\odot}$ pre-white dwarf models. Both the pre-subdwarf and the pre-white dwarf models are found to pulsate in the region of parameter space associated with the newly discovered BLAPs, but the effects of radiative levitation must be considered in order for this to be the case. Inclusion of radiative levitation also reproduces the known result that hot subdwarfs on the horizontal branch can pulsate, a result which is not found if levitation is ignored in the models. Detailed study of the models which lie in the BLAP region finds that the pre-subdwarf models evolve much more quickly through this region compared to the pre-white dwarf models, and thus the pre-white dwarf model is the preferred explanation for what BLAPs are. Analysis of the pulsation modes identifies the driving mechanism is the κ-mechanism as a result of a large iron opacity peak. Comparison with static models with uniformly enhanced metal abundances indicates a blue-edge which is slightly hotter. This is understood to be a consequence of contraction providing additional destabilisation to the star.

Chapter 5 expands upon the work of Chapter 4 to address the growing number of BLAP discoveries. An expanded set of pre-white dwarf models provide a detailed map of the instability region in which the BLAPs lie. The instability region encompasses both the low-gravity and high-gravity groups of BLAPs, confirming they are phenomenologically related objects, with the low-gravity pulsators having masses of around $0.31\,M_{\odot}$, while the high-gravity pulsators have masses around $0.28\,M_{\odot}$. Furthermore, the morphology of the instability region suggests that pulsators with intermediate masses could also exist. All of the pulsators are located close to the cool, red-edge of the instability region. This coincides with the location of the onset of radiative levitation and the enhancement of iron in the driving region of the star, reinforcing the conclusion that the pulsations are driven by the κ-mechanism. This thesis makes theoretical predictions of the range of periods, effective temperatures and surface gravities in which more BLAP-like pulsators could be discovered. This information is extremely useful for obser-

vational astronomers as they search for stars to form a continuous population, rather than two disparate groups.

This work has also highlighted that GYRE struggles in highly non-adiabatic conditions (such as those with a high luminosity-to-mass ratio or a very large opacity) due to its practice of using the adiabatic eigenfrequencies as initial guesses for the non-adiabatic solutions. A more robust method for non-adiabatic pulsation analysis is being formulated by the GYRE developers, which will shed light on the pulsation behaviour of those stars where the fundamental mode could not be identified.

Several unanswered questions remain regarding the origin and evolutionary status of the chemically peculiar hot subdwarfs. Testing of the diffusion hypothesis as the origin of the heavy metals will require atomic data calculations for those elements in a number of ionisation states. These data must then be incorporated into stellar evolution and/or stellar atmosphere models in order to determine whether radiative levitation is responsible for the peculiar surface abundances. Atomic data calculations are an area of ongoing scientific research (e.g. Fernández-Menchero *et al.*, 2019) but are computationally intensive, particularly for high ionisation states. Aside from diffusion, there are other scenarios which could potentially explain the origin of the heavy-metal subdwarfs. For example, Bauer *et al.* (2019) calculated binary star models involving a white dwarf accreting mass from a hot subdwarf, generating a supernova explosion. Such an interaction may be able to produce a chemically peculiar subdwarf if the subdwarf is contaminated by exotic material from the supernova ejecta. This scenario would also lead to the subdwarf acquiring a high Galactic rest frame velocity as it gets ejected from the disrupted binary system. This agrees with kinematic studies of these stars, which show that these peculiar subdwarfs have unusual galactic orbits (Martin *et al.*, 2017). Detailed evolutionary calculations, including the chemical evolution of such a system would provide a test of the viability of this scenario.

In the case of BLAPs, the field of study is incredibly new, and therefore there remain a number of questions that must be addressed. In Section 5.3.5 we can see the effect that changing the remnant envelope mass has on the location of the instability region. Comparing these theoretical results with the observed properties of BLAPs provides a constraint on the amount of material that can be

stripped from a star during a common envelope event. This constraint provides useful information for the study of common envelope evolution, which remains a poorly understood phase of close binary evolution. Further observations are needed in order to determine the spectroscopic properties of the other known pulsators, which provide a better map of the instability region. If any of these pulsators lie in the region predicted to be stable, then further refinements will be required to my models in order to match observation with theory.

Further theoretical modelling is required to produce a similar set of models showing the outcome for low-mass pre-white dwarfs formed through stable Roche Lobe overflow, so that both formation channels for BLAPs are modelled. Combining the results of the post-CE and post-RLOF models together will provide an updated version of Figure 5.9, which makes predictions of the mass distribution of potential BLAP pulsators, based on their evolution through the BLAP instability region. Combining this distribution with binary population synthesis calculations to determine the actual formation rate of low-mass white dwarf systems would provide a reliable estimate of the expected population distribution of BLAPs.

Overall, this thesis has expanded our understanding of the role played by atomic diffusion in the post-common envelope phase of evolution at a range of masses. Simulations of low-mass pre-white dwarfs have provided a convincing model of the evolutionary status and driving mechanism of BLAPs and unified two separate observational groups into one connected category of star. BLAPs, like hot subdwarfs, are proving to be extremely useful laboratories which can be used to develop our understanding of single and binary star evolution.

References

Aerts, C., Christensen-Dalsgaard, J. & Kurtz, D.W. (2010). *Asteroseismology*. Springer. (Cited on pages xiii, 18, 19 and 25.)

Aizenman, M.L. & Cox, J.P. (1975). Pulsational stability of stars in thermal imbalance. VI - Physical mechanisms and extension to nonradial oscillations. *Astrophysical Journal*, **195**, 175–185. (Cited on pages 115 and 118.)

Aller, L.H. & Chapman, S. (1960). Diffusion in the Sun. *Astrophysical Journal*, **132**, 461. (Cited on page 16.)

Althaus, L.G., Miller Bertolami, M.M. & Córsico, A.H. (2013). New evolutionary sequences for extremely low-mass white dwarfs. Homogeneous mass and age determinations and asteroseismic prospects. *Astronomy & Astrophysics*, **557**, A19. (Cited on page 42.)

Asplund, M., Grevesse, N. & Sauval, A.J. (2005). The Solar Chemical Composition. In I. Barnes Thomas G. & F.N. Bash, eds., *Cosmic Abundances as Records of Stellar Evolution and Nucleosynthesis in honor of David L. Lambert, Proceedings of a symposium held 17-19 June, 2004 in Austin.*, vol. 336 of *Astronomical Society of the Pacific Conference Series*, 25. (Cited on pages 51 and 64.)

Bauer, E.B., White, C.J. & Bildsten, L. (2019). Remnants of Subdwarf Helium Donor Stars Ejected from Close Binaries with Thermonuclear Supernovae. *Astrophysical Journal*, **887**, 68. (Cited on page 151.)

Bethe, H.A. (1939). Energy Production in Stars. *Physical Review*, **55**, 434–456. (Cited on page 7.)

Bethe, H.A. & Critchfield, C.L. (1938). The Formation of Deuterons by Proton Combination. *Physical Review*, **54**, 248–254. (Cited on page 7.)

Blanchette, J.P., Chayer, P., Wesemael, F., Fontaine, G., Fontaine, M., Dupuis, J., Kruk, J.W. & Green, E.M. (2008). FUSE Determination of Abundances in Long-Period Pulsating V1093 Her (PG 1716+426) Stars. *Astrophysical Journal*, **678**, 1329–1341. (Cited on page 39.)

Blöcker, T. (1995). Stellar evolution of low and intermediate-mass stars. I. Mass loss on the AGB and its consequences for stellar evolution. *Astronomy & Astrophysics*, **297**, 727. (Cited on page 52.)

Brown, T.M., Ferguson, H.C., Davidsen, A.F. & Dorman, B. (1997). A Far-Ultraviolet Analysis of the Stellar Populations in Six Elliptical and S0 Galaxies. *Astrophysical Journal*, **482**, 685–707. (Cited on page 31.)

REFERENCES

Brown, T.M., Sweigart, A.V., Lanz, T., Landsman, W.B. & Hubeny, I. (2001). Flash Mixing on the White Dwarf Cooling Curve: Understanding Hot Horizontal Branch Anomalies in NGC 2808. *Astrophysical Journal*, **562**, 368–393. (Cited on pages 68 and 127.)

Bruno, G. (1584). *De l'infinito universo e mondi (On the Infinite Universe and Worlds)*. Venice. (Cited on page 2.)

Burgers, J.M. (1969). *Flow Equations for Composite Gases*. Academic Press. (Cited on pages 65, 96 and 123.)

Byrne, C.M. & Jeffery, C.S. (2018). Post-common envelope binary stars, radiative levitation, and blue large-amplitude pulsators. *Monthly Notices of the Royal Astronomical Society*, **481**, 3810–3820. (Cited on pages 91, 119, 120, 121, 123, 124 and 129.)

Byrne, C.M. & Jeffery, C.S. (2020). Pulsation in faint blue stars. *Monthly Notices of the Royal Astronomical Society*, **492**, 232–244. (Cited on page 119.)

Byrne, C.M., Jeffery, C.S., Tout, C.A. & Hu, H. (2018). The effects of diffusion in hot subdwarf progenitors from the common envelope channel. *Monthly Notices of the Royal Astronomical Society*, **475**, 4728–4738. (Cited on pages 61, 92, 94, 96, 97 and 120.)

Cannon, A.J. & Pickering, E.C. (1912). Classification of 1,688 southern stars by means of their spectra. *Annals of Harvard College Observatory*, **56**, 115–164. (Cited on page 3.)

Charpinet, S., Fontaine, G., Brassard, P. & Dorman, B. (1996). The Potential of Asteroseismology for Hot, Subdwarf B Stars: A New Class of Pulsating Stars? *Astrophysical Journal Letters*, **471**, L103. (Cited on pages 40, 104 and 121.)

Charpinet, S., Fontaine, G., Brassard, P., Chayer, P., Rogers, F.J., Iglesias, C.A. & Dorman, B. (1997). A Driving Mechanism for the Newly Discovered Class of Pulsating Subdwarf B Stars. *Astrophysical Journal Letters*, **483**, L123–L126. (Cited on pages 40, 62, 76 and 83.)

Charpinet, S., Brassard, P., Fontaine, G., Green, E.M., Van Grootel, V., Randall, S.K. & Chayer, P. (2009). Progress in Sounding the Interior of Pulsating Hot Subdwarf Stars. In J.A. Guzik & P.A. Bradley, eds., *American Institute of Physics Conference Series*, vol. 1170 of *American Institute of Physics Conference Series*, 585–596. (Cited on page 38.)

Charpinet, S., Fontaine, G., Brassard, P., Green, E.M., Van Grootel, V., Randall, S.K., Silvotti, R., Baran, A.S., Østensen, R.H., Kawaler, S.D. & Telting, J.H. (2011). A compact system of small planets around a former red-giant star. *Nature*, **480**, 496–499. (Cited on page 34.)

Chen, X., Maxted, P.F.L., Li, J. & Han, Z. (2017). The Formation of EL CVn-type Binaries. *Monthly Notices of the Royal Astronomical Society*, **467**, 1874–1889. (Cited on pages 42 and 146.)

Córsico, A.H., Romero, A.D., Althaus, L.r.G., Pelisoli, I. & Kepler, S.O. (2018). Blue Large-Amplitude Pulsators (BLAPs): possible origin, evolutionary status, and nature of their pulsations. *arXiv e-prints*, arXiv:1809.07451. (Cited on page 44.)

Cowling, T.G. (1941). The non-radial oscillations of polytropic stars. *Monthly Notices of the Royal Astronomical Society*, **101**, 367. (Cited on page 25.)

Cox, J.P. (1980). *Theory of stellar pulsation*. Princeton University Press. (Cited on page 115.)

Cox, J.P. & Giuli, R.T. (1968). *Principles of stellar structure*. Gordon & Breach. (Cited on page 51.)

Dagum, L. & Menon, R. (1998). OpenMP: an industry standard API for shared-memory programming. *IEEE Computational Science and Engineering*, **5**, 46–55. (Cited on page 48.)

Dorman, B., Rood, R.T. & O'Connell, R.W. (1993). Ultraviolet Radiation from Evolved Stellar Populations. I. Models. *Astrophysical Journal*, **419**, 596. (Cited on page 85.)

Dorsch, M., Latour, M. & Heber, U. (2019). Heavy metals in intermediate He-rich hot subdwarfs: the chemical composition of HZ 44 and HD 127493. *Astronomy & Astrophysics*, **630**, A130. (Cited on page 40.)

Driebe, T., Schoenberner, D., Bloecker, T. & Herwig, F. (1998). The evolution of helium white dwarfs. I. The companion of the millisecond pulsar PSR J1012+5307. *Astronomy & Astrophysics*, **339**, 123–133. (Cited on page 127.)

Eddington, A.S. (1920). The internal constitution of the stars. *The Observatory*, **43**, 341–358. (Cited on page 7.)

Eddington, S.A.S. (1930). *The Internal Constitution of Stars*. Cambridge University Press, 2nd edn. (Cited on page 15.)

Edelmann, H., Heber, U. & Napiwotzki, R. (2001). Metal abundances of sdB stars. *Astronomische Nachrichten*, **322**, 401–404. (Cited on page 86.)

Eggleton, P.P. (1971). The evolution of low mass stars. *Monthly Notices of the Royal Astronomical Society*, **151**, 351. (Cited on page 53.)

Fernández-Menchero, L., Smyth, R.T., Ramsbottom, C.A. & Ballance, C.P. (2019). Spectroscopic diagnostics of low-ionized iron-peak elements. Electron-impact excitation of Ni^{3+} and photoionization of Ni^{2+}. *Monthly Notices of the Royal Astronomical Society*, **483**, 2154–2164. (Cited on page 151.)

Fontaine, G., Brassard, P., Charpinet, S., Green, E.M., Chayer, P., Billères, M. & Randall, S.K. (2003). A Driving Mechanism for the Newly Discovered Long-Period Pulsating Subdwarf B Stars. *Astrophysical Journal*, **597**, 518–534. (Cited on pages 40, 62, 83 and 121.)

Fontaine, G., Brassard, P., Green, E.M., Chayer, P. & Charpinet, S. (2008). Radiative levitation: a likely explanation for pulsations in the unique hot O subdwarf star SDSS J1600+0748. *Communications in Asteroseismology*, **157**, 305–306. (Cited on page 104.)

Geier, S. (2013). Hot subdwarf stars in close-up view. III. Metal abundances of subdwarf B stars. *Astronomy & Astrophysics*, **549**, A110. (Cited on pages xv, 36, 73, 75 and 86.)

REFERENCES

Gianninas, A., Curd, B., Fontaine, G., Brown, W.R. & Kilic, M. (2016). Discovery of Three Pulsating, Mixed-atmosphere, Extremely Low-mass White Dwarf Precursors. *Astrophysical Journal Letters*, **822**, L27. (Cited on pages 42 and 146.)

Green, E.M., Fontaine, G., Reed, M.D., Callerame, K., Seitenzahl, I.R., White, B.A., Hyde, E.A., Østensen, R., Cordes, O., Brassard, P., Falter, S., Jeffery, E.J., Dreizler, S., Schuh, S.L., Giovanni, M., Edelmann, H., Rigby, J. & Bronowska, A. (2003). Discovery of A New Class of Pulsating Stars: Gravity-Mode Pulsators among Subdwarf B Stars. *Astrophysical Journal Letters*, **583**, L31–L34. (Cited on pages 40, 121, 122 and 144.)

Greenstein, J.L. & Sargent, A.I. (1974). The Nature of Faint Blue Stars in the Halo. II. *Astrophysical Journal Supplemental Series*, **28**, 157. (Cited on page 31.)

Grevesse, N. & Noels, A. (1993). Cosmic abundances of the elements. In N. Prantzos, E. Vangioni-Flam & M. Casse, eds., *Origin and Evolution of the Elements*, 15–25. (Cited on page 51.)

Grevesse, N. & Sauval, A.J. (1998). Standard Solar Composition. *Space Science Reviews*, **85**, 161–174. (Cited on pages 50, 51, 64, 94 and 123.)

Han, Z., Podsiadlowski, P., Maxted, P.F.L., Marsh, T.R. & Ivanova, N. (2002). The origin of subdwarf B stars - I. The formation channels. *Monthly Notices of the Royal Astronomical Society*, **336**, 449–466. (Cited on pages 31, 32, 33, 34, 62 and 87.)

Han, Z., Podsiadlowski, P., Maxted, P.F.L. & Marsh, T.R. (2003). The origin of subdwarf B stars - II. *Monthly Notices of the Royal Astronomical Society*, **341**, 669–691. (Cited on pages 31, 34 and 62.)

Heber, U. (2009). Hot Subdwarf Stars. *Annual Review of Astronomy & Astrophysics*, **47**, 211–251. (Cited on page 5.)

Heber, U. (2016). Hot Subluminous Stars. *Publications of the Astronomical Society of the Pacific*, **128**, 082001. (Cited on pages 31 and 63.)

Henyey, L.G., Wilets, L., Böhm, K.H., Lelevier, R. & Levee, R.D. (1959). A Method for Automatic Computation of Stellar Evolution. *Astrophysical Journal*, **129**, 628. (Cited on pages 47 and 54.)

Hermes, J.J., Montgomery, M.H., Gianninas, A., Winget, D.E., Brown, W.R., Harrold, S.T., Bell, K.J., Kenyon, S.J., Kilic, M. & Castanheira, B.G. (2013). A new class of pulsating white dwarf of extremely low mass: the fourth and fifth members. *Monthly Notices of the Royal Astronomical Society*, **436**, 3573–3580. (Cited on page 42.)

Hertzsprung, E. (1911). Ueber die Verwendung photographischer effektiver Wellenlaengen zur Bestimmung von Farbenaequivalenten. *Publikationen des Astrophysikalischen Observatoriums zu Potsdam*, **63**. (Cited on page 3.)

Hu, H., Tout, C.A., Glebbeek, E. & Dupret, M.A. (2011). Slowing down atomic diffusion in subdwarf B stars: mass loss or turbulence? *Monthly Notices of the Royal Astronomical Society*, **418**, 195–205. (Cited on pages 41, 53, 65, 82, 83, 85, 96, 104, 120 and 123.)

Iglesias, C.A. & Rogers, F.J. (1996). Updated Opal Opacities. *Astrophysical Journal*, **464**, 943. (Cited on page 51.)

Istrate, A.G., Tauris, T.M., Langer, N. & Antoniadis, J. (2014). The timescale of low-mass proto-helium white dwarf evolution. *Astronomy & Astrophysics*, **571**, L3. (Cited on pages 42 and 127.)

Istrate, A.G., Fontaine, G. & Heuser, C. (2017). A Model of the Pulsating Extremely Low-mass White Dwarf Precursor WASP 0247-25B. *Astrophysical Journal*, **847**, 130. (Cited on page 42.)

Ivanova, N., Justham, S., Chen, X., De Marco, O., Fryer, C.L., Gaburov, E., Ge, H., Glebbeek, E., Han, Z., Li, X.D., Lu, G., Marsh, T., Podsiadlowski, P., Potter, A., Soker, N., Taam, R., Tauris, T.M., van den Heuvel, E.P.J. & Webbink, R.F. (2013). Common envelope evolution: where we stand and how we can move forward. *Astronomy & Astrophysics Review*, **21**, 59. (Cited on pages 34, 63 and 140.)

Jeffery, C.S. & Saio, H. (2006a). Fe-bump instability: the excitation of pulsations in subdwarf B and other low-mass stars. *Monthly Notices of the Royal Astronomical Society*, **371**, 659–672. (Cited on page 109.)

Jeffery, C.S. & Saio, H. (2006b). Gravity-mode pulsations in subdwarf B stars: a critical test of stellar opacity. *Monthly Notices of the Royal Astronomical Society*, **372**, L48–L52. (Cited on pages 41, 62, 83, 112 and 113.)

Jeffery, C.S. & Saio, H. (2007). Improved opacities and pulsation stability in subluminous B and O stars. *Monthly Notices of the Royal Astronomical Society*, **378**, 379–383. (Cited on pages 41, 76 and 104.)

Jeffery, C.S. & Saio, H. (2013). Pulsation in extremely low mass helium stars. *Monthly Notices of the Royal Astronomical Society*, **435**, 885–892. (Cited on page 42.)

Jeffery, C.S. & Saio, H. (2016). Radial pulsation as a function of hydrogen abundance. *Monthly Notices of the Royal Astronomical Society*, **458**, 1352–1373. (Cited on pages 43, 112, 113, 114, 118 and 124.)

Jeffery, C.S., Baran, A.S., Behara, N.T., Kvammen, A., Martin, P., N, N., Østensen, R.H., Preece, H.P., Reed, M.D., Telting, J.H. & Woolf, V.M. (2017). Discovery of a variable lead-rich hot subdwarf: UVO 0825+15. *Monthly Notices of the Royal Astronomical Society*, **465**, 3101–3124. (Cited on pages xv, 40, 62, 73 and 75.)

Justham, S., Wolf, C., Podsiadlowski, P. & Han, Z. (2009). Type Ia supernovae and the formation of single low-mass white dwarfs. *Astronomy & Astrophysics*, **493**, 1081–1091. (Cited on page 42.)

Kepler, S.O., Kleinman, S.J., Nitta, A., Koester, D., Castanheira, B.G., Giovannini, O., Costa, A.F.M. & Althaus, L. (2007). White dwarf mass distribution in the SDSS. *Monthly Notices of the Royal Astronomical Society*, **375**, 1315–1324. (Cited on page 42.)

REFERENCES

Kilic, M., Stanek, K.Z. & Pinsonneault, M.H. (2007). The Future Is Now: The Formation of Single Low-Mass White Dwarfs in the Solar Neighborhood. *Astrophysical Journal*, **671**, 761–766. (Cited on page 42.)

Kilkenny, D. (2007). Pulsating Hot Subdwarfs – An Observational Review. *Communications in Asteroseismology*, **150**, 234. (Cited on page 40.)

Kilkenny, D., Koen, C., O'Donoghue, D. & Stobie, R.S. (1997). A new class of rapidly pulsating star - I. EC 14026-2647, the class prototype. *Monthly Notices of the Royal Astronomical Society*, **285**, 640–644. (Cited on pages 40 and 121.)

Kippenhahn, R., Weigert, A. & Hofmeister, E. (1967). Methods for Calculating Stellar Evolution. *Methods in Computational Physics*, **7**, 129–190. (Cited on page 47.)

Kirchhoff, G. (1860). Ueber die Fraunhofer'schen Linien. *Annalen der Physik*, **185**, 148–150. (Cited on page 3.)

Kupfer, T., Bauer, E.B., Burdge, K.B., Bellm, E.C., Bildsten, L., Fuller, J., Hermes, J., Kulkarni, S.R., Prince, T.A., van Roestel, J., Dekany, R., Duev, D.A., Feeney, M., Giomi, M., Graham, M.J., Kaye, S., Laher, R.R., Masci, F.J., Porter, M., Riddle, R., Shupe, D.L., Smith, R.M., Soumagnac, M.T., Szkody, P. & Ward, C. (2019). A New Class of Large-amplitude Radial-mode Hot Subdwarf Pulsators. *Astrophysical Journal Letters*, **878**, L35. (Cited on pages iv, xix, xx, 43, 44, 45, 121, 122, 123, 131, 134, 135, 139, 144 and 147.)

Landolt, A.U. (1968). A New Short-Period Blue Variable. *Astrophysical Journal*, **153**, 151. (Cited on page 129.)

Latour, M., Green, E.M. & Fontaine, G. (2019). Discovery of a second pulsating intermediate helium-enriched sdOB star. *Astronomy & Astrophysics*, **623**, L12. (Cited on page 40.)

Magnus, W. (1954). On the exponential solution of differential equations for a linear operator. *Communications on Pure and Applied Mathematics*, **7**, 649–673. (Cited on page 59.)

Martin, P., Jeffery, C.S., Naslim, N. & Woolf, V.M. (2017). Kinematics of Subluminous O and B Stars by Surface Helium Abundance. *Monthly Notices of the Royal Astronomical Society*, **467**, 68–82. (Cited on page 151.)

Maxted, P.F.L., Heber, U., Marsh, T.R. & North, R.C. (2001). The binary fraction of extreme horizontal branch stars. *Monthly Notices of the Royal Astronomical Society*, **326**, 1391–1402. (Cited on page 36.)

Maxted, P.F.L., Bloemen, S., Heber, U., Geier, S., Wheatley, P.J., Marsh, T.R., Breedt, E., Sebastian, D., Faillace, G., Owen, C., Pulley, D., Smith, D., Kolb, U., Haswell, C.A., Southworth, J., Anderson, D.R., Smalley, B., Collier Cameron, A., Hebb, L., Simpson, E.K., West, R.G., Bochinski, J., Busuttil, R. & Hadigal, S. (2014). EL CVn-type binaries - discovery of 17 helium white dwarf precursors in bright eclipsing binary star systems. *Monthly Notices of the Royal Astronomical Society*, **437**, 1681–1697. (Cited on page 42.)

Mayor, M. & Queloz, D. (1995). A Jupiter-mass companion to a solar-type star. *Nature*, **378**, 355–359. (Cited on page 2.)

Michaud, G. (1970). Diffusion Processes in Peculiar a Stars. *Astrophysical Journal*, **160**, 641. (Cited on pages 17 and 62.)

Michaud, G., Richer, J. & Richard, O. (2011). Horizontal branch evolution, metallicity, and sdB stars. *Astronomy & Astrophysics*, **529**, A60. (Cited on pages 41, 82, 83, 104 and 120.)

Michaud, G., Alecian, G. & Richer, J. (2015). *Atomic Diffusion in Stars*. Springer. (Cited on page 15.)

Miller Bertolami, M.M., Althaus, L.G., Unglaub, K. & Weiss, A. (2008). Modeling He-rich subdwarfs through the hot-flasher scenario. *Astronomy & Astrophysics*, **491**, 253–265. (Cited on pages 68 and 127.)

Miller Bertolami, M.M., Córsico, A.H. & Althaus, L.G. (2011). On the Challenging Variability of LS IV-14°116: Pulsational Instabilities Excited by the epsilon-Mechanism. *Astrophysical Journal Letters*, **741**, L3. (Cited on page 18.)

Naslim, N., Jeffery, C.S., Behara, N.T. & Hibbert, A. (2011). An extremely peculiar hot subdwarf with a 10 000-fold excess of zirconium, yttrium and strontium. *Monthly Notices of the Royal Astronomical Society*, **412**, 363–370. (Cited on pages 38, 62 and 92.)

Naslim, N., Geier, S., Jeffery, C.S., Behara, N.T., Woolf, V.M. & Classen, L. (2012). The helium-rich subdwarf CPD-20°1123: a post-common-envelope binary evolving on to the extended horizontal branch. *Monthly Notices of the Royal Astronomical Society*, **423**, 3031–3038. (Cited on pages 38, 62 and 85.)

Németh, P., Kawka, A. & Vennes, S. (2012). A selection of hot subluminous stars in the GALEX survey - II. Subdwarf atmospheric parameters. *Monthly Notices of the Royal Astronomical Society*, **427**, 2180–2211. (Cited on pages 63 and 85.)

Opacity Project Team (1995). *The Opacity Project, Vol. 1*. Institute of Physics. (Cited on pages 50, 51, 64, 115 and 123.)

Opacity Project Team (1997). *The Opacity Project, Vol. 2*. Institute of Physics. (Cited on pages 50, 51, 64, 115 and 123.)

Oreiro, R., Ulla, A., Pérez Hernández, F., Østensen, R., Rodríguez López, C. & MacDonald, J. (2004). ¡ASTROBJ¿Balloon 090100001¡/ASTROBJ¿: A bright, high amplitude sdB pulsator. *Astronomy & Astrophysics*, **418**, 243–247. (Cited on page 40.)

Østensen, R.H., Oreiro, R., Solheim, J.E., Heber, U., Silvotti, R., González-Pérez, J.M., Ulla, A., Pérez Hernández, F., Rodríguez-López, C. & Telting, J.H. (2010). A survey for pulsating subdwarf B stars with the Nordic Optical Telescope. *Astronomy & Astrophysics*, **513**, A6. (Cited on pages 122 and 144.)

Ostlie, D.A. & Cox, A.N. (1986). A Linear Survey of the Mira Variable Star Instability Region of the Hertzsprung-Russell Diagram. *Astrophysical Journal*, **311**, 864. (Cited on page 128.)

REFERENCES

O'Toole, S.J. & Heber, U. (2006). Abundance studies of sdB stars using UV echelle HST/STIS spectroscopy. *Astronomy & Astrophysics*, **452**, 579–590. (Cited on page 41.)

Paczyński, B. (1976). Common Envelope Binaries. In P. Eggleton, S. Mitton & J. Whelan, eds., *Structure and Evolution of Close Binary Systems*, vol. 73 of *IAU Symposium*, 75. (Cited on page 33.)

Paxton, B., Bildsten, L., Dotter, A., Herwig, F., Lesaffre, P. & Timmes, F. (2011). Modules for Experiments in Stellar Astrophysics (MESA). *Astrophysical Journal Supplemental Series*, **192**, 3. (Cited on pages 47, 56, 63, 92 and 123.)

Paxton, B., Cantiello, M., Arras, P., Bildsten, L., Brown, E.F., Dotter, A., Mankovich, C., Montgomery, M.H., Stello, D., Timmes, F.X. & Townsend, R. (2013). Modules for Experiments in Stellar Astrophysics (MESA): Planets, Oscillations, Rotation, and Massive Stars. *Astrophysical Journal Supplemental Series*, **208**, 4. (Cited on pages 48, 56, 63, 92 and 123.)

Paxton, B., Marchant, P., Schwab, J., Bauer, E.B., Bildsten, L., Cantiello, M., Dessart, L., Farmer, R., Hu, H., Langer, N., Townsend, R.H.D., Townsley, D.M. & Timmes, F.X. (2015). Modules for Experiments in Stellar Astrophysics (MESA): Binaries, Pulsations, and Explosions. *Astrophysical Journal Supplemental Series*, **220**, 15. (Cited on pages 48, 53, 63, 92 and 123.)

Paxton, B., Schwab, J., Bauer, E.B., Bildsten, L., Blinnikov, S., Duffell, P., Farmer, R., Goldberg, J.A., Marchant, P., Sorokina, E., Thoul, A., Townsend, R.H.D. & Timmes, F.X. (2018). Modules for Experiments in Stellar Astrophysics (MESA): Convective Boundaries, Element Diffusion, and Massive Star Explosions. *Astrophysical Journal Supplemental Series*, **234**, 34. (Cited on pages 48, 92 and 123.)

Paxton, B., Smolec, R., Schwab, J., Gautschy, A., Bildsten, L., Cantiello, M., Dotter, A., Farmer, R., Goldberg, J.A., Jermyn, A.S., Kanbur, S.M., Marchant, P., Thoul, A., Townsend, R.H.D., Wolf, W.M., Zhang, M. & Timmes, F.X. (2019). Modules for Experiments in Stellar Astrophysics (MESA): Pulsating Variable Stars, Rotation, Convective Boundaries, and Energy Conservation. *Astrophysical Journal Supplemental Series*, **243**, 10. (Cited on pages 48 and 123.)

Pietrukowicz, P., Dziembowski, W.A., Latour, M., Angeloni, R., Poleski, R., di Mille, F., Soszyński, I., Udalski, A., Szymański, M.K., Wyrzykowski, Ł., Kozłowski, S., Skowron, J., Skowron, D., Mróz, P., Pawlak, M. & Ulaczyk, K. (2017). Blue large-amplitude pulsators as a new class of variable stars. *Nature Astronomy*, **1**, 0166. (Cited on pages iv, xvii, xix, xx, 43, 44, 91, 92, 93, 94, 97, 104, 108, 117, 119, 121, 122, 123, 131, 134, 135, 139, 144 and 147.)

Podsiadlowski, P., Han, Z., Lynas-Gray, A.E. & Brown, D. (2008). Hot Subdwarfs in Binaries as the Source of the Far-UV Excess in Elliptical Galaxies. In U. Heber, C.S. Jeffery & R. Napiwotzki, eds., *Hot Subdwarf Stars and Related Objects ASP Conference Series, Vol. 392, Proceedings of the conference held 23-27 July, 2007, at Otto-Friedrich-Universität, Bamberg, Germany. Edited by Ulrich Heber, C. Simon Jeffery, and Ralf Napiwotzki., p.15*, vol. 392, 15, Astronomical Society of the Pacific Conference Series. (Cited on pages 33, 35 and 37.)

Pols, O.R., Tout, C.A., Eggleton, P.P. & Han, Z. (1995). Approximate input physics for stellar modelling. *Monthly Notices of the Royal Astronomical Society*, **274**, 964–974. (Cited on page 53.)

Ramsay, G. (2018). Identifying blue large-amplitude pulsators in the Galactic plane using Gaia DR2: a case study. *Astronomy & Astrophysics*, **620**, L9. (Cited on page 145.)

Reimers, D. (1975). Circumstellar envelopes and mass loss of red giant stars. In B. Baschek, W.H. Kegel & G. Traving, eds., *Problems in stellar atmospheres and envelopes.*, 229–256, Springer, Berlin. (Cited on page 52.)

Romero, A.D., Córsico, A.H., Althaus, L.G., Pelisoli, I. & Kepler, S.O. (2018). On the evolutionary status and pulsations of the recently discovered blue large-amplitude pulsators (BLAPs). *Monthly Notices of the Royal Astronomical Society*, **477**, L30–L34. (Cited on pages 44, 94, 97, 104 and 108.)

Russell, H.N. (1914). Relations Between the Spectra and Other Characteristics of the Stars. *Popular Astronomy*, **22**, 275–294. (Cited on page 3.)

Schindler, J.T., Green, E.M. & Arnett, W.D. (2015). Exploring Stellar Evolution Models of sdB Stars using MESA. *Astrophysical Journal*, **806**, 178. (Cited on pages 64, 86 and 88.)

Shibahashi, H. (2005). The DB gap and pulsations of white dwarfs. In G. Alecian, O. Richard & S. Vauclair, eds., *EAS Publications Series*, vol. 17 of *EAS Publications Series*, 143–148. (Cited on page 129.)

Stancliffe, R.J. & Eldridge, J.J. (2009). Modelling the binary progenitor of Supernova 1993J. *Monthly Notices of the Royal Astronomical Society*, **396**, 1699–1708. (Cited on page 53.)

Stancliffe, R.J., Fossati, L., Passy, J.C. & Schneider, F.R.N. (2016). Confronting uncertainties in stellar physics. II. Exploring differences in main-sequence stellar evolution tracks. *Astronomy & Astrophysics*, **586**, A119. (Cited on pages 64, 94 and 123.)

Thoul, A.A., Bahcall, J.N. & Loeb, A. (1994). Element diffusion in the solar interior. *Astrophysical Journal*, **421**, 828–842. (Cited on pages 65, 96 and 123.)

Townsend, R. (2019). Read mesa files into a idl structure. (Cited on page 58.)

Townsend, R.H.D. & Teitler, S.A. (2013). GYRE: an open-source stellar oscillation code based on a new Magnus Multiple Shooting scheme. *Monthly Notices of the Royal Astronomical Society*, **435**, 3406–3418. (Cited on pages 58, 59, 96 and 124.)

Townsend, R.H.D., Goldstein, J. & Zweibel, E.G. (2018). Angular momentum transport by heat-driven g-modes in slowly pulsating B stars. *Monthly Notices of the Royal Astronomical Society*, **475**, 879–893. (Cited on pages 58, 96 and 124.)

Unglaub, K. (2008). The Mass Loss Rates of sdB Stars. In U. Heber, C.S. Jeffery & R. Napiwotzki, eds., *Hot Subdwarf Stars and Related Objects*, vol. 392 of *Astronomical Society of the Pacific Conference Series*, 95. (Cited on page 52.)

REFERENCES

Unglaub, K. & Bues, I. (2001). The influence of diffusion and mass loss on the chemical composition of subdwarf B stars. *Astronomy & Astrophysics*, **374**, 570–583. (Cited on page 52.)

Unno, W., Osaki, Y., Ando, H., Saio, H. & Shibahashi, H. (1989). *Nonradial oscillations of stars*. University of Tokyo Press. (Cited on page 25.)

von Weizsäcker, C.F. (1938). Uber elementumwandlungen im innern der sterne ii. *Physikalische Zeitschrift*, **39**, 633–646. (Cited on page 7.)

Wu, T. & Li, Y. (2018). Which evolutionary status does the Blue Large-Amplitude Pulsators stay at? *Monthly Notices of the Royal Astronomical Society*, **478**, 3871–3877. (Cited on page 44.)

Xiong, H., Chen, X., Podsiadlowski, P., Li, Y. & Han, Z. (2017). Subdwarf B stars from the common envelope ejection channel. *Astronomy & Astrophysics*, **599**, A54. (Cited on pages 63, 64, 73, 80 and 85.)

Zhang, X. & Jeffery, C.S. (2012). Evolutionary models for double helium white dwarf mergers and the formation of helium-rich hot subdwarfs. *Monthly Notices of the Royal Astronomical Society*, **419**, 452–464. (Cited on pages 36 and 62.)